DISTRIBUTED ENERGY-BALANCE GLACIER MELT-MODELLING IN THE DONJEK RANGE OF THE ST. ELIAS MOUNTAINS, YUKON TERRITORY, CANADA: MODEL TRANSFERABILITY IN SPACE AND TIME

by

Andrew Hugh MacDougall

BSc, St. Francis Xavier University, 2008

THESIS SUBMITTED IN PARTIAL FULFILLMENT

OF THE REQUIREMENTS FOR THE DEGREE OF

MASTER OF SCIENCE

IN THE DEPARTMENT

OF

EARTH SCIENCES

SIMON FRASER UNIVERSITY

Fall 2010

APPROVAL

Name: **Andrew MacDougall**

Degree: **Master of Science**

Title of Thesis: **Distributed energy-balance glacier melt-modelling in the Donjek Range of the St. Elias Mountains, Yukon Territory, Canada: model transferability in space and time**

Examining Committee:

Chair: **Dr. John Clague**
Professor, Department of Earth Sciences

Dr. Gwenn Flowers
Senior Supervisor
Professor, Department of Earth Sciences

Dr. Bernhard Rabus
Supervisor
Adjunct, Department of Earth Sciences

By written/email consultation from Scotland
Dr. Benjamin Brock
External Examiner
Senior Lecturer, University of Dundee

Date Defended/Approved: October 20th, 2010

Declaration of
Partial Copyright Licence

Abstract

Modelling melt from glaciers is crucial to assessing regional hydrology and eustatic sea-level rise. To investigate melt-model transferability, a distributed energy-balance melt model (DEBM) is applied to two glaciers of opposing aspects in the Donjek Range of the St. Elias Mountains, Yukon Territory, Canada. An analysis is conducted in four stages to assess the transferability of the DEBM in space and time: (1) locally derived model parameter values and meteorological forcing variables are used to assess model skill; (2) model parameter values are transferred between glacier sites and between years of study; (3) measured meteorological forcing variables are transferred between glaciers, using locally derived parameter values; (4) both model parameter values and measured meteorological forcing variables are transferred from one glacier site to the other, treating the second glacier site as an extension of the first. The model has high transferability in time, but has limited transferability in space.

To those who taught me how to read, allowing me to be whatever I wanted to be.

Acknowledgments

I would like to thank my supervisor Gwenn Flowers for her support and guidance over the last two years and for giving me the opportunity to travel to a remote environment that few are lucky enough to ever see. Her constructive criticism, astute recommendations and positive attitude have been invaluable in the completion of this thesis. I would also like to thank my committee member Bernhard Rabus for his guidance and my external examiner Ben Brock for his valuable comments.

I am grateful for camaraderie of my fellow lab-mates who have made our cavern of a lab an enjoyable place to work. I am grateful to Guðni Rosenkjær, Nicolas Roux and Patrick Belliveau for their contributions to this work and company in the field. Special thanks to Brett Wheler who's previous work on similar projects meant that I did not have to start this project from scratch.

I am are grateful to the Natural Science and Engineering Research Council of Canada (NSERC), the Canada Foundation of Innovation (CFI), the Canada Research Chairs (CRC) program, the Northern Scientific Training Program (NSTP), and Simon Fraser University for funding. I am particularly grateful for support from NSERC PGS-M. Permission to conduct this research was granted by the Kluane First Nation, Parks Canada, and the Yukon Territorial Government. Support from the Kluane Lake Research Station (KLRS) and Kluane National Park and Reserve is greatly appreciated. I am indebted to Andy Williams, Sian Williams, Lance Goodwin (KLRS), Doug Makkonen and Stephen Soubliere (Trans North Helicopters) for logistical support, and to P. Belliveau, B. Wheler, G. Rosenkjær, N. Roux, A. Jarosch, L. Mingo, J. Logher, F. Anslow, C. Schoof, S. Heðinsdóttir, and A. Rushmere for field assistance.

I would like to thank my Mother and Father for their unwavering support throughout my education and thank Uncle Gary for his help since I arrived in Vancouver.

Contents

List of Tables

List of Figures

Chapter 1

Introduction

1.1 Motivation

Changes in the cryosphere resulting from recent anthropogenic climate warming have become an important focus of study due to potential effects on society (Lemke et al., 2007). The mountain glacier and ice-cap components of the cryosphere in particular are of concern due to their relatively rapid response time to a change in climate (Oerlemans et al., 1998), significant capacity to interfere with fresh water resources, and their potential contribution to eustatic sea-level rise (Lemke et al., 2007). As a result of these concerns there has been a recent effort to model the mass balance of the world's mountain glaciers and ice-caps driven with output from the General Circulation Models (GCMs) (e.g. de Woul and Hock, 2005, Oerlemans et al., 2005). These simulations have produced a wide range of 21st century eustatic sea-level rise projections, from 4 cm Sea Level Equivalent (SLE) (Raper and Braithwaite, 2006) to 36 cm SLE (Bahr et al., 2009). With such a range in projected sea-level rise and concurrent uncertainty on the effects on fresh water resources, there is a need to further evaluate the validity of assumptions necessary to implement glacier melt models over large spatial domains.

1.2 Background

There are two general approaches to modelling the melt of glaciers. The empirical approach where a strong correlation between melt and positive temperatures is assumed (Hock, 2003), and the physical approach where the energy available for melt is estimated by measuring or parameterizing all of the other components of the surface energy balance of ice or snow (Hock, 2005). Empirical melt models, including classical temperature-index models and enhanced temperature-index models have the advantage that they require few meteorological inputs and produce reliable estimates of ablation (Hock, 1999, 2003, Pellicciotti et al., 2005). The disadvantage to empirical models is that they are tuned to the unique energy balance and climatological conditions of the glaciers on which they are derived. As climate changes empirical models are unable to take into account non-linear changes in the relationship between temperature and melt caused by factors such as changes in cloudiness and increases in the incoming longwave radiation flux. The study of Hock et al. (2007) explored the effect of using empirically-based and physically-based models to project melt decades into the future. The study found that empirical models of any complexity significantly underestimated melt with respect to a physically-based model. This suggests that empirical models, while reliable over short time-scales, are unreliable for assessing glacier degradation under anthropogenic climate warming.

The most physically justified form of glacier melt modeling is energy-balance melt-modeling Hock (2005). Since energy balance components tend to only be measured at a small number of location on a glacier these components must be extrapolated to grid across the glacier surface if melt is to be computed over the entire glacier. Below is discussed how such distributed energy balance melt models (DEBMs) have been developed for many of the best studied glacier sites (e.g Anderson et al., 2010, Anslow et al., 2008, Arnold et al., 1996, Brock et al., 2000a, Hock and Holmgren, 2005, Klok and Oerlemans, 2002). For the full details of the DEBM used in this study see *Modelling Methods*.

1.2.1 Conceptualization of energy balance

The surface energy balance or ice or snow is expressed as:

$$Q_M = (S_{\text{in}}(1-\alpha) + L_{\text{in}} - L_{\text{out}}) + Q_H + Q_L - Q_g + Q_R, \tag{1.1}$$

where S_{in} is incoming shortwave radiation, α is the albedos of the ice or snow surface, L_{in} is the incoming longwave radiation and L_{out} is the outgoing longwave radiation. Q_H is the sensible heat flux, the energy exchanged between the glacier and the atmosphere. Q_L is the latent heat flux, the heat transferred to or from the glacier through sublimation, deposition, evapouration or condensation. Q_g is the heat transferred to and from the glacier subsurface when the ice or snow of the subsurface changes temperature. Q_R is heat from rain, the sensible heat released when rain is cooled to the freezing point. Q_M is the energy available to melt ice.

Shortwave radiation

Incoming shortwave radiation has been computed in two ways in DEBMs: by measuring the radiation at a meteorological station on or near the glacier (e.g. Hock and Holmgren, 2005, Brock et al., 2000b) or by computing the incoming shortwave radiation from top of the atmosphere radiation and scattering coefficients (Klok and Oerlemans, 2002). Diffuse and direct shortwave radiation are partitioned using empirical relationships derived from sophisticated radiation monitoring instrumentation deployed at only a small number of research stations. Klok and Oerlemans (2002) derived an empirical relationship to partition shortwave radiation using cloud fraction as the independent variable. Hock and Holmgren (2005) relate the ratio of diffuse radiation over global radiation to global radiation over top of the atmosphere radiation. This relationship was originally derived by Collares-Pereira and Rabl (1979) for solar power applications in the United States. Diffuse solar radiation is applied to all grid points, while direct solar radiation is corrected for the slope and aspect of the grid point and applied only to those grid points that are not shaded by topography. Topographic shading is calculated using a digital elevation map of the terrain surrounding the glacier and knowledge of astronomical theory (e.g. Arnold et al., 1996, Anslow et al., 2008).

Albedo

The albedos of glacier ice and snow vary immensely in time and space (Paterson, 1994) making the treatment of this variable one of the most important considerations in energy balance modeling (Hock, 2005). Schemes to treat albedo evolution in DEBMs range from

the very simple method of assigning snow, firn and ice static albedos (e.g. Arnold et al., 1996) to complex multivariable parameterizations (e.g. Hock and Holmgren, 2005, Oerlemans and Knap, 1998). Two commonly used albedo evolution parameterizations are: that of Oerlemans and Knap (1998), which relates snow albedo to time since the last snowfall and snow depth; and that of Hock and Holmgren (2005), which related snow albedo to temperature, time since the last snow fall and snowfall rate. A physically-based albedo evolution model has been developed (Gardner and Sharp, 2010), but has yet to be implemented in DEBMs.

Outgoing longwave radiation and subsurface heat flux

Outgoing longwave radiation is the main mechanism by which glaciers lose heat (Hock, 2005). This quantity is easily calculated using knowledge of the glacier surface temperature and the Stefan-Boltzmann relationship. Surface temperature is internally calculated using a subsurface heat transport model (e.g. Reijmer and Hock, 2008), or assumed to always be at freezing point (e.g. Anslow et al., 2008). If not assumed to be zero the subsurface flux (Q_g) is accounted for using a subsurface model (e.g. Reijmer and Hock, 2008). In some studies the subsurface flux has been implicitly taken into account by interactively lowering the surface temperature to balance negative energy balances by reducing the calculated outgoing longwave radiation (e.g. Hock and Holmgren, 2005).

Incoming longwave radiation

Incoming longwave radiation is the radiation emitted by the atmosphere, i.e. the greenhouse effect (Oke, 1987). This quantity is estimated in DEBMs either as the residual of measured net all-wave radiation and the other radiative components of the energy balance (net shortwave and outgoing longwave radiation) (e.g. Hock and Holmgren, 2005), or calculated using measured air temperature and the Stefan-Boltzmann relationship while parameterizing the emissivity of the atmosphere as a function of cloud fraction (e.g. Klok and Oerlemans, 2002).

Turbulent energy fluxes

Sensible and latent heat fluxes, the turbulent fluxes, are usually calculated using the bulk aerodynamic approach or some simplified version of this approach in DEBMs (e.g. Brock et al., 2000b, Hock and Holmgren, 2005, Anslow et al., 2008). The approach relates sensible heat flux to temperature, wind speed and a number of physical and stability constants. Latent heat flux is related to vapor pressure, wind speed and similar physical and stability constants. Despite glacier boundary layers violating some of the assumptions that are used to derive the bulk aerodynamic approach, the method has been shown to work well in glacierized environments (Denby and Greuell, 2000). One of the parameters used in the bulk aerodynamic approach, roughness length, is often used as a tuning parameter in DEBMs (e.g. Hock and Holmgren, 2005, Anslow et al., 2008, Anderson et al., 2010). A method to parameterize the evolution of this quantity for snow has been developed by Brock et al. (2006), which related roughness length to the logarithm of positive degree days since the last major snowfall event. To my knowledge this parameterization has yet to be implemented in a DEBM. The sensible heat released when rain is cooled to freezing point (Q_R) has been calculated by assuming that the rain is initially at air temperature and utilizing the sensible heat capacity of water (Hock and Holmgren, 2005). This flux is in many climates very small and is often disregarded in energy balance calculations (e.g. Anslow et al., 2008, Klok and Oerlemans, 2002).

1.2.2 Melt model transferability

Glacier melt models have been applied over vast regions by calibrating the models to well-studied glaciers and applying them unchanged over much larger areas (e.g. de Woul and Hock, 2005, Oerlemans et al., 2005, Raper and Braithwaite, 2006, Schneeberger et al., 2003). Empirical melt models have been applied at regional scales in which transferability in space and time must be assumed, despite evidence that such transferability is not universally possible (Hock et al., 2007, Hock, 2003). Physically-based melt models have not been used at regional scales in complex terrain. Two studies have specifically explored the transferability of melt-model parameters between glaciers within the same mountain range. Carenzo et al. (2009) explored the transferability of an enhanced temperature-index melt model (Pellicciotti et al., 2005) within the Swiss-Italian Alps. This study found the

model to be highly transferable between three glaciers in three summers, except when the model was calibrated separately for overcast and clear conditions. Wheler (2009) explored the transferability of the Hock (1999) enhanced temperature-index melt model within the Donjek Range of the St. Elias Mountains. He found a small reduction in model skill when transferring the model in space and high model transferability in time. Despite the advantage of being able to model the effects of climate change on individual components of the energy balance (Hock et al., 2007) DEBMs have not been used for regional studies, due to large data requirements and perceived complexity (Hock and Holmgren, 2005, Pellicciotti et al., 2005).

1.3 Objectives

The objective of this thesis is to take the first steps to applying a DEBM regionally by:

1. Creating DEBMs of two small glaciers in the Donjek Range of the St. Elias Mountains.

2. Assessing the spatial and temporal transferability of model parameters and meteorological driving variables between the two glaciers.

1.4 Study site

The St. Elias Mountains, located in northwestern North America, are characterized by extreme topographic gradients (Clarke and Holdsworth, 2002) and host one of the largest glacierized regions outside of the Arctic or Antarctic (Arendt et al., 2008). During the latter decades of the 20^{th} century, glaciers in southeastern Alaska and the Coast Mountains contributed more to sea-level rise than any other glacierized region (Kaser et al., 2006, Lemke et al., 2007). Within this region the greatest single contribution came from the glaciers of the St. Elias Mountains (Berthier et al., 2010). The fraction of these glaciers in the Yukon exhibit the third highest rate of glacier mass loss in the world (Barrand and Sharp, 2010). The Donjek Range is located in the southwestern Yukon Territory of Canada, at the eastern edge of the St. Elias Mountains just beyond the contiguous ice fields (Fig. 1.1 a.). The range is separated from the Gulf of Alaska by the highest peaks of the St. Elias Mountains,

and therefore, despite being less than 100 km from the ocean, experiences a continental climate (L'Heureux et al., 2004). This study is conducted on two unnamed mountain glaciers 10 km apart in the Donjek Range (Fig. 1.1 b). One glacier has a predominantly southerly aspect and a surge-type dynamic regime (De Paoli and Flowers, 2009) and is henceforth referred to as "South Glacier" (Fig 1.1 c). The other has a northwesterly aspect and is referred to as "North Glacier" (Fig. 1.1 d). South Glacier is thought to have a polythermal structure (De Paoli and Flowers, 2009) similar to that of Storglaciären in northern Sweden (Pettersson et al., 2004). The thermal regime of North Glacier is also presumed to be polythermal but has not been studied. The glaciers were chosen as focussed study sites among the $\gtrsim$20 mountain glaciers of the Donjek Range framed by the Kluane and Kaskawulsh outlet glaciers. These specific glaciers were selected for their opposing aspects, similar surface areas, independence from the large outlet glaciers, and to minimize hazards for field personnel. The two glaciers have been studied in detail from 2007–2009 with a full complement of instruments in the 2008 and 2009 field seasons.

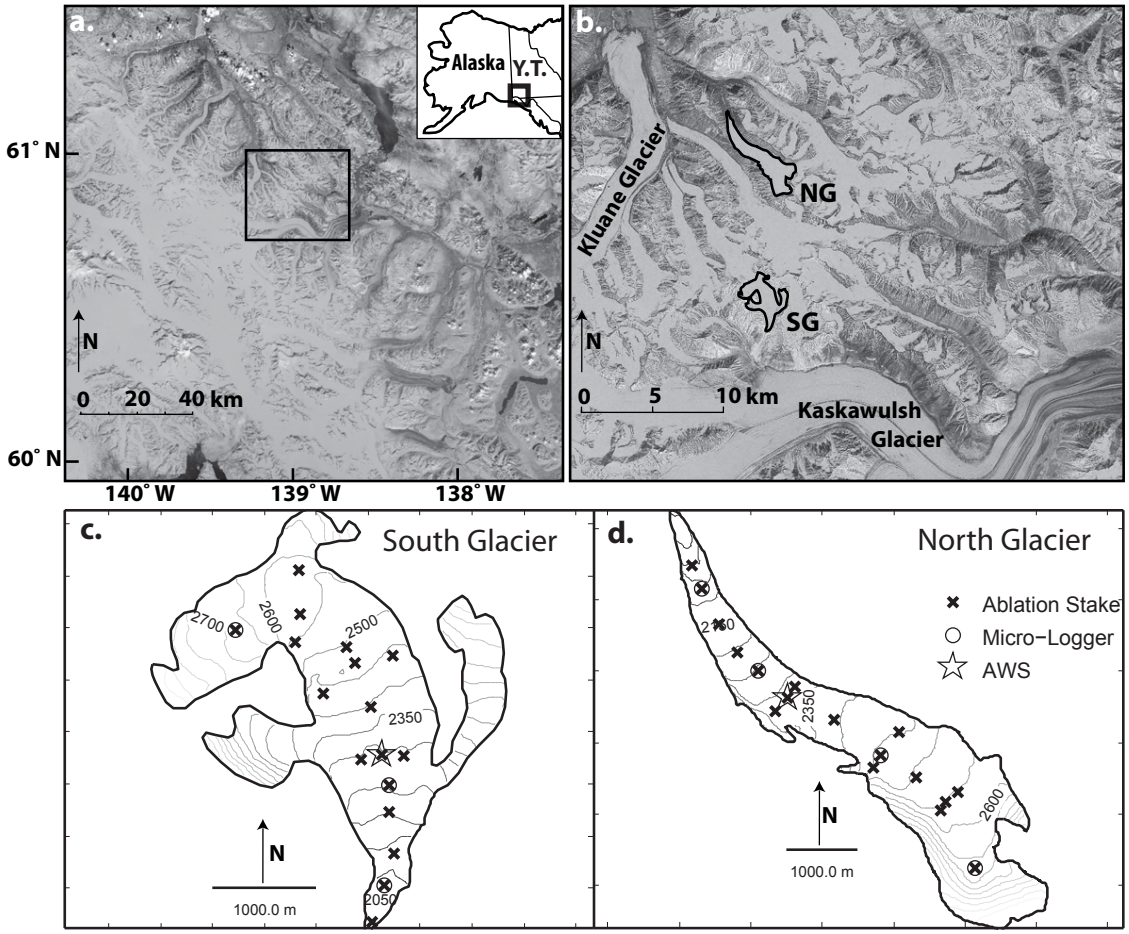

Figure 1.1: Map of study region. (a) St. Elias Mountains in southwest Yukon Territory, Canada (inset). Donjek Range study area is outlined. Images provided through NASA's Scientific Data Purchase Project and under NASA contract by Earth Satellite Corporation. (b) Donjek Range between Kluane and Kaskawulsh Glaciers. Study glaciers are outlined and labeled: "NG" for North Glacier, "SG" for South Glacier. (c) Surface contour map of South Glacier with locations of ablation stakes, AWS and micro-loggers. (d) As for (c) but for North Glacier.

1.5 Thesis Structure

This thesis is divided into eight chapters which describe the development and experiments conducted with a distributed energy balance melt model. *Field Methods and Data Processing* (Chapter 2) discusses the methods of data collection and processing of the data used to drive and validate the model. *Modelling Methods* (Chapter 3) introduces the physical basis and parameterizations of the distributed energy balance melt model. *Model Validation* (Chapter 4) examines model skill by comparing model output to validation data. *Sensitivity Testing* (Chapter 5) explores the sensitivity of the model to perturbations in model parameter and meteorological inputs. *Transferability Experiments* (Chapter 6) explores the transferability of model parameters and meteorological variables in space and time. *Discussion* (Chapter 7) discusses the implications of the model transferability experiments, and *Summary, Conclusions and Future Work* (Chapter 8) contains a summary of this thesis and conclusion drawn from the experiments within.

Chapter 2

Field Measurements and Data Processing

2.1 Overview

In this chapter I present the methods used in collecting and processing of field data utilized to drive and validate the distributed energy balance melt model (DEBM). Explained in detail are the methods used to: estimate mass balance from ablation stake and ultra-sonic depth gauge measurements, estimate aerodynamic roughness length using the microtopographic technique, and apply corrections to meteorological records.

2.2 Preparation of meteorological data

Meteorological data were collected by Campbell Scientific automatic weather stations (AWS) at two sites on South Glacier between 2006–2009 and one site on North Glacier between 2007–2009. One of the AWSs on South Glacier, located on debris-covered ice at the western margin of the glacier, records very similar data to that recorded by the AWS located on the glacier and will not be mentioned further. The two AWSs located on the glaciers are deployed with a parallel set of instruments (Table 2.1). Data from these AWSs needed to be gap filled and corrected to make them suitable for driving a DEBM.

Instrument records collected on various dates by downloading station data were con-

Variable	Instrument	Precision
Air Temperature	HMP45C212 TRH Probe	$\pm 0.28°C$
Relative Humidity	HMP45C212 TRH Probe	$\pm 4\%$
Wind Speed	RM Young 05103-10	$\pm 3\ m\,s^{-1}$
Wind Direction	RM Young 05103-10	$\pm 3°$
Surface Height (distance)	SR50 Sonic Ranger	$\pm 0.4\%$
Net Radiation	Kipp & Zonen NR-LITE	$\pm 5\%$
Barometric Pressure	RM Young 61205V	± 0.5 hPa
Shortwave Radiation	Kipp & and Zonen CMA6	$\pm 3\%$
Rainfall rate	TE525 Tipping Bucket Rain Gauge	0 to $-3\,\%$

Table 2.1: Instrumentation deployed at AWS locations on North Glacier and South Glacier. Instrument precision is taken from manufacturer's documentation. Rainfall for South Glacier was measured 500 m from AWS.

Event	Date or Range 2008	Date or Range 2009
Albedometer deployed	5 May – 11 September	9 May – 27 July
Snow-pits excavated	4 May	10 May, 12 May
First ablation stake survey	1 – 2 May	8 – 13 May
Final ablation stake survey	11 – 13 September	24 –25 July

Table 2.2: Date or date ranges of major data collection events for South Glacier. Except for the albedometer AWS instruments have recoded without interruption since summer 2006.

Event	Date or Range 2008	Date or Range 2009
Albedometer deployed	8 May – 14 September	18 May – 4 August
Snow-pits excavated	6 May, 8 May	15 May, 16 May
First ablation stake survey	6 – 7 May	15 – 16 May
Final ablation stake survey	15 September	4 August

Table 2.3: Date or date ranges of major data collection events for North Glacier. Except for the albedometer AWS instruments have recoded without interruption since summer 2007.

catenated and gaps in the data filed. No gap was longer than 30 minutes for the permanently deployed and undamaged instrumentation. Major data collection dates and date ranges are given in Table 2.2 for South Glacier and Table 2.3 for North Glacier.

2.2.1 Specific corrections

Ultra sonic depth gauge

Records from the Ultra sonic depth gauge (USDG), which measures the distance to the glacier surface, need to be corrected for temperature. The correction given in instrument documentation is:

$$d_s = d_{so}\sqrt{\frac{T_a + 273.15}{273.15}}, \tag{2.1}$$

where d_s is the distance to the surface, d_{so} is the original distance measured by the USDG and T_a is air temperature in °C. USDG data was further modified by replacing the error reading 0 with a linearly interpolated value between non-zero measurement. Resets of the stakes on which the USDG rests (which will melt out in time) were manually removed by flagging the time steps when field notes indicate resets occurred and by adding the magnitude of the reset to all measurements after the reset.

Net Radiation

Net radiation measurements need to be corrected for high wind speeds. If wind speed is below $5\,\mathrm{m\,s^{-1}}$ no change is made, otherwise:

$$Q_N = Q_{No}(1 + 0.021286(u_z - 5)), \tag{2.2}$$

where Q_N is net radiation, Q_{No} is the original net radiation reading and u_z is wind speed in $\mathrm{m\,s^{-1}}$. Net radiation records exhibit spurious values of very negative net radiation that last for only one five minute time-step. Therefore values below $-300\,\mathrm{W\,m^{-2}}$ were replaced by linearly interpolated values between reliable data points.

Shortwave Radiation

Shortwave radiation records need to be corrected for the effect of tilting of the AWSs that occurs due to differential melt under the tripod legs. Only incoming direct shortwave ra-

diation is effected by small changes in the tilt of the sensor, as all other components of shortwave radiation are omnidirectional in origin (Jonsell et al., 2003). The effect of sensor tilt on recorded incoming shortwave radiation is the same as the effect surface slope and aspect have on incident radiation on non-flat topography. As this relationship is well known it is trivial to derive the correction to be applied to a tilted sensor. The correction is,

$$\cos\theta = \cos Z \cos\beta + \sin Z \sin\beta \cos(a - A), \tag{2.3}$$

$$I = I_o \frac{\cos\theta_h}{\cos\theta_t}, \tag{2.4}$$

where θ is the incident angle of the solar beam, Z is the solar zenith angle, β is the surface slope or tilt, A is the aspect of the slope or tilt measured with south as zero, a is the azimuth angle from south, I is the direct shortwave radiation, I_o is the observed direct solar radiation, θ_h is the incident angle on a horizontal surface and θ_t is the incident angle on the tilted (or sloped) surface.

Field records indicate that no significant tilting of the shortwave radiation sensor occurred on either glacier in 2008 and on South Glacier in 2009. The sensor on North Glacier was tilted 6° to the south from horizontal when retrieved on the 4$^{\text{th}}$ of August 2009. The tilt was corrected by assuming a constant tilt rate since the instrument was leveled in May 2009 and breaking up diffuse and direct radiation using the method of Hock and Holmgren (2005). A tilt of 6° to the south only creates a 7.5% positive bias in incoming direct shortwave radiation under the most detrimental conditions: summer solstice at noon at the latitude of North Glacier. The effect would have been much larger closer to the equator.

The slope of the glaciers at the AWS locations is not horizontal and therefore the horizontally leveled albedometers are not surface parallel. Albedo readings that are not parallel to the surface exhibit complex and spurious daily variations in albedo (Jonsell et al., 2003). To compensate for this effect integrated daily albedos are used, where daily integrated incoming and reflected shortwave radiation measurements are used to calculate a single daily value of albedo following Oerlemans and Knap (1998).

Wind

The wind monitor on North Glacier was destroyed during the winter of 2008 and could not be replaced until June of that year. To compensate for this gap in the wind record

wind speeds were simulated using the katabatic coefficient developed by Oerlemans and Grisogono (2002) which relates wind speed to glacier temperature for positive glacier temperatures. The parameterization is based on the study of melt-generated down-glacier katabatic winds (Oerlemans and Grisogono, 2002). The model is a simple linear relationship between wind and temperature,

$$u_z = K_c(T_a - T_f), \tag{2.5}$$

where u_z is wind speed, K_c is the Katabatic coefficient, T_a is air temperature and T_f is the freezing threshold taken as the standard 0 °C. When temperatures are below freezing, wind speed is assumed to be zero. Measurements of wind speed are only needed when the glacier is melting which is almost exclusively when temperatures are above freezing.

The best-fit katabatic coefficient was found to be $0.404\,\mathrm{m\,s^{-1}\,K^{-1}}$ for wind data collected in 2007–2009. This relationship has a correlation coefficient R of 0.54. The simulation augmented wind record is shown in Figure 2.1.

2.3 Temperature lapse rates

Three (four) Onset Hobo^{TM} micro-loggers are deployed on South (North) Glacier at various elevations (Fig. 2.2, 2.3). These micro-loggers measure temperature and relative humidity. Temperature records for each of the mirco-loggers is averaged and a linear regression on elevation is used to estimate the temperature lapse rates. The lapse rate for South Glacier 2008 and South Glacier 2009 is $-6.0\,\mathrm{K\,km^{-1}}$ and for North Glacier 2008 is $-5.3\,\mathrm{K\,km^{-1}}$. The temperature lapse rate for North Glacier 2009 could not be derived due to sensor malfunction and is therefore assumed to be the same as North Glacier in 2008.

2.4 Ablation Stake Measurements

2.4.1 Introduction

The direct glaciological method is the oldest and simplest method of observing accumulation and ablation on a glacierized surface (Paterson, 1994). The method is implemented

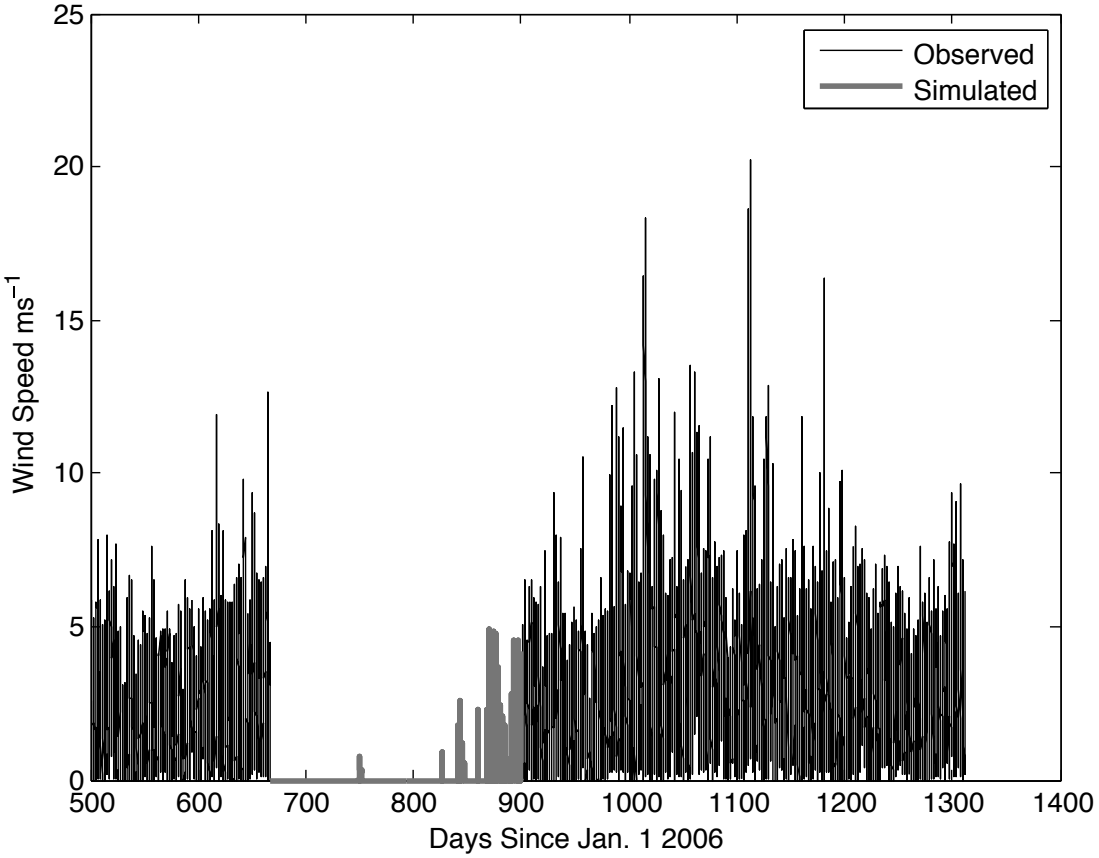

Figure 2.1: Observed and simulated wind speed on North Glacier. Simulated values are in grey and were necessary to replace measurements lost due to instrument destruction.

by deploying an array of stakes drilled into the glacier surface and making repeated measurements of stake height to find the change in surface height over time. By measuring the density of the surface at the time of each stake height measurement one can transform the height measurements into water equivalent (w.e.) ablation or accumulation. Although this method if straightforward to implement it is subject to large uncertainties originating from errors in stake height measurement, error in surface density measurements and errors in the spatial representativeness of stake measurements (Paterson, 1994).

During the summer of 2006 (2007) an array of 18 (17) ablation stakes was deployed on South (North) Glacier. These stakes have been measured at least twice a year up to and including summer 2009 to gauge accumulation and ablation on the two glaciers. Here we describe how raw stake data are processed into usable w.e. accumulation and ablation estimates and how finite error estimates are placed on these measurements. Only results from the 2008 and 2009 field seasons are discussed. Earlier seasons have been examined previously by Wheler (2009).

2.4.2 Notation to be used

Each ablation stake is named according to its location on the glacier. Stakes deployed longitudinally on the glacier centre line are designated “L", stakes deployed transverse to the glacier flow line are designated “T", stakes located at meteorological stations are named after the station. The four stakes located at micro meteorological Onset-Hobo^{TM} stations are designated “H", the stake located at the mid-glacier meteorological station is designated “MM" and the stake at the high elevation meteorological station is designated “HM". Stakes are assigned numbers based on their elevations with numbering starting at the lowest elevation stake, such that the stake at the terminus is L01. Where two transverse stakes are at the same elevation the stake on glacier right is given the lower number. See figures 2.2 and 2.3 for the locations of the stakes on each glacier.

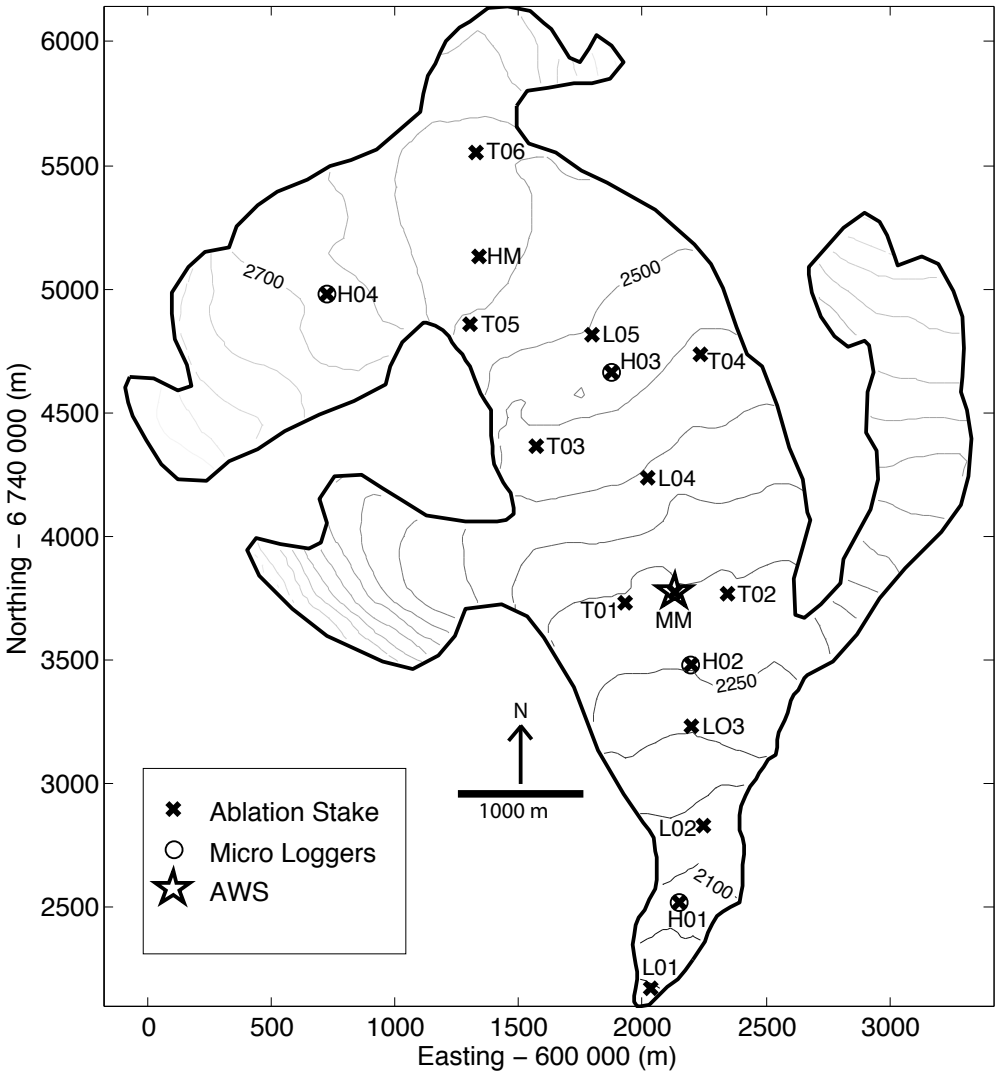

Figure 2.2: Location of ablation stakes, micro loggers, and AWS on South Glacier.

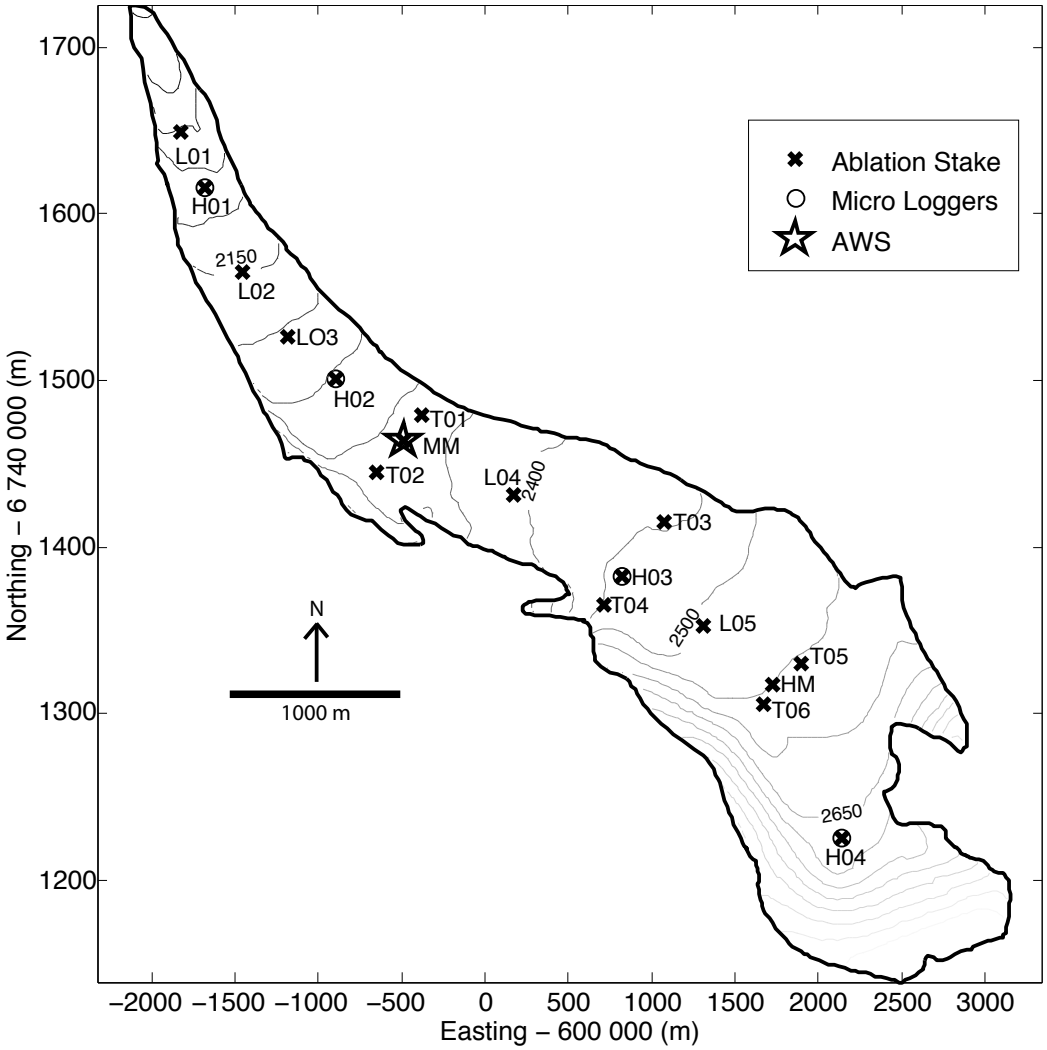

Figure 2.3: Locations of ablation stakes, micro loggers, and AWS on North Glacier.

2.4.3 Estimating accumulation

Snow depth was measured at each stake location in May of 2008 and 2009. Three depth measurements were made near each stake and averaged to estimate local snow depth. At the AWS location and the high glacier temporary meteorological station location snow pits were excavated and density-depth measurements taken. In each snow pit measurements were taken of the density of regular 10cm thick layers. The data was integrated into an average density as follows.

$$\rho_s = \frac{\sum \triangle d_i \triangle \rho_i}{\sum \triangle d_i}, \tag{2.6}$$

where ρ_s is the integrated snow pit snow density, $\triangle d_i$ is the thickness of the i^{th} snow layer, and $\triangle \rho_i$ is the density of the i^{th} snow layer.

To transform snow depth measurements at stakes into w.e. snow depth the integrated snow pit densities were extrapolated to the stakes on South Glacier by assuming that each snow pit was representative of the nearby region of the glacier. The snow pit density from the AWS location were used at stakes MM, H01, H02, L01,L02, L03, T01 and T02, the snow pit density from the high elevation temporary meteorological station were used at HM, H04, L05, L06, T05, and T06; a mean of the two snow pit densities were used at stakes H03, T03, T04 and L04. The same extrapolation was carried out on North Glacier with the exception that there is no L06 on North Glacier.

Water equivalent snow depths were extrapolated to all digital elevation model (DEM) grid points on both glaciers by using the snow depths at stake locations to perform a linear regression. Regression of snow depth on elevation and snow depth on slope was carried out to find statistically significant relationships between these independent variables and snow depth. On South Glacier there was a statistically significant relationship between snow depth, elevation and slope. On North Glacier there was only a statistical relationship between snow depth and elevation. See Table 2.4 for regression parameter values and correlation coefficients. See Figures 2.4 for maps of w.e. snow depth in May 2008 and 2009 on North and South Glacier.

Using the extrapolated snow depth data it is trivial to compute winter balance. The winter balance is simply the area averaged snow depth across a glacier surface. Winter balance for South Glacier was 33 cm w.e. in 2008 and 53 cm w.e. in 2009. Winter balance for North Glacier was 23 cm w.e. in 2008 and 38 cm w.e. in 2009. These estimates assume

that the spring field campaign coincides with peak winter accumulation. Although the spring field companied is planed to capture this peak, inter-annual variation means that this timing is only approximate. In particular in 2008 large snowfalls where recoded by the USDG after the spring field campaign.

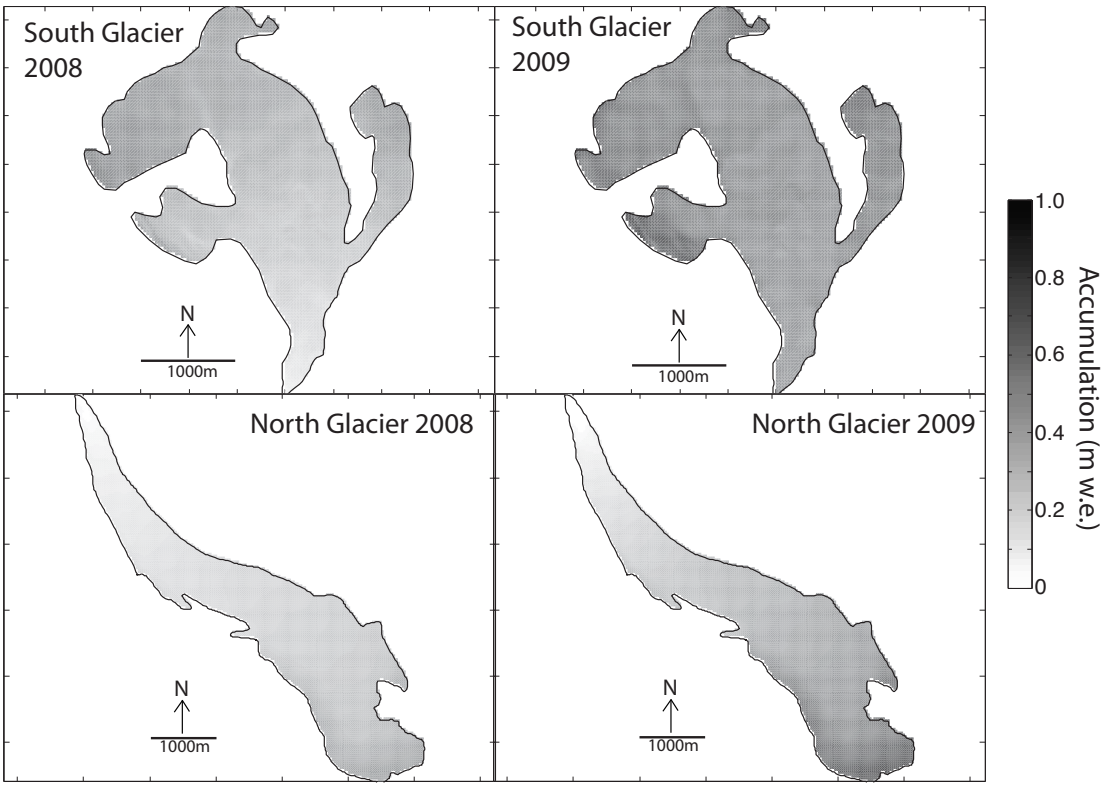

Figure 2.4: Water equivalent snow (m) for May of 2008 and 2009 for North Glacier and South Glacier.

2.4.4 Estimation of Ablation

To estimate ablation at stake locations two quantities must be measured or estimated: the change in the height of the stake since the last measurement, and the density of the material that has melted since the last measurement. Estimating the density of material melted requires several steps. I classify the glacier surface as either new snow, densified old snow,

Table 2.4: Results of w.e. snow depth regression. Table shows linear regression parameters for elevation, slope and intercept, and R correlation coefficient. Also included is winter surface accumulation (C_w) for both glaciers in 2007–2008 (S08, N08) and 2008–2009 (S09, N09).

	S08	S09	N08	N09
Intercept (cm)	-89.57	4.76	-69.37	-135.52
Elevation Coef. (w.e. cm m^{-1})	0.051	0.027	0.037	0.070
Slope Coef. (w.e. cm per $^\circ$)	-0.309	- 0.322	–	–
R	0.58	0.20	0.57	0.83
C_w (w.e. cm)	33	53	23	38

soft firn, hard firn or ice. Each of these materials has a unique density range, although the densities ultimately form a continuum that represents the transformation of snow into ice (Paterson, 1994). Density measurements were made of the surface material during stake surveys, whenever possible. When these measurements were not made, due to for example a solid surface, typical values were used. Ice was taken to have a density of 900 kg mw^{-3} and hard firn was taken to have a density of 800 kg m^{-3} (Paterson, 1994). Typical values of new snow and old snow were estimated as the mean of the measured values for samples of these types. The density of soft firn was measured each time it was encountered.

we calculate the w.e. ablation as:

$$\triangle b = \frac{\rho_g \triangle H}{\rho_w}, \tag{2.7}$$

where $\triangle b$ is the change in w.e. snow or ice thickness, ρ_g is the density of the melted material and ρ_w is density of water taken as 1000 kg m^{-3}. For snow and soft firn ρ_g is taken as the mean values measured at time t and $t-1$. Over much of the glacier surface there will at some point in the summer be a transition from snow surface to ice or firn surface. This is accounted for by breaking the calculation of w.e. ablation in two. In the first part density is taken as the last measured value, or if the last measurement was at the beginning of the summer, as the extrapolated snow pit density at that stake. The change in height is taken as the measured snow depth during the last survey. In the second part

the density is taken as that of the uncovered surface, firn or ice, and the change in height is the calculated by subtracting the snow depth measured during the previous survey from the change in hieght.

The estimates of melt between each survey are added to find cumulative melt. Starting from either the first measurement of the year, or the first measurement after a stake has been reset. If the stake has been reset without melting out completely the change in height due to the reset is simply disregarded in above calculations.

2.4.5 Errors in ablation

Uncertainties are assigned to calculated values of w.e. ablation by estimating error in both height and density. Error estimates for the height measurements were made at the time of the stake survey by estimating the variability in surface height using a 30 cm $\times$ 30 cm "Ablation Disk" placed at the base of the stake. Where this estimate of error was not made, an error of $\pm$5 cm is assumed. Error estimates for density were made based on the surface material and method used to estimate density. The error in ice and hard firn density were assigned from the range of reported densities for these materials found in Paterson (1994). For ice the error is taken as $\pm$2% and for hard firn it is $\pm$6%. Error estimates for the snow pit density, surface snow density, and snow depth were taken from Wheler (2009) and are $\pm$10%, $\pm$15%, and $\pm$10% respectively. Assigned unmeasured snow densities were given an error estimate of $\pm$30% encompassing the range of values measured in the field.

Errors in density and height were combined using standard error propagation. The error in w.e. ablation is

$$E_b = \sqrt{E_h^2 + E_\rho^2}, \tag{2.8}$$

where E_b is the relative error in ablation, E_h is the relative error in stake height and E_ρ is the relative error in density.The error in cumulative ablation is calculated similarly except using absolute errors. As expected when using the direct glaciological method, errors in ablation can be large.

2.5 Estimating Surface Accumulation and Ablation using a USDG

The Ultra Sonic Depth Gauge (USDG) deployed near the AWSs on North Glacier and South Glacier measures the distance to the surface of the glacier every half hour. By estimating the density of the surface at every time step this record is used to create a continuous estimate of mass balance at the AWS locations. The method employed to make this estimate involves several steps. To eliminate noise daily averages are taken of the distance to surface measurements. Differences are taken between each daily average, positive difference (when distance to the surface is reduced) are interpreted as snow fall events, negative differences are interpreted as ablation events. Snowfall events are assigned a density of $200\,\mathrm{kg\,m^{-3}}$ (Paterson, 1994). If the next ablation event is less than the snowfall event the ablation is assigned a density of new snow. If the next ablation event is greater than the remaining snow from the snowfall event a density is a assigned which is a weighted average of the density of new snow and the spring snow pit density at the AWS. If there is no new snow the density is assigned as the spring snow pit density at the AWS. If net ablation has exceeded the initial snow pit depth the density of ice ($900\,\mathrm{kg\,m^{-3}}$ (Paterson, 1994)) is used instead of the snow pit density.

The cumulative density weighted positive differences are total surface accumulation. Cumulative density weighted negative differences are total surface ablation and cumulative density differences are total surface point mass balance (Figure 2.5.)

Two assumptions are made when interpreting USDG records as a mass balance record that are at times untrue in glacierized environments. One assumption is that there is no wind redistribution of snow. This assumption is a good approximation in the summer season when snow is too wet to become airborne, but can be a poor assumption early and late in the summer season when weather can change from well above freezing to well below freezing on synoptic time-scales. The other assumption is that there is no densification of the snow pack. This is clearly false, however, because the initial mass of the snowpack is known from the snow pit measurements and because mass is conserved in the densification process, the estimated cumulative ablation from surface lowering and real ablation will converge when the snowpack has melted completely. Therefore interpretations of ablation should be taken with caution when a snowpack is present. The daily averaging necessary

to suppress noise in the record means that snowfall events that ablate in less than a full day will not be recorded.

The USDG on North Glacier was inoperative for much of the summer of 2008. The snowfall records for this time where replaced by the records from the Duke River AWS (One of three additional AWSs located in the Donjek Range). Snowfall events at the Duke River AWS are highly correlated with those on North Glacier with an R^2 coefficient of 0.88.

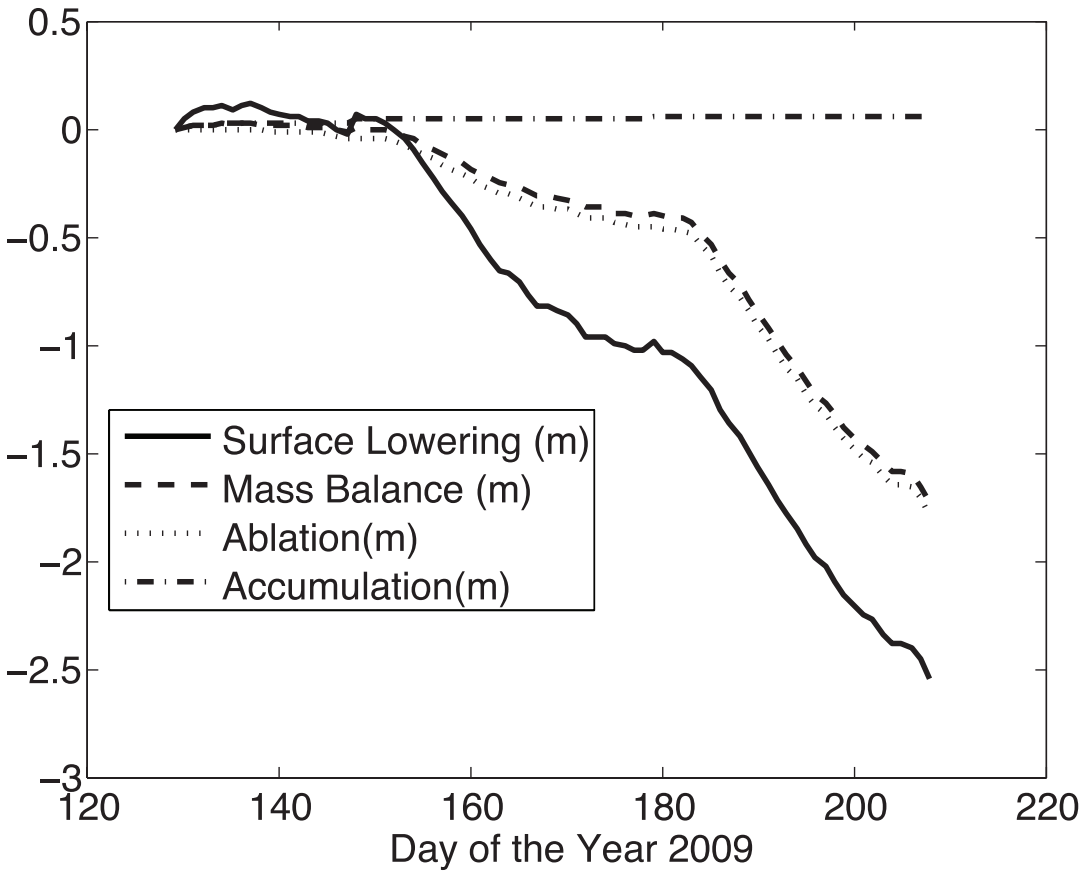

Figure 2.5: USDG recorded surface lowering and estimated surface ablation, surface accumulation, and mass balance. South Glacier 2009.

2.6 Aerodynamic roughness length

2.6.1 Introduction

Aerodynamic roughness length is the height above the ground at which wind speed reaches zero. This quantity is needed for the calculation of turbulent heat fluxes and can be estimated from the microtopography of a surface (Munro, 1989). In the spring and summer of 2009 repeat microtopographic surveys were carried out on both North Glacier and South Glaciers in an attempt to characterize roughness length and to fit a time-evolving model of snow surface roughness developed by Brock et al. (2006). Microtopography was measured using two methods: the backdrop method in which a black backdrop was inserted into snow or soft firn and a digital photograph taken of it, and the "string method" in which a black string is laid on the ice surface and a digital photograph is taken of it. The backdrop method was developed by Rees (1998) and the string method was developed for this project.

2.6.2 Characterization of microtopography

The microtopographic approach is based on the work of Lettau (1969) and Munro (1989); it involves measuring the actual roughness of the surface. This is accomplished by laying either a pole or a taught string across the surface, perpendicular to the prevailing wind direction, and measuring the distance from the pole to the surface at regular spatial intervals. These measurments are used to compute a roughness length z_o as

$$z_o = 0.5h^* \frac{s}{S}, \tag{2.9}$$

where h^* is the effective height of the roughness elements, interpreted as twice the standard deviation of the height measurement, s is the cross-sectional area of an effective roughness element and S is the inverse of the roughness element density. s and S are

$$s = h^* \frac{X}{2f}, \tag{2.10}$$

$$S = \left(\frac{X}{f}\right)^2 \tag{2.11}$$

where X is the length of the string or pole and f is a measure of the frequency of microtopographic elements, defined as the number of continuous groups of positive deviations from the de-trended surface profile.

Rather than measuring surface heights from a pole Rees (1998) took a digital photograph of a black backdrop inserted into the snow surface. Brock et al. (2006) established that the microtopographic approach produced roughness lengths within the error envelope of the direct wind profile method.

2.6.3 Backdrop method

The backdrop method captures a 1-D profile of the snow-air interface by taking a digital photograph of the boundary between snow and a backdrop inserted into the snow surface (Figure 2.6). The photographs are digitized into (x,y) coordinate pairs using the software package ImageJ. ImageJ is a photograph analysis software package developed by the United States National Health Service, is native to Mac OSX and is released to the public under a GNU license (Rasband, 1997–2009).

To extract a microtopographic profile the digital photograph is opened with ImageJ and the length of the backdrop in pixels is recorded. The photo is converted into black and white using the *Make Binary* function. The section of the photo that contains the snow-backdrop interface is copy-pasted into a new window. The *Find Edge* function is used to find the boundary between the backdrop and the snow. At this point automatically selected but unwanted pixels resulting form of snow stuck to the backdrop, damage to the backdrop's duct tape coating or artifacts from the copy-paste process must be manually erased. The profile of the snow surface is exported to an ascii file containing (x,y) coordinates of white (or black) pixels using the *Save as (X,Y)* function.

A Matlab script is used to calculate a aerodynamic roughness using the method of Munro (1989). Before this method can be used the data must be converted to length in mm using the recorded pixel length of the backdrop and the known length of the backdrop (1 m). The data are linearly de-trended to emulate the effect of taking measurements from a pole laying on a surface and reduced in resolution to prevent spurious counts of frequency created by sub-millimeter scale noise in the profiles.

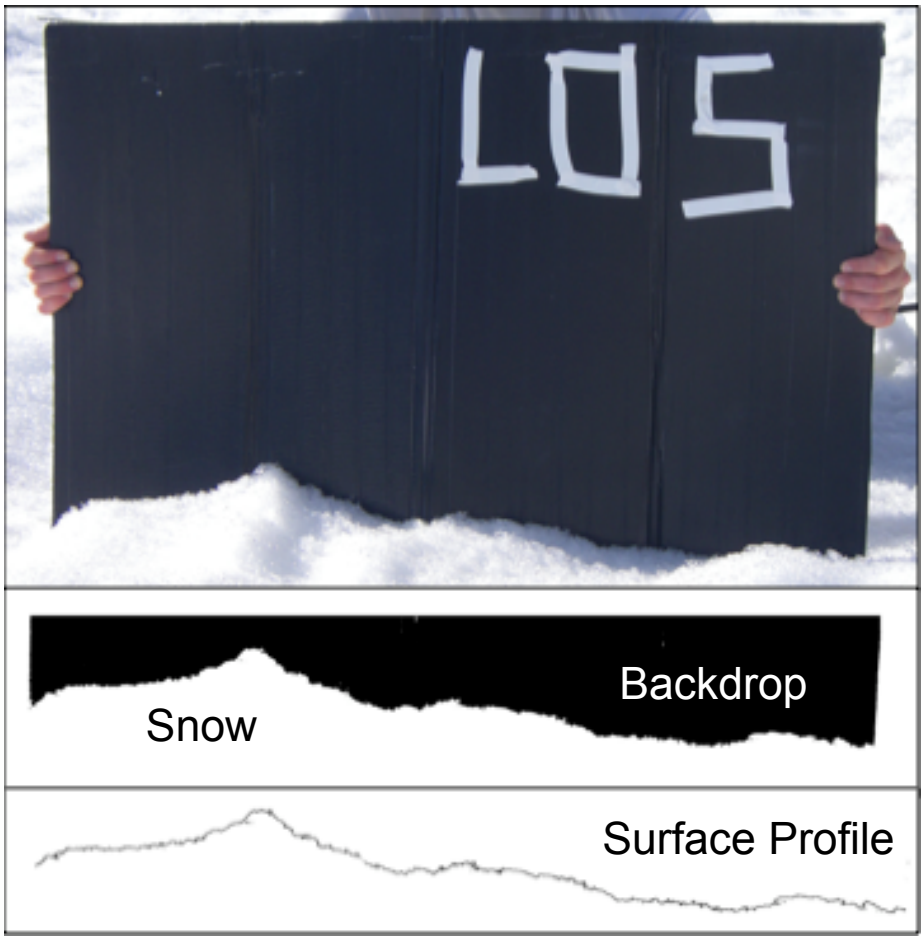

Figure 2.6: Example of digital photograph taken of black backdrop used to capture surface microtopography and the steps in isolating the surface profile.

2.6.4 String Method

The string method was developed to capture the outline of hard surfaces into which a backdrop cannot be inserted, namely ice and hard firn. The method works by laying a string along the surface such that it forms a profile of the surface. A digital photograph is taken of the string in a plane perpendicular to the surface and parallel to the axis of the profile. The string is attached to a 1 m long stick which is placed just behind the string for scale and is used as a guide to keep the string in a straight line when viewed parallel to the surface (Figure 2.7).

The photos are loaded into ImageJ and the length of the stick is recorded in pixels. The section of the photo containing the string is copy-pasted into a new window and the *Threshold* function is used to convert the image into black and white. Unwanted pixels resulting from dark background patches, dirt and the stick must be erased.

The profile produced is loaded into Matlab, converted to length in mm and linearly detrended. The resolution of the profile is reduced to remove spurious frequency counts and the profile is converted into a roughness length using the method of Munro (1989).

2.6.5 Error in the photographic method

There are several sources of error in the backdrop and string methods of determining surface roughness. If the image is not taken in a plane perfectly parallel to the backdrop or string part of the profile will be closer to the camera creating a parallax effect. This creates a spurious slope in the profiles that is removed during linear regression, but also means that the roughness elements closer to the camera seem larger those further away. This effect is reduced because the roughness elements are defined in the method of Munro (1989) as twice the standard deviation of elevation of all recorded points meaning the spuriously large elements compensate for the spuriosly small elements. The effect of parallax is small at small angular deviations from parallel and is proportional to the ratio of distance from the camera to each point.

Deviations of the string from a straight line in the plane perpendicular to that of measurement create false variation in the profile. As long as these deviations are much smaller

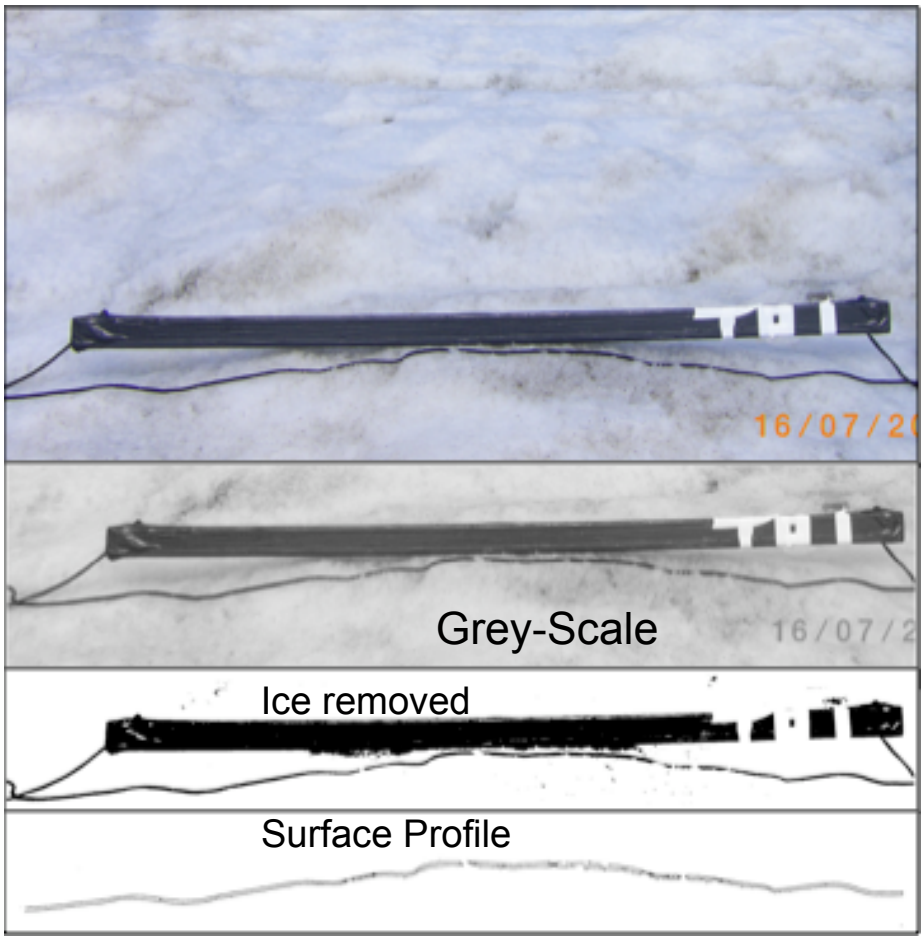

Figure 2.7: Example of digital photograph taken of a black string used to capture surface microtopography and the steps in isolating the surface profile.

than the real roughness elements their effect should be minimal. The string method is also affected by features in the photograph that obscure the string from view, including near-camera roughness elements and narrow deep depressions. These occlusions mean that the string profiles are not always continuous and that some variability may be missing when roughness lengths are computed. Very dark ice can also have a similar effect making it impossible to distinguish the string from the background effectively removing parts of the profile. Crenulations in the backdrop itself can cause false roughness readings. Severely distorted photographs were discarded and not processed.

2.6.6 Comparison of string method and traditional microtopographic method

The traditional microtopographic method of estimating roughness length is carried out by laying a pole on a surface and measuring the distance between the pole and the ground at regular intervals to create a linearly de-trended profile of the surface. At seven points on South Glacier on the 23rd of July 2009 the tradition method of measuring microtopographicly-derived roughness length was compared to the string method. At these sites a 3 m pole was laid on the ice surface and the distance to the surface was measured at 10 cm intervals. In the same locations the string method was used by laying out the string underneath the pole. The length of the pole meant that two photographs had to be taken at each pole location. This complicated later analysis as the two photos needed to be stitched together for direct comparison of the string method and the pole method.

The traditional profile were processed using the method of Munro (1989). The pole method does does not require de-trending as laying a pole on the ground compensates for the average slope of the surface (Table 2.5).

The string method systematically underestimates that roughness length computed using the pole method (Table 2.5). This may be an effect of occlusions and deep narrow depressions obscuring part of the string profile or may be related to the low sampling frequency of the pole method. Fortunately the bulk aerodynamic approach for computing turbulent heat fluxes, that uses roughness length as a parameter, has a low sensitivity to estimates of roughness length as it contains the natural logarithm of roughness length not roughness length itself.

Table 2.5: Aerodynamic roughness length derived using the string method and the pole method of capturing a surface profile.

Site	Pole z_o (mm)	String z_o (mm)
L01	1.3746	1.1835
H01	2.1864	1.5919
L02	0.5567	0.2320
L03	2.5804	2.3280
H02	2.5252	1.8886
MM	3.8032	1.3770
T02	1.5140	0.9358

2.6.7 Roughness length and scale of measurement

It has been well established that microtopographic roughness length has a dependency on the length of the pole, string or backdrop used to measure it (Rees and Arnold, 2006). The effect has been shown to be small for the length of measuring device typically used on glaciers, but could still have an effect at the 1 m scale used in this project (Brock et al., 2006). To explore this sensitivity the 3 m-long profiles created for the pole and string method comparison were subsampled at logarithmic scale intervals to see if a pattern emerged. It was found that the roughness of the 3 m profile was most similar to the maximum roughness of the 1 m profiles. Therefore taking the maximum roughness observed at each site during stake surveys may be more appropriate that taking the mean or median of the measurements at each site.

Chapter 3

Modelling Methods

3.1 Overview

In this chapter I introduce the physical relationships and parameterizations that are used to compute each of the components of the surface energy balance of ice and snow for this study. I also describe how these energy balance components are extrapolated to each grid point on the glacier surface to create the distributed energy balance melt model (DEBM).

3.2 Distributed surface energy-balance melt model

Energy balance melt models calculate melt by measuring or parameterizing all of the components of the surface energy balance of ice or snow, leaving only energy available for melt as a residual. The surface energy balance of ice is written as:

$$Q_M = (S_{\text{in}}(1-\alpha) + L_{\text{in}} - L_{\text{out}}) + Q_H + Q_L - Q_g + Q_R, \tag{3.1}$$

where S_{in} is incoming shortwave radiation, α is the albedo of the ice or snow surface, L_{in} is the incoming longwave radiation and L_{out} is the outgoing longwave radiation. Q_H is the sensible heat flux, the energy exchanged between the glacier and the atmosphere. Q_L is the latent heat flux, the heat transferred to or from the glacier through sublimation, deposition, evapouration or condensation. Q_g is the heat transferred to and from the glacier subsurface when the ice or snow of the subsurface changes temperature. Q_R is heat from rain, the

sensible heat released when rain is cooled to the freezing point. Q_M is the energy available to melt ice. The sensible heat transfered to the glacier from the cooling of rainfall to the freezing point (Q_R) is disregarded, as above-freezing rainfall totals are small for the Donjek Range study glaciers. A distributed energy balance melt model (DEBM) extrapolates each component of the energy balance to a grid covering the glacier surface, such that energy available for melt can be found at each point.

The DEBM created for this study is similar to those created by Hock and Holmgren (2005) and Anslow et al. (2008). New innovations in this DEBM are (1) a new simple subsurface model for calculating surface temperature and subsurface flux, and (2) incorporating a time evolving parameterization for snow aerodynamic roughness length.

3.3 Shortwave Radiation

Incoming and reflected shortwave radiation are measured at the AWSs located on each glacier. To extrapolate measured incoming shortwave radiation to each DEM grid point S_{in} is broken into direct and diffuse components using the empirical relationship of Collares-Pereira and Rabl (1979). Diffuse shortwave radiation is applied to all grid points taking into account the fraction of the visible sky at each grid point. Direct shortwave radiation is applied to grid points that are not shaded by surrounding topography and is corrected for the slope and aspect of the grid cell.

The empirical relationship found by Collares-Pereira and Rabl (1979) relates the ratio of diffuse shortwave radiation D over incoming shortwave radiation S_{in} to the ratio of incoming shortwave radiation over incident radiation at the top of the atmosphere I_{toa}. The relationship was originally derived for assessing solar power potential based on observation in the continental United States. Hock and Holmgren (2005) re-derived the relationship using data from Sweden, finding parameter values near identical to those of Collares-Pereira and Rabl (1979) despite the differences in climate, topography and latitude between the two regions. Here we use the parameter values found by Hock and Holmgren (2005) as follows,

$$\frac{D}{S_{\text{in}}} = \begin{cases} 0.15 & : \frac{S_{\text{in}}}{I_{\text{toa}}} \geqslant 0.8 \\ 0.929 + 1.134\frac{S_{\text{in}}}{I_{\text{toa}}} - 5.111(\frac{S_{\text{in}}}{I_{\text{toa}}})^2 + 3.106(\frac{S_{\text{in}}}{I_{\text{toa}}})^3 & : 0.15 < \frac{S_{\text{in}}}{I_{\text{toa}}} < 0.8 \\ 1.0 & : \frac{S_{\text{in}}}{I_{\text{toa}}} \leqslant 0.15 \end{cases} \tag{3.2}$$

If the AWS is shaded by surrounding topography all measured incoming shortwave radiation is assumed to be diffuse. The ratio of diffuse to incoming shortwave radiation is assumed to stay constant until the next time-step at which the AWS is unshaded. This ratio is used to estimate direct shortwave radiation for the period of AWS shading (Hock and Holmgren, 2005).

3.3.1 Direct Shortwave Radiation

Direct shortwave radiation is only incident on grid points that are unshaded by surrounded terrain. At each time-step topographic shading is calculated using the traverse of the sun through the celestial hemisphere and the local horizon at each grid cell. The local horizon at each grid point is calculated using DEMs of the topography surrounding each glacier and by taking into account the curvature of the Earth. For every grid point at every time-step the position of the sun is calculated. If the sun is above the local horizon the gird is unshaded. If the sun is below the local horizon the grid is shaded.

Direct shortwave radiation is corrected from the measured horizontal to the slope and aspect of each grid point following Oke (1987),

$$I_{\text{e}} = I\frac{\cos\theta}{\cos\theta_{\text{h}}}, \tag{3.3}$$

where I is the direct shortwave radiation, I_{e} is the direct shortwave radiation effective on each grid point, θ is the incident angle of the sun on the surface and θ_{h} is the incident angle of the sun on a horizontal surface. The incident angle is found using well known astronomical theory,

$$\cos\theta = \cos Z\cos\beta + \sin Z\sin\beta\cos(a - A), \tag{3.4}$$

where

$$\cos Z = \sin\varphi\sin\delta + \cos\varphi\cos\delta\cos h_r, \tag{3.5}$$

where Z is the zenith angle of the sun, β is surface slope from the horizontal, a is the azimuth angle of the sun from south, A is the aspect of the surface, φ is geographic latitude, δ is the solar declination and h_r is the hour angle of the sun.

3.3.2 Diffuse shortwave radiation

Diffuse radiation is assumed to originate from all parts of the sky equally. This assumption is false under clear-sky conditions when diffuse radiation makes up only a small fraction of shortwave radiation but is approximately correct in cloudy conditions when diffuse radiation makes up the majority of the incoming shortwave radiation (Oke, 1987). There are two sources of diffuse shortwave radiation incident on each grid point: that incident from the unobscured fraction of the sky, and that reflected by surrounding terrain. Diffuse shortwave radiation is calculated as

$$D = D_o V_f + \alpha_{\text{ter}} S_{\text{in}} (1 - V_f), \tag{3.6}$$

where D_o is the diffuse radiation from an unobsured sky, α_{ter} is the albedo of the surrounding terrain and V_f is the sky-view factor, the fraction of the sky that is unobscured by topography. Sky-view factor is defined by Oke (1987) as

$$V_f = \frac{1}{2\pi} \int_0^{2\pi} \cos^2(\gamma)\, d\varphi, \tag{3.7}$$

where γ is the elevation angle of the horizon and φ is azimuth of the horizon. Numerical integration of the local horizon was carried out at 15° intervals to find the sky-view factor for every grid point. The albedo of the surrounding terrain was estimated in the field by measuring the albedo of rock slabs that had fallen from nearby slopes. The effect of snow cover on surrounding slopes is ignored as snow is rarely present on surrounding slopes during the summer season. The measured shortwave radiation at the AWS already includes the effects of surrounding terrain, therefore D_o must be backed out of Equation 3.6.

3.3.3 Albedo

The measured albedo on South Glacier and North Glacier range from 0.15–0.9. Given this range of albedo values and the dominance of net radiation in the energy balance of both glaciers, the accuracy of the parameterization of albedo evolution is the most important

component of modelling mass balance in this study. This sensitivity to albedo has been confirmed and quantified by sensitivity tests (see *Sensitivity Tests*).

Many parameterizations have been proposed for modelling the evolution of snow albedo throughout a melt season (e.g. Hock and Holmgren, 2005, Brock et al., 2000a, Oerlemans and Knap, 1998, Arnold et al., 1996). I find the parameterization developed by Hock and Holmgren (2005) gives the best fit to the measured albedo at our AWS locations (Figure 3.1) and therefore use a slightly altered version of this parameterization in the DEBM. The parameterization of Hock and Holmgren (2005) relates the change in the albedo of snow in each time-step to temperature, time since the last snowfall, the rate of snowfall and four rate controlling constants. The change in albedo is added to the albedo in the previous time step to find the current albedo. The parameterization is written as:

$$\alpha_t = \begin{cases} \alpha_{t-1} - a_1 \left[\ln(T+1)\right] e^{\left(a_2\sqrt{n_d}\right)} & \text{if } n_d > 0 \text{ and } T > 0 \\ \alpha_{t-1} - a_3 e^{\left(a_2\sqrt{n_d}\right)} & \text{if } n_d > 0 \text{ and } T < 0 \\ \alpha_{t-1} + a_4 P_s & \text{if } n_d = 0 \end{cases} \tag{3.8}$$

where α_{t-1} is the albedo at the previous time step, α_t is the albedo at the current time step, n_d is the number of days since the last snow fall, P_s is the measured rate of snow fall, T is temperature and $a_{1:4}$ are constants that must be found through calibration (Hock and Holmgren, 2005). The original parameterization proposed by Hock and Holmgren (2005) included an alteration of the albedo based on a cloudiness factor. It was recommend to us that this correction be removed as outside of Storglaciären it had not been successful (*pers. com., R. Hock,* (2009)).

When this parameterization was applied to North Glacier and South Glacier in some grid cells the snow albedo falls to absurdly low values. To prevent to model from producing such values a lower limit for snow albedo of 0.66 is enforced (Paterson, 1994).

Firn is treated in a similar fashion as snow. When a snow–firn transition occurs, an instantaneous change in albedo of 0.03 is applied to account for the accumulation of debris in firn, after which the firn is treated the same as snow, following Hock and Holmgren (2005). Firn is given a different lower albedo limit than snow of 0.56 (Paterson, 1994). A constant elevation firn-line was assigned based on field observations. No attempt was made to account for firn–ice transitions as the depth of the firn on both glacier is unknown.

Ice is assumed to have a constant albedo in time (e.g. Hock and Holmgren, 2005, Oer-

lemans and Knap, 1998), although observations do not support this assumption. Ice albedo is taken as the mean ice albedo at the AWS location and an elevation-dependent albedo decrease is applied to account for greater debris cover at lower elevations. Rates of ice darkening were crudely estimated using photographs taken during ablation stake surveys. The method of Corripio (2004) was used to estimate albedo from these photographs. This method relates albedo to the bit numbers in digital photography and incident shortwave radiation at the time the photograph was taken. We find a rate of $11\%\,100\mathrm{m}^{-1}$ for South Glacier and $0\%\,100\mathrm{m}^{-1}$ for North Glacier. The measured and simulated albedos for the AWS locations are shown in Figure 3.2.

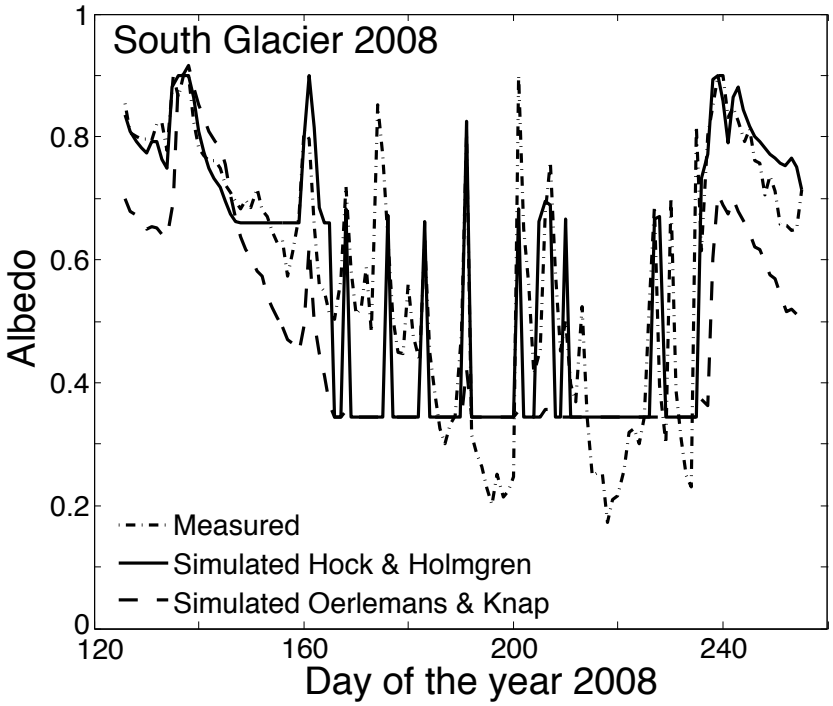

Figure 3.1: Comparison of Hock and Holmgren (2005) and Oerlemans and Knap (1998) parameterizations of albedo for South Glacier in 2008. Notice that the Hock and Holmgren (2005) simulation better matches the measured albedo.

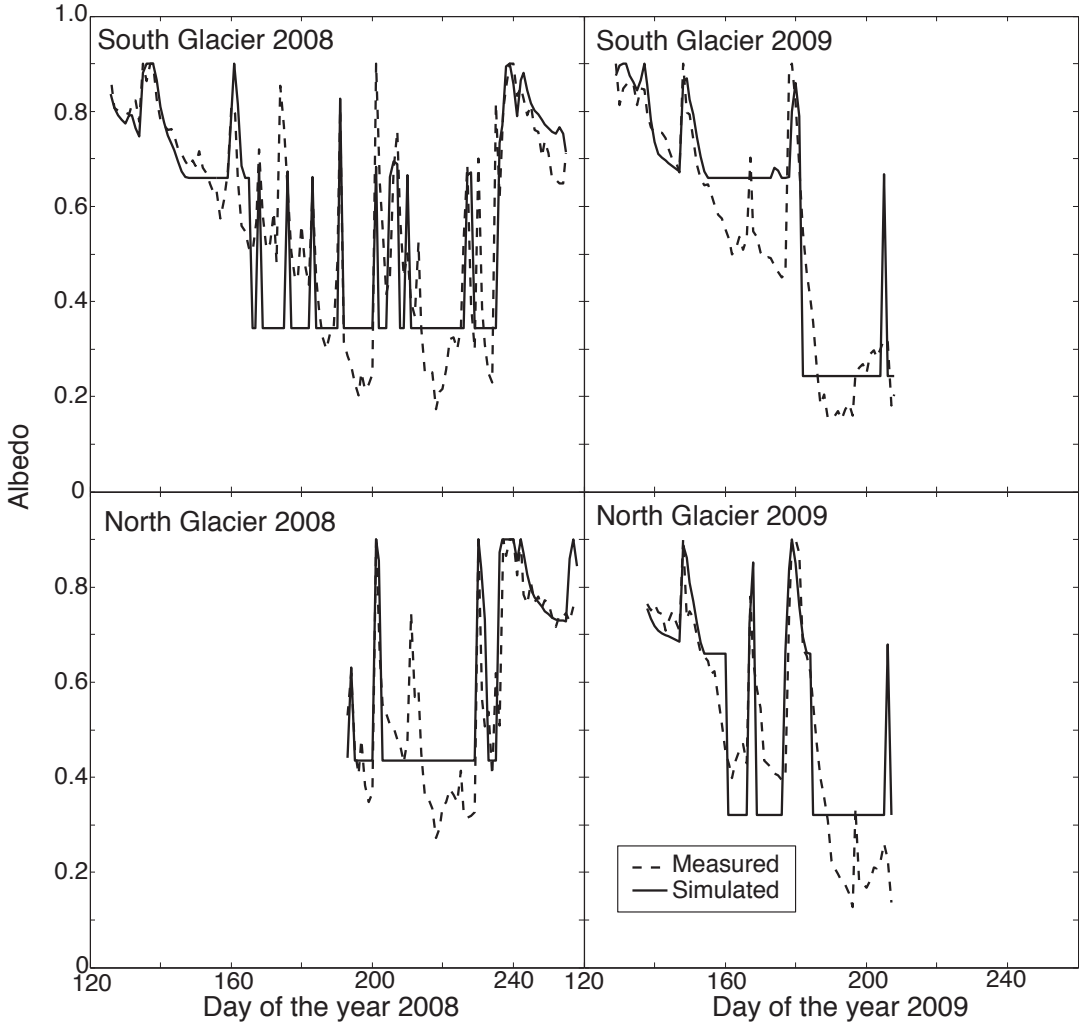

Figure 3.2: Comparison of Hock and Holmgren (2005) parameterization of albedo and simulated albedo for each glacier and year.

3.4 Longwave Radiation and Subsurface Heat Flux

3.4.1 Outgoing Longwave Radiation and Subsurface Heat Flux

Outgoing longwave radiation is calculated from the temperature of the ice or snow surface T_s according to the Stefan-Bolzmann relationship,

$$L_{out} = \varepsilon \sigma T_s^4, \tag{3.9}$$

where ε is emissivity of the surface and $\sigma = 5.67 \times 10^{-8}\,\mathrm{J\,s^{-1}m^{-2}K^{-4}}$ is the Stefan-Boltzmann constant. Following convention in energy-balance modelling the emissivity ε of ice is taken as 1 (e.g. Arnold et al., 1996, Hock and Holmgren, 2005).

The temperature of the surface and the subsurface heat flux are calculated using a simple subsurface scheme. In this scheme the subsurface flux Q_g is taken as the residual of the energy balance when the energy balance is negative. The subsurface flux is forced into a thin subsurface layer such that,

$$\triangle T_s = \frac{Q_g}{\rho_f c_s h} \triangle t, \tag{3.10}$$

where $\triangle t$ is the time-step in seconds, ρ_f is the surface material density, c_s is the specific heat capacity of ice, and h is the thickness of the subsurface layer. Unaltered, this scheme has a tendency to produce absurdly cold surface temperatures during prolonged periods of sub-freezing air temperatures. To solve this problem a second passive layer is added to the scheme. This second layer takes up cold-content if the surface temperature drops below a defined threshold. Then when the surface layer reaches the freezing point the surface is prevented from melting until all of the cold content in the passive layer is balanced by subsurface heat flux, enforcing the conservation of energy. Although physical subsurface schemes have been developed for and used in DEBMs these schemes have large data requirements that are only met for the most well studied glaciers (e.g Reijmer and Hock, 2008).

3.4.2 Incoming Longwave Radiation

Incoming longwave radiation is computed as a residual of the radiative energy balance at the AWS location and is assumed to be representative over the entire glacier, following

Hock and Holmgren (2005). The radiative balance is

$$L_{\text{in}} = Q_N - S_{\text{in}} + S_{\text{ref}} + L_{\text{out}}, \tag{3.11}$$

where Q_N is the measured net radiation and S_{ref} is the reflected shortwave radiation. The outgoing longwave radiation for this calculation is computed from surface temperatures produced by the more sophisticated subsurface scheme used in a point energy balance model developed by Wheler (2009), to increase the accuracy of the calculation.

Incoming longwave radiation emitted from surrounding terrain was calculated following Anslow et al. (2008),

$$L_{\text{terrain}} = \varepsilon_{\text{r}} \sigma T_{\text{a}}^4, \tag{3.12}$$

$$L_{\text{in}} = L_{\text{sky}}(V_f) + L_{\text{terrain}}(1 - V_f), \tag{3.13}$$

where L_{terrain} is the longwave radiation emitted by surrounding terrain, ε_{r} is the emissivity of surrounding terrain taken as 0.95 (Anslow et al., 2008), T_{a} is air temperature and L_{sky} is the incoming longwave radiation from an unobscured sky. Although this parameterization is an obvious oversimplification, it has been shown to work well, likely because most longwave radiation combines with emissions from the air within 500 m of the valley walls (Greuell and Knap, 1997). L_{sky} must be backed out of Equation 3.13 as the AWS is affected by surrounding topography.

3.5 Turbulent Fluxes Q_{H} and Q_{L}

Sensible and latent heat fluxes are calculated using the bulk aerodynamic approach as in other recent DEBM studies (e.g. Anderson et al., 2010, Brock et al., 2000a, Hock and Holmgren, 2005, Anslow et al., 2008). Despite glacier boundary layers violating some of the assumptions that are used to derive the bulk aerodynamic approach, the method has been shown to work well in glacierized environments (Denby and Greuell, 2000). Sensible heat flux Q_H is calculated using this approach as

$$Q_H = \frac{\rho_a c_p k^2 u_z T_c}{(\ln(z/z_o) - \Psi_M(z/L))(\ln(z/z_{oT}) - \Psi_H(z/L))}, \tag{3.14}$$

where ρ_a is the density of air, c_p is the heat capacity of air, $k = 0.4$ is the von Kármán constant, u_z is wind speed, T_c is the air temperature relative to the freezing point and adjusted

for air pressure, z is the height at which the measurements are made above the ground, z_o is the aerodynamic roughness length of the surface, z_{oT} is the roughness length for temperature, L is the Obukhov length, and $\Psi_{M,H}$ are stability constants. Latent heat flux Q_L is similarly calculated as:

$$Q_L = \frac{\rho_a L_v k^2 u_z \left(\frac{0.622}{p}\right)(e_z - e_s)/p_c}{(\ln(z/z_o) - \Psi_M(z/L))(\ln(z/z_{oe} - \Psi_H(z/L))}, \tag{3.15}$$

where e_z is the vapour pressure at height z, e_s is vapour pressure at the surface, L_v is the latent heat of vaporization (as in Anslow et al. (2008)), p_c is the atmospheric pressure and z_{oe} is the roughness length for humidity. The equation for L depends on Q_H such that an iterative loop is necessary to calculate these energy fluxes (Hock and Holmgren, 2005),

$$L = \frac{\rho_a c_p u_*^3 T_\mathrm{a}}{k g Q_\mathrm{H}}, \tag{3.16}$$

$$u_* = \frac{k u_z}{\ln(\frac{z}{z_{0T}}) - \Psi_M}, \tag{3.17}$$

where u_* is the friction velocity, T_a is air temperature in kelvin and $g = 9.81\,\mathrm{m\,s^{-2}}$ is the gravitational constant at Earth's surface.

The stability constants $\Psi_{M,H}$ are calculated for stable conditions using the non-linear stability functions of Beljaars and Holtslag (1991), following Hock and Holmgren (2005) and Forrer and Rotach (1997). These stability functions are

$$-\Psi_M = \frac{c_1 z}{L} + c_2\left(\frac{z}{L} - \frac{c_3}{c_4}\right)\exp\left(-c_4\frac{z}{L}\right) + \frac{c_2 c_3}{c_4}, \tag{3.18}$$

$$-\Psi_H = \left(1 + \frac{2c_1 z}{3L}\right)^{\frac{3}{2}} + c_2\left(\frac{z}{L} - \frac{c_3}{c_4}\right)\exp\left(-c_4\frac{z}{L}\right) + \frac{c_2 c_3}{c_4} - 1, \tag{3.19}$$

where $c_{1:4}$ are empirical constants taken from Beljaars and Holtslag (1991). For the infrequent unstable conditions the commonly used Businger-Dyer expressions are used (Paulson, 1970).

3.5.1 Aerodynamic Roughness Length z_o

The aerodynamic roughness length (z_o) used in the bulk aerodynamic approach is defined as the distance above the surface at which wind speed reaches zero (Brock et al., 2006). Dealing with this parameter has bedeviled previous distributed energy balance melt modellers

and is often used as a tuning constant (e.g Hock and Holmgren, 2005). The constantly changing glacier surface results in changing values of z_o and interferes with attempts to measure z_o accurately; as the methods of measuring wind profiles are very sensitive to the height of the instrumentation above the glacier surface (Brock et al., 2006). Brock et al. (2006) examined this problem in detail finding that the microtopographic approach to measuring aerodynamic roughness length as a function of surface roughness fell entirely within the error bound of the wind profile method. In addition to examining the techniques used to measure z_o, Brock et al. (2006) made the first attempts at creating a time-evolving parameterization for the roughness length of snow. The parameterization relates the natural logarithm of snow roughness length to the logarithm of the sum of positive degree days since the last snowfall event:

$$\ln(z_o) = b_1 \left(\arctan \left[\frac{(P_{\mathrm{dd}} - b_2)}{b_3} \right] \right) - b_4, \tag{3.20}$$

where P_{dd} is the base 10 logarithm of the sum of daily maximum temperatures since the last snow fall event and $b_{1:4}$ are empirical constants. I calculate the empirical constants using a least-squares fit between the parameterization and snow roughness lengths measured during the 2009 field campaign. Insufficient data existed to produce independent fits for both North Glacier and South Glacier so the data sets were combined to provide one set of parameters for the entire study area (Figure 3.3). The 2009 parameter values were used for the 2008 simulations, as no attempt was made to measure aerodynamic roughness length in 2008. Brock et al. (2006) failed to find a time-evolving roughness length parameterization for ice. I therefore use the mean value of the measured roughness of ice for each glacier. Firn is treated simply as very old snow. The roughness lengths for temperature z_{oT} and water vapour z_{oe} were taken as two orders of magnitude smaller than the roughness length z_o, following Hock and Holmgren (2005).

3.6 Snowfall Events

Snowfall events are recorded at the AWS by the USDG. These events are extrapolated to the rest of the glacier using an empirical precipitation lapse rate, a temperature threshold

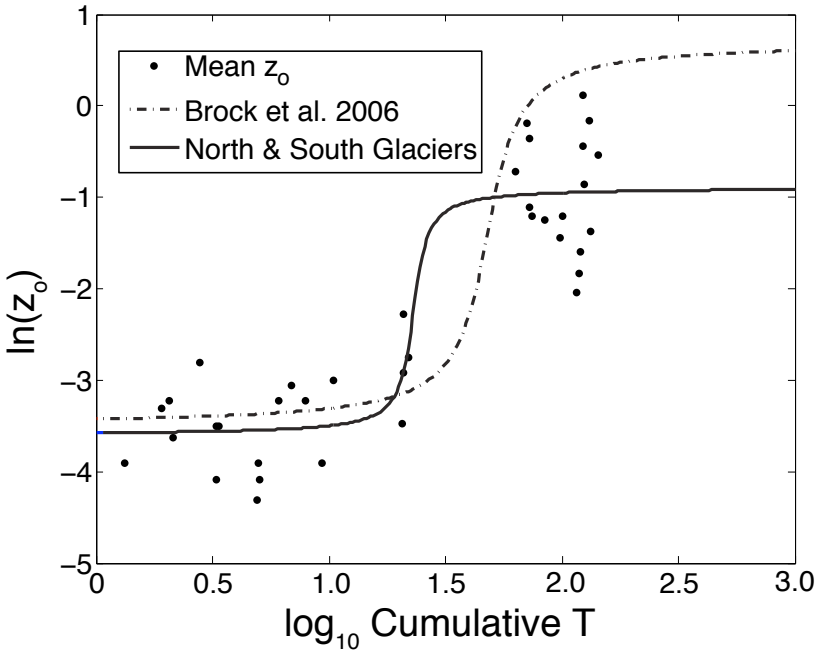

Figure 3.3: Measured and modelled snow aerodynamic roughness lengths (Brock et al., 2006). Solid line is the parameterization using values determined by least-squares regression in this study. Dashed line is the original parameterization of Brock et al. (2006).

and the rainfall records from the AWS. The snowfall is modified using the precipitation lapse rate to the elevation of each grid point. The temperature lapse rate is used to find the temperature at the grid point, and if the temperature is above the threshold of 1 °C then the snow is assumed to melt before reaching the ground. Similarly rainfall is extrapolated to each grid cell using the precipitation lapse rate and is converted to snow if the local temperature is below the melt/freeze threshold. The record of rainfall is manually adjusted to remove spurious points caused by snow accumulation and melting in the rain bucket.

Chapter 4

Model Validation

4.1 Introduction

Distributed energy balance melt model (DEBM) simulations were carried out by driving the model for each glacier and year with locally measured meteorological variables, using local initial snow-depth, and using locally derived model parameters. These simulations are referred to as the "control runs". Data required for the control runs were collected from the two Donjek Range study glaciers in the summers of 2008 and 2009, creating four data sets of meteorological variables and parameter values: the North Glacier 2008 data set (N08), the North Glacier 2009 data set (N09), the South Glacier 2008 data set (S08), and the South Glacier 2009 data set (S09). For full details of how each parameter is derived see *Modelling Methods*. For details of how meteorological variable were collected see *Field Measurements and Data Processing*.

The purpose of the control runs is to (1) assess the skill of the model by comparing the results of these simulations to validation data and (2) to create reference energy balance, and ablation estimates from which to assess deviations created by the model sensitivity tests and the model transferability experiments. Error relative to the validation data is quantified using two statistics, Mean Percentage Error (MPE), a measure of model bias,

$$MPE = \frac{\sum_{i=1}^{n} (M_{\mathrm{s}i} - M_{\mathrm{m}i})}{n\overline{M}_{\mathrm{m}}} \times 100\,\%, \tag{4.1}$$

and Root Mean Square Error (RMSE), a measure model precision,

$$RMSE_p = \frac{\sqrt{\sum_{i=1}^{n} \left(M_{\mathrm{s}i} - M_{\mathrm{m}i}\right)^2}}{\sqrt{n}\overline{M_{\mathrm{m}}}} \times 100\,\%, \tag{4.2}$$

$$RMSE_a = \frac{\sqrt{\sum_{i=1}^{n} \left(M_{\mathrm{s}i} - M_{\mathrm{m}i}\right)^2}}{\sqrt{n}}, \tag{4.3}$$

where $M_{\mathrm{s}i}$ is the simulated melt in grid point i, $M_{\mathrm{m}i}$ is the measured melt at the stake located in the grid point i, $\overline{M_{\mathrm{m}}}$ is the mean of the measured melt and n is the number of ablation stakes surveyed. For assessing model validity I found it useful to compute RMSE both as a relative error $\mathrm{RMSE_p}$ expressed in percent (%) and as an absolute error $\mathrm{RMSE_a}$ expresses in water equivalent meters (w.e. m).

4.2 Model skill

There are two sets of validation data used to assess model skill: data from an array of ablation stakes deployed on each glacier which yield total summer ablation at various locations on the glaciers, and data from the Ultra Sonic Depth Gauges (USDG) which yields daily ablation at the location of the Automatic Weather Stations (AWS) deployed on each glacier. (See *Field Measurements and Data Processing* for details on how the validation data were collected and processed.) The two data sets used to assess model skill were not used to tune the model, therefore the validation data are independent of the model parameters.

A problem arises in the comparison of simulated ablation at the AWS locations to the ablation measured by the USDG, in that the regression used to estimate initial snow-depth for the distributed model tends to greatly overestimate the amount of snow at the AWS locations. This causes the simulation to underestimate ablation compared to the USDG record on both South Glacier and North Glacier. To more realistically assess model performance, special simulations were carried out for the AWS locations using locally measured snow-depth. The comparison between the USDG record and all following simulations (including those in *Transferability Experiments*) is therefore not a comparison to the distributed model, but a point energy balance model identical to the DEBM, except for the use of a locally measured initial snow-depth.

The results of the comparison between ablation-stake-derived estimates of ablation and simulated ablation for both glaciers for both years are shown in Figure 4.1. Errors, expressed in MPE and RMSE, are annotated on the figure as well as displayed in Table 4.1. The comparisons between the USDG records and modelled ablation are shown in Figure 4.2.

Table 4.1: Comparison of simulated and measured ablation at stake locations for the control runs.

	MPE (%)	$RMSE_p$ (%)	$RMSE_a$ (m)
S08 control	−11	23	0.29
S09 control	−10	14	0.14
N08 control	18	30	0.11
N09 control	−11	15	0.20

These results show that in general the model can reproduce measured ablation with reasonable accuracy, but not to within the measurement uncertainty of the ablation stakes (Figure 4.1). The MPEs with respect to the stakes calculated for three of the data sets (South Glacier 2008, South Glacier 2009 and North Glacier 2009) are similar and range from -10 to -11 %, indicating that the model underestimates ablation. This can also be seen in the USDG comparison (Figure 4.2), where for those three data sets the model closely follows the USDG record after the snow–ice transition then drifts below the measured ablation toward the end of the melt season. The exception is the North Glacier 2008 data set where the model overestimates ablation, having an MPE of 18 %. This overestimation also applies to the USDG record where the model departs from the record soon after the USDG begins working on the 11^{th} July 2008 (day 193), converging again for several days before the simulated ablation drifts above the USDG record after the late summer snowfall.

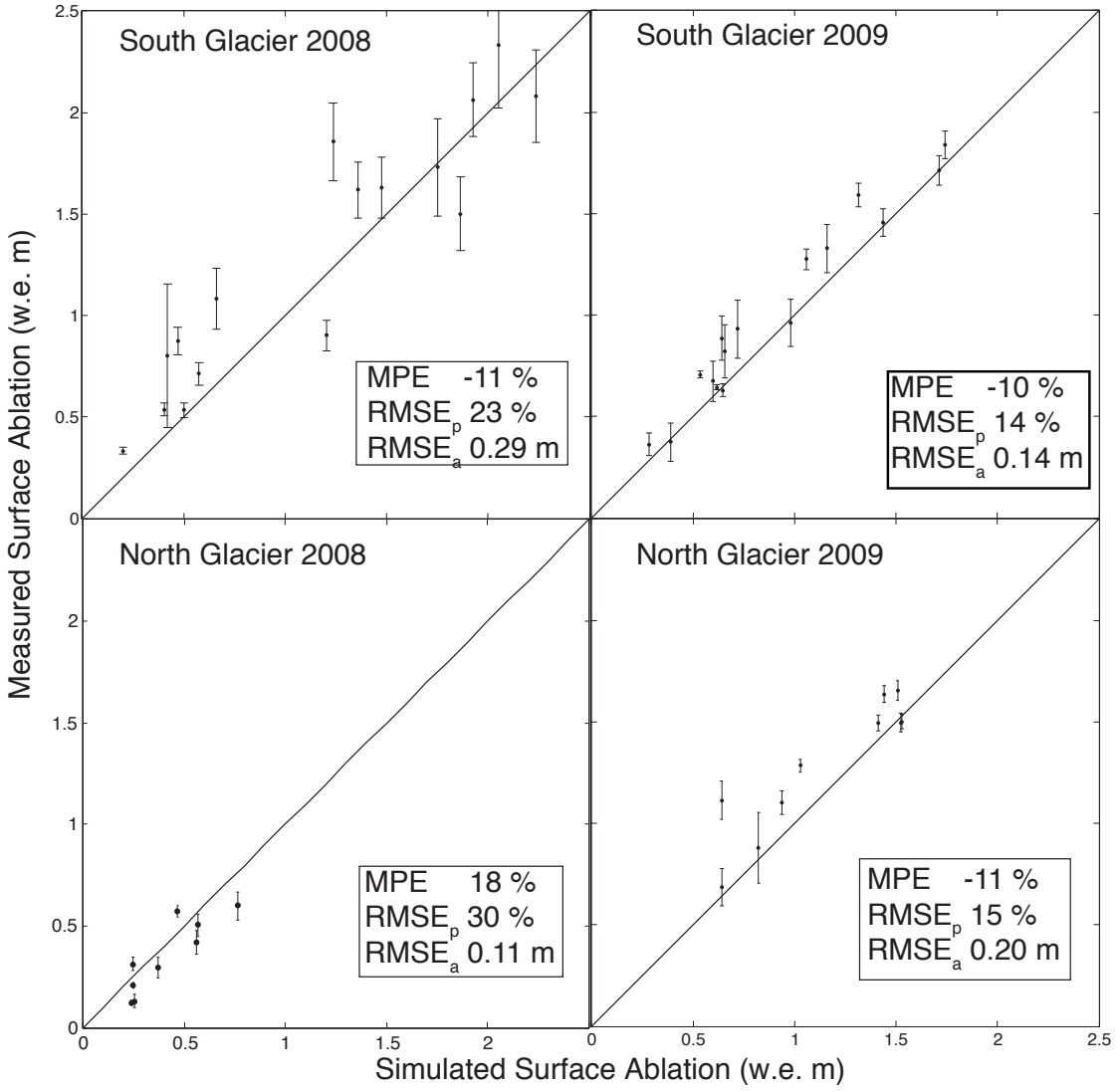

Figure 4.1: Comparison of simulated and measured ablation at stake locations for the control runs. Notice that in three of the simulations the model underestimates ablation; for North Glacier 2008 the model overestimates ablation.

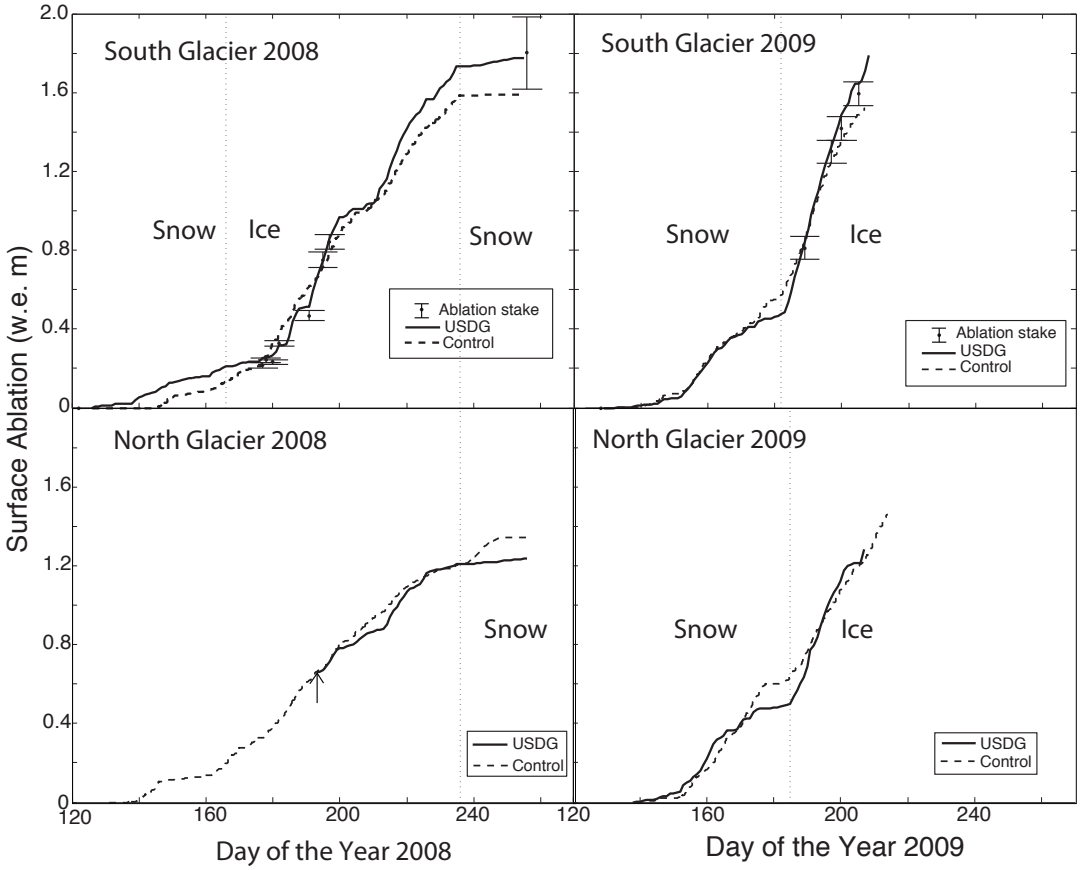

Figure 4.2: Comparison of simulated and measured ablation at USDG location. For South Glacier ablation stake measurements from near the AWS are also shown. Dotted vertical lines delineate snow–ice transitions. Arrow indicates when the USDG on North Glacier began functioning in 2008.

This overestimation for North Glacier 2008 may be a result of sparse validation data. The validation data for this data set is more spatially and temporally limited than for the other data sets. Only eight of the ablation stakes on North Glacier were measured both in the spring and the autumn of 2008. In addition the USDG did not start recording surface lowering until the 11th of July 2008.

The RMSE is largest for South Glacier in 2008 in absolute terms, and largest for North Glacier 2008 in relative terms. Relative RMSE is smaller in 2009 than in 2008. This may be a result of the different meteorological characteristics of the two summers: colder and snowier in 2008 verses warmer and drier in 2009, or could be a result of the shorter simulation period in 2009, ending in late July and early August as opposed to in September for the 2008 simulations.

4.3 Model output

Four model outputs are used to compare the control runs to the transferability experiments (see *Transferability Experiments*). These outputs are: spatially distributed model ablation (Figure 4.3), cumulative melt at the AWS location (Figure 4.2), mass balance components (Table 4.2) and energy balance components (Table 4.3). All output is computed for the period of overlap of the North Glacier and South Glacier data sets for each year. The 2008 overlap is from the 10th of May – 10th of September (day 131–254). The overlap for 2009 is from the 19th of May – 26th of July (day 139–207).

These model outputs reveal several important features of the study glaciers. Ablation on both glaciers is dominated by net radiation, and the turbulent fluxes are more important on North Glacier than South Glacier. 2008 was a lower melt year than 2009. Ablation in 2009 had already exceeded that in 2008 by the end of July with over a month left in the typical ablation season. Mass balance was negative for both glaciers (unless a large amount of snow fell on the glaciers in August 2009), although North Glacier 2008 was close to balance in 2008.

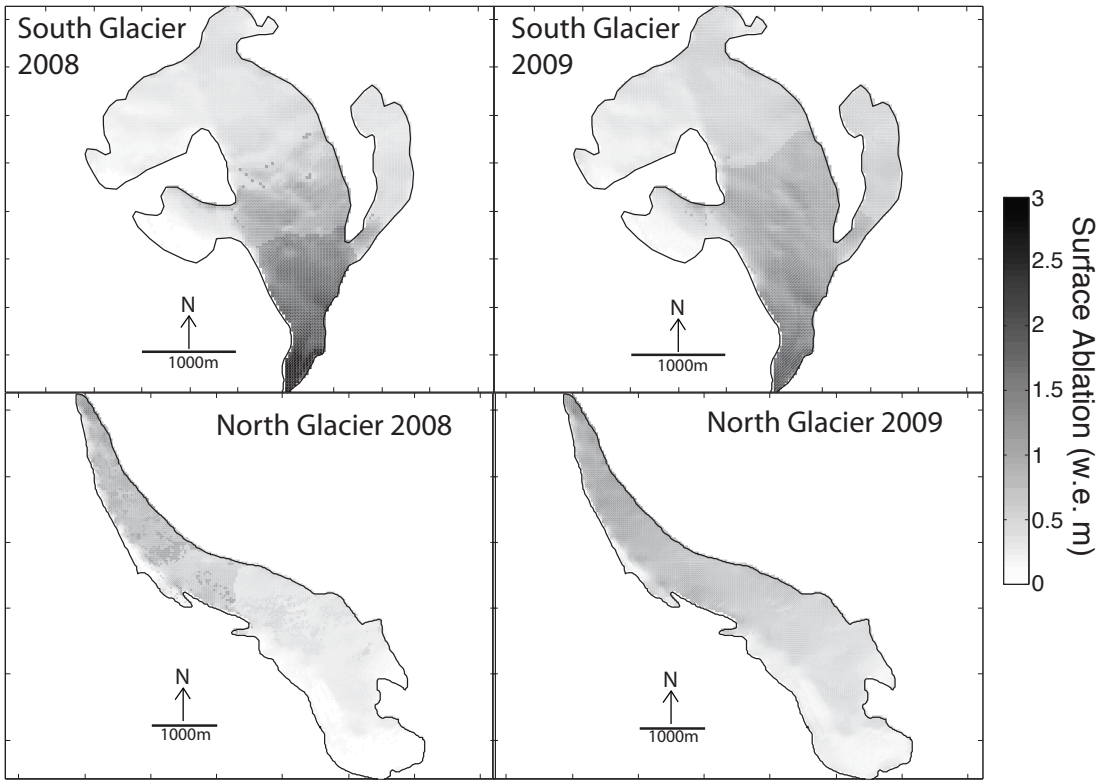

Figure 4.3: Spatially distributed surface ablation computed in the control runs.

Table 4.2: Spatially averaged mass balance components (w.e. m) as estimated by the control runs: C_{w} is winter surface accumulation, C_{s} is summer surface accumulation, A_{s} is summer surface ablation and B_{n} is surface net balance. Note that for 2008 the mass balance is the yearly mass balance. For 2009 the mass balance is the mass balance at the time the South Glacier albedometer was taken down on July 26$^{\mathrm{th}}$ 2009 mid-way though the ablation season.

Simulation	C_w	C_s	A_s	B_n
S08 control	0.33	0.29	−0.79	−0.18
S09 control	0.53	0.05	−0.81	−0.23
N08 control	0.23	0.17	−0.46	−0.07
N09 control	0.38	0.07	−0.70	−0.25

Table 4.3: Spatially averaged energy balance components (W m^{-2}).

Simulation	S_{net}	L_{net}	Q_{H}	Q_{L}	Q_{g}	Q_{M}
S08 control	80.0	−59.3	4.9	−1.4	−0.3	24.9
S09 control	95.1	−57.8	10.8	−1.8	−0.3	46.1
N08 control	61.6	−52.9	6.6	−1.1	0.5	14.6
N09 control	84.4	−54.4	13.0	−3.5	0.3	39.7

4.3.1 Comparison to empirical models

A general comparison can be made between the errors found using the DEBM for the summers of 2008 and 2009 and the errors found using temperature-index models for these glaciers in the summers of 2006 and 2007 in Wheler (2009). Using classical temperature-index models Wheler (2009) calculated RMSEs ranging from 15–25 %, and using an enhanced temperature-index model, calculated RMSEs of 14–23 %. The RMSE range found for this study 14–30 % confirm that physically based energy balance melt models do not simulate melt more accurately than simple empirical models (e.g. Hock, 2005). Nevertheless that physical models can reproduce melt to the same precision as empirical models without specifically using ablation data to tune the models is encouraging.

Chapter 5

Sensitivity Testing

5.1 Model sensitivity to parameter perturbation

The distributed energy balance melt model (DEBM) created for this study contains 23 parameters which must either be derived from field data or taken from literature. These parameters describe unique local features of the study glaciers that may change in space or time. As the parameters are derived from field data or the literature each is associated with a poorly constrained finite error which will effect the skill of the DEBM; it is therefore important to assess the model sensitivity to each parameter.

Model sensitivity to each parameter was evaluated by varying the parameter value through a range of plausible values, while holding all of the other model parameters constant. What constitutes a plausible range of values is somewhat subjective and therefore the results of this analysis must be interpreted with caution. Parameters with clear physical meaning have well defined ranges of plausible values, for example the parameter α_{ter}, the albedo of surrounding terrain, can only take on values between the darkest albedo of rock and the highest albedo of snow. Other parameters do not have a clear physical meaning, such as the a_2 parameter in the Hock and Holmgren (2005) parameterization of snow albedo evolution. This parameter controls the rate of decline in snow albedo since the last snow fall and represents a collection of distinct physical processes. The plausible range in this parameter is therefore poorly defined and consequently assumed to be large.

Model sensitivity is quantified using two statistics, Mean Percentage Error (MPE)

$$MPE = \frac{\sum_{i=1}^{n} (M_{si} - M_{mi})}{n\overline{M_m}} \times 100\,\%, \tag{5.1}$$

and Root Mean Squared Error (RMSE)

$$RMSE = \frac{\sqrt{\sum_{i=1}^{n} (M_{si} - M_{mi})^2}}{\sqrt{n}\overline{M_m}} \times 100\,\%, \tag{5.2}$$

where M_{si} is the simulated melt in grid point i, M_{mi} is the measured melt at the stake located in the grid point i, $\overline{M_m}$ is the mean of the measured melt and n is the number of ablation stakes surveyed. MPE is a measure of model bias: an unbiased model will have an MPE of zero, but might have large scatter in model output. RMSE is a good measure of model precision and is considered the stronger of the two statistics. All errors are here presented as percentages. Model sensitivity is expressed as a range in MPE or RMSE. That is, the difference between the highest and lowest error generated by the plausible range for each parameter. Each parameter rage was broken into equal increments of one tenth of the range for computation. The results of these test are shown in the tables labeled "coarse". If one tenth increments were too large to resolve the optimum parameter value to sufficient precision a smaller range bounding the closest to zero MPE and minimum RMSE values was used for a second calculation. These smaller ranges were also broken into one tenth increments for computation. The results of these finer increment tests are displayed in the tables labeled "fine".

The parameters are here grouped into four categories for the purposes of clarity. The categories are: "albedo parameters" ,the parameters that control the Hock and Holmgren (2005) albedo evolution parameterization; "roughness parameters", the parameters that control the Brock et al. (2006) parameterization of aerodynamic roughness length evolution; "lapse rates", the parameters involved in temperature and precipitation elevation lapse rates and "Miscellaneous Parameters", all of the other parameters needed to run the model.

5.1.1 Miscellaneous parameters

There are eight Miscellaneous parameters used in the model, four of which – density of ice, density of fresh snow, density of the initial snow pack and model tolerance – have essentially no effect on the model within their plausible ranges and will not be discussed further.

Table 5.1: Parameters used in the DEBM, their units, symbols and meaning

Parameter	Units	Meaning
Miscellaneous parameters		
α_{ter}		Albedo of surrounding terrain
ε_{ter}		Emissivity of surrounding terrain
T_{sub}	°C	Minimum limit of subsurface temperature
h	m	Thickness of subsurface model
Albedo Parameters		
α_{o}		Initial albedo of snow
E_{f}	m	Firn line elevation
$\frac{d\alpha_{\text{i}}}{dZ}$	$100\,\text{m}^{-1}$	Change ice albedo with elevation
a_1	$\ln(^\circ\text{C})^{-1}$	Albedo temperature rate constant
a_2	$\text{day}^{-\frac{1}{2}}$	Albedo time constant
a_3		Albedo subfreezing darkening constant
a_4	$\text{hr}\,\text{m}^{-1}$	Albedo snowfall rate constant
α_{i}		Albedo of ice
$\alpha_{\text{s lim}}$		Lower limit of snow albedo
$\alpha_{\text{f lim}}$		Lower limit of firn albedo
$\alpha_{\text{s to f}}$		Albedo snow–firn transition
$\alpha_{\text{i lim}}$		Lower limit of ice albedo
Roughness Parameters		
Z_{thr}	m	Fresh snow depth threshold
b_1	mm	Roughness scaling constant
b_2	°C	Temperature translation
b_3	°C	Temperature scaling
b_4	mm	Roughness translation
$z_{o\text{i}}$	mm	Roughness length of ice
Lapse rates		
Γ_{T}	$\text{K}\,\text{km}^{-1}$	Temperature lapse rate
Γ_{p}	$\text{mm}\,\text{km}^{-1}$	Precipitation lapse rate

The remaining parameters are the albedo of the surrounding terrain (α_{ter}), the emissivity of the surrounding terrain (ε_{ter}, the lowest allowable temperature in the subsurface model (T_{sub}), and the thickness of the subsurface model (h) (Tables 5.2–5.5, Figure 5.2). The range of error created by perturbing these parameters is moderate, 1-10% RMSE, for three of the four simulations (South Glacier 2008, 2009 and North Glacier 2009) but higher for North Glacier 2008. This pattern of greater error associated with the simulation of North Glacier 2008 is also present for the other categories of parameters. North Glacier 2008 is unique among the data sets in that only eight ablation stakes were surveyed during both expeditions to North Glacier in 2008. These measurements are heavily biased toward the accumulation zone of the glacier, where melt is relatively small compared to that in the ablation zone and therefore perturbations to the model that create a small absolute error will produce a larger relative error simply because the mean melt is small.

The most concerning error range in the miscellaneous parameters is that associated with the thickness of the subsurface model (h), as this parameter was chosen to minimize the number of iterations required for the model to converge. Examination of Figure 5.1, shows that the value of this parameter has little effect on the model RMSE until a threshold above 0.1 m is reached. This indicates that there are a range of equally good values for h and that the choice of 0.1 m to minimized model iterations is justified.

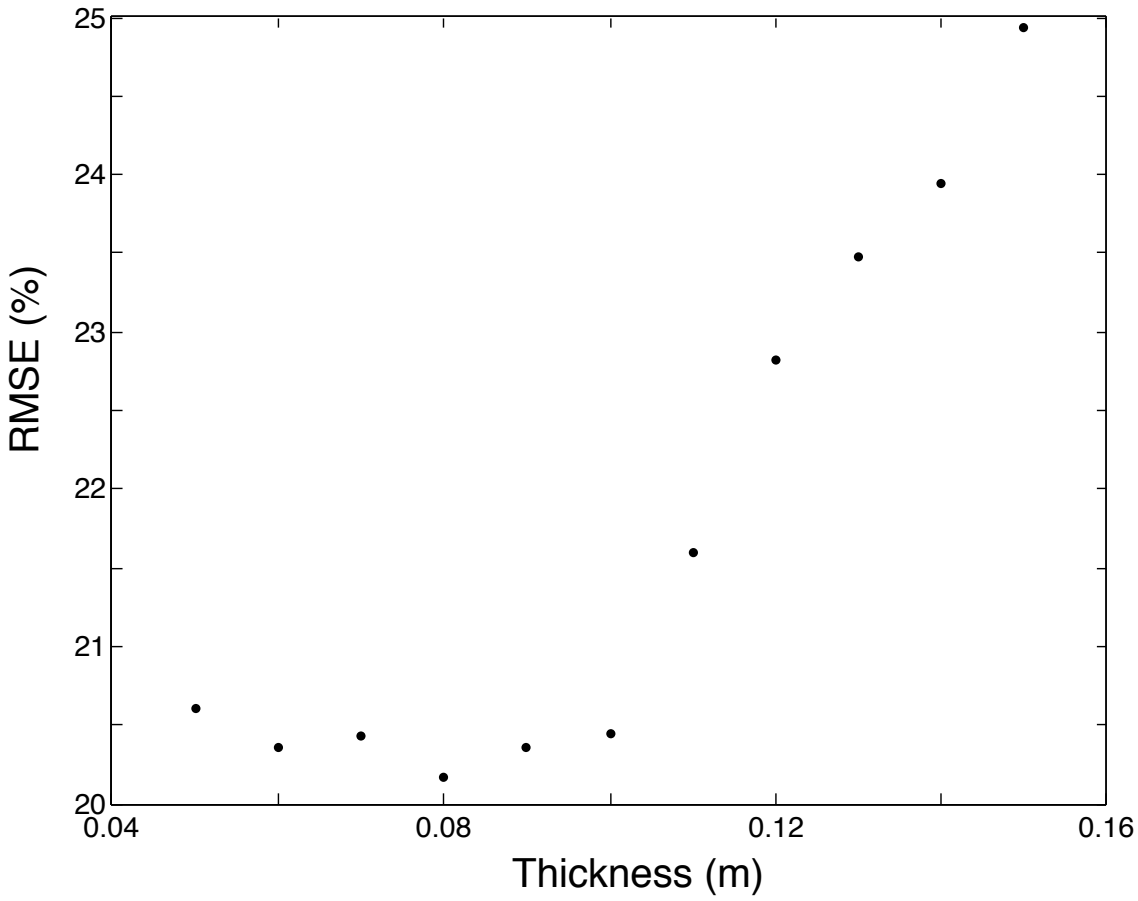

Figure 5.1: RMSE vs. values of parameter h, the thickness of the subsurface model. Note that the value of h makes little difference to model skill until a threshold greater than 0.1 m is reached.

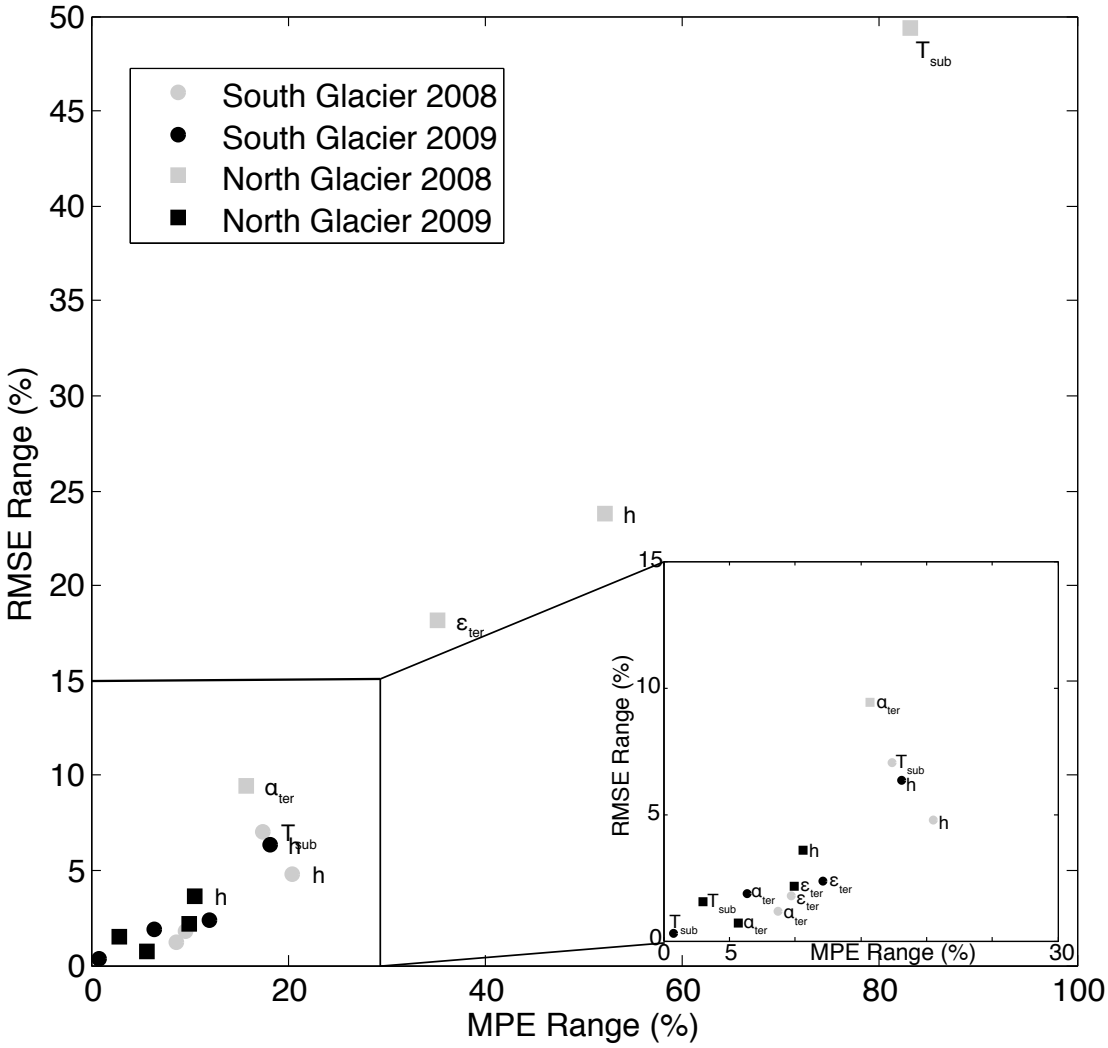

Figure 5.2: RMSE vs. MPE ranges for each miscellaneous parameter and data set.

Table 5.2: RMSE ranges and values for sensitivity study of miscellaneous parameters, coarse increments.

Variable	Control Value	Value Range	Min RMSE	Optimum Value	Range RMSE
S08					
α_{ter}	0.21	0 – 0.5	20.3 %	0.35	1.2 %
ε_{ter}	0.95	0.91 – 1	20.3 %	0.98	1.8 %
T_{sub}	−30 °C	−50 to −20 °C	20.4 %	−38 °C	7.1 %
h	0.1 m	0.05 – 0.15 m	20.2 %	0.8 m	4.8 %
S09					
α_{ter}	0.21	0.1 – 0.5	14.3 %	0.18	1.9 %
ε_{ter}	0.95	0.9 – 1	14.3 %	0.95	2.4 %
T_{sub}	−30 °C	−50 to −30 °C	14.1 %	−36 °C	0.3 %
h	0.1 m	0.05 – 0.15 m	14.3 %	0.1 m	6.3 %
N08					
α_{ter}	0.21	0 – 0.5	27.3 %	0.30	9.4 %
ε_{ter}	0.95	0.9 – 1	27.3 %	0.95	18.1 %
T_{sub}	−30 °C	−50 to −20 °C	30.4 %	−32 °C	49.4 %
h	0.1 m	0.05 – 0.15 m	27.3 %	0.1 m	23.8 %
N09					
α_{ter}	0.21	0– 0.5	9.9 %	0.25	0.7 %
ε_{ter}	0.95	0.9 – 1	9.9 %	0.95	2.2 %
T_{sub}	−30 °C	−50 to −20 °C	10.3 %	−29 °C	1.6 %
h	0.1 m	0.05 – 0.15 m	9.9 %	0.1 m	3.6 %

Table 5.3: RMSE ranges and values for sensitivity study of miscellaneous parameters, fine increments.

Variable	Control Value	Value Range	Min RMSE	Optimum Value	Range RMSE
S08					
α_{ter}	0.21	0.20 – 0.40	20.4 %	0.26	0.3 %
T_{sub}	$-30\,^{\circ}$C	-46 to $-36\,^{\circ}$C	20.1 %	$-37\,^{\circ}$C	1.3 %
S09					
α_{ter}	0.21	0.1 – 0.3	14.3 %	0.12	0.3 %
N08					
α_{ter}	0.21	0.15 – 0.35	27.3 %	0.21	9.5 %
T_{sub}	$-30\,^{\circ}$C	-35 to $-25\,^{\circ}$C	27.3 %	$-30\,^{\circ}$C	52.5 %
N09					
α_{ter}	0.21	0.15 – 0.35	9.9 %	0.25	0.2 %

Table 5.4: MPE ranges and values for sensitivity study of miscellaneous parameters, coarse increments.

Variable	Control Value	Value Range	Min MPE	Optimum Value	Range MPE
S08					
α_{ter}	0.21	0 – 0.50	−0.4 %	0.45	8.7 %
ε_{ter}	0.95	0.91 – 1	−0.2 %	0.99	9.7 %
T_{sub}	−30 °C	−50 to −20 °C	−1.1 %	−44 °C	17.4 %
h	0.1 m	0.05 – 0.15 m	−1.1 %	0.08 m	20.5 %
S09					
α_{ter}	0.21	0.1 – 0.5	−0.1 %	0.46	6.4 %
ε_{ter}	0.95	0.9 – 1	0.3 %	0.98	12.1 %
T_{sub}	−30 °C	−50 to −30 °C	−3.1 %	−50 °C	0.8 %
h	0.1 m	0.05 – 0.15 m	0.6 %	0.08 m	18.1 %
N08					
α_{ter}	0.21	0 – 0.50	0.1 %	0.15	15.7 %
ε_{ter}	0.95	0.9 – 1	−0.7 %	0.94	35.1 %
T_{sub}	−30 °C	−50 to −20 °C	−4.3 %	−29 °C	83.0 %
h	0.1 m	0.05 – 0.15 m	0.2 %	0.09 m	52.1 %
N09					
α_{ter}	0.21	0 – 0.5	0.3 %	0.40	5.7 %
ε_{ter}	0.95	0.9 – 1	0.1 %	0.97	9.9 %
T_{sub}	−30 °C	−50 to −20 °C	−1.2 %	−47 °C	3.0 %
h	0.1 m	0.05 – 0.15 m	−0.1 %	0.08 m	10.6 %

Table 5.5: MPE ranges and values for sensitivity study of miscellaneous parameters, fine increments.

Variable	Control Value	Value Range	Min MPE	Optimum Value	Range MPE
S08					
α_{ter}	0.21	0.20 – 0.40	−1.3 %	0.40	3.2 %
T_{sub}	−30 °C	−46 to −36 °C	−1.1 %	−44 °C	5.1 %
S09					
α_{ter}	0.21	0.10 – 0.30	−2.4 %	0.30	3.0 %
N08					
α_{ter}	0.21	0.15 – 0.35	0.1 %	0.15	6.7 %
T_{sub}	−30 °C	−35 to −25	2.1 %	−30 °C	51.3 %
N09					
α_{ter}	0.21	0.15 – 0.35	−1.2 %	0.35	1.6 %

5.1.2 Albedo parameters

The Hock and Holmgren (2005) parameterization used to simulated albedo in the DEBM contains twelve parameters. Eight of these parameters have clear physical meaning: the initial albedo of snow (α_o), the firn line elevation (E_f), the rate of increase in ice albedo with increased elevation ($\frac{d\alpha_\mathrm{i}}{dZ}$), the albedo of ice ($\alpha_\mathrm{i}$), the lower limit of snow albedo ($\alpha_{\mathrm{s\,lim}}$), the lower limit of firn albedo ($\alpha_{\mathrm{f\,lim}}$), the instantaneous decrease in albedo that accompanies a snow-firn transition ($\alpha_{\mathrm{s\,to\,f}}$) and the lower limit of ice albedo ($\alpha_{\mathrm{i\,lim}}$). Four of the parameters, $a_{1:4}$, are rate controlling constants that together emulate many complex physical processes and therefore do not have a clear physical interpretation.

Four of the albedo parameters, a_1, a_2, $\alpha_{\mathrm{s\,lim}}$ and α_i, consistently create large error ranges when perturbed from their control value (Tables 5.6–5.11, Figure 5.3). This indicates that the values of these four parameters largely control the skill of the DEBM. The optimum values of these four parameters are close to the values obtained by calibrating the albedo model independently. This demonstrates that these parameters are transferable in space over the scale of the glacier basin.

The other albedo parameters have smaller error ranges, but these ranges tend to be larger than those for the other parameter types. The albedo parameterization therefore dominates the sensitivity of the DEBM.

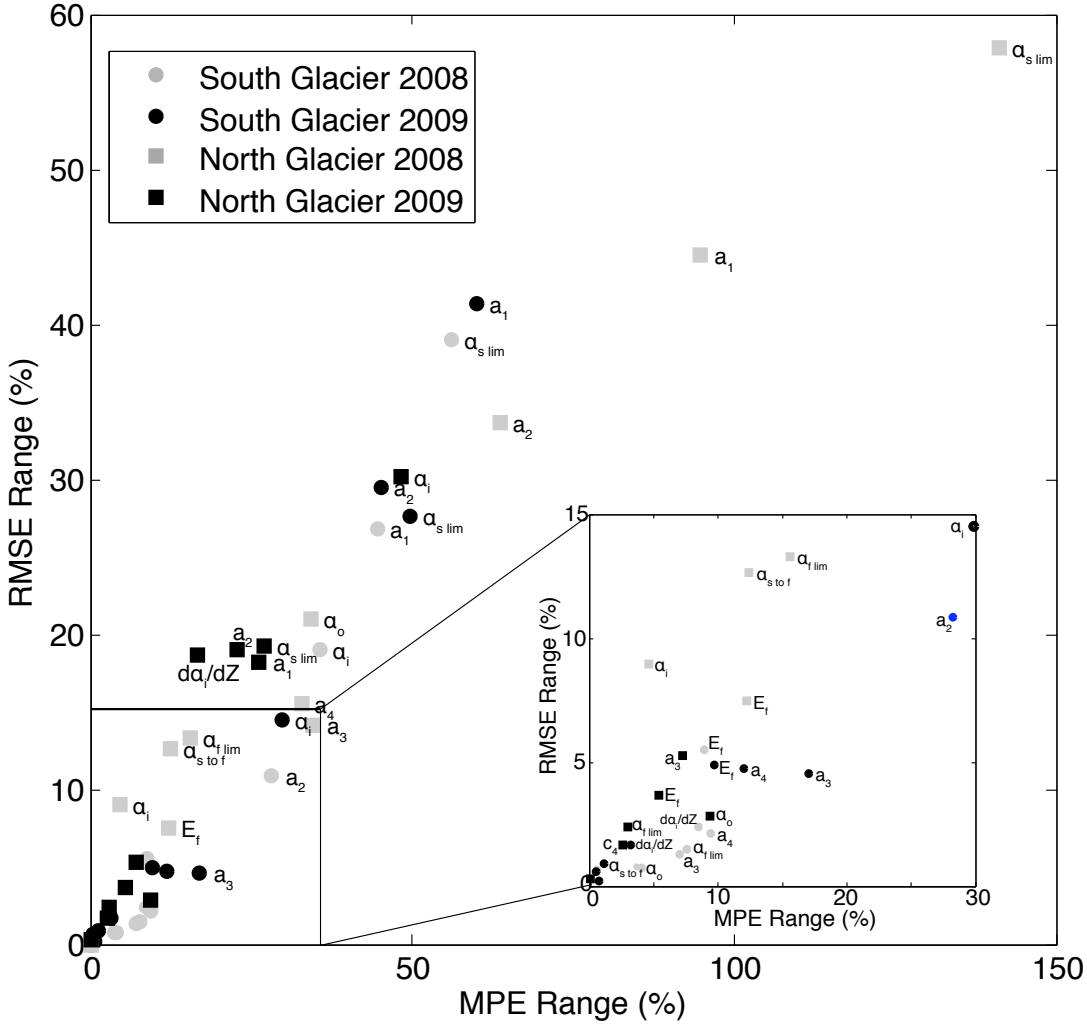

Figure 5.3: Albedo parameters displayed by their sensitivity ranges in MPE vs. RMSE.

Table 5.6: RMSE ranges and values for sensitivity study of albedo parameters, coarse increments, South Glacier.

Variable	Control Value	Value Range	Min RMSE	Optimum Value	Range RMSE
S08					
α_o	0.85	0.63 – 0.9	20.2 %	0.72	0.7 %
E_f	2450 m	2300 – 2500 m	19.9 %	2460 m	5.5 %
$\frac{d\alpha_i}{dZ}$	$0.15\,\mathrm{hm}^{-1}$	$0 – 0.30\,\mathrm{hm}^{-1}$	19.9 %	$0.12\,\mathrm{hm}^{-1}$	2.4 %
a_1	$0.032\,\ln(^\circ\mathrm{C})^{-1}$	$0.01 – 0.1\,\ln(^\circ\mathrm{C})^{-1}$	20.5 %	$0.030\,\ln(^\circ\mathrm{C})^{-1}$	26.8 %
a_2	$-1.54\,\mathrm{day}^{-\frac{1}{2}}$	-2 to $-1\,\mathrm{day}^{-\frac{1}{2}}$	20.9 %	$-1.5\,\mathrm{day}^{-\frac{1}{2}}$	10.9 %
a_3	0.007	0.005 – 0.015	20.4 %	0.007	1.3 %
a_4	$44\,\mathrm{hr\,m}^{-1}$	$10 – 100\,\mathrm{hr\,m}^{-1}$	19.5 %	$10\,\mathrm{hr\,m}^{-1}$	2.1 %
α_i	0.34	0.1 – 0.55	20.2 %	0.35	19.0 %
$\alpha_{s\,lim}$	0.66	0.55 – 0.75	18.4 %	0.63	39.0 %
$\alpha_{f\,lim}$	0.56	0.45 – 0.65	20.3 %	0.61	1.5 %
$\alpha_{s\,to\,f}$	0.03	0 – 0.09	20.4 %	0.02	0.7 %
$\alpha_{i\,lim}$	0.21	0.10 - 0.30	20.2 %	0.10	0.8 %
S09					
α_o	0.85	0.60 – 0.90	14.2 %	0.78	0.6 %
E_f	2450 m	2300 – 2600 m	14.3	2450 m	4.9 %
$\frac{d\alpha_i}{dZ}$	$0.11\,\mathrm{hm}^{-1}$	$0 – 0.2\,\mathrm{hm}^{-1}$	13.7 %	$0.02\,\mathrm{hm}^{-1}$	1.7 %
a_1	$0.031\,\ln(^\circ\mathrm{C})^{-1}$	$0.01 – 0.1\,\ln(^\circ\mathrm{C})^{-1}$	14.5 %	$0.03\,\ln(^\circ\mathrm{C})^{-1}$	41.4 %
a_2	$-1.68\,\mathrm{day}^{-\frac{1}{2}}$	-2 to $-1.5\,\mathrm{day}^{-\frac{1}{2}}$	14.6 %	$-1.65\,\mathrm{day}^{-\frac{1}{2}}$	29.5 %
a_3	0.011	0.005 – 0.015	14.4 %	0.012	4.6 %
a_4	$30\,\mathrm{hr\,m}^{-1}$	$10 – 100\,\mathrm{hr\,m}^{-1}$	14.2 %	$20\,\mathrm{hr\,m}^{-1}$	4.8 %
α_i	0.33	0 – 0.55	13.8 %	0.40	14.5 %
$\alpha_{s\,lim}$	0.66	0.55 – 0.75	14.9 %	0.67	27.6 %
$\alpha_{f\,lim}$	0.56	0.45 – 0.65	14.3	0.65	0 %
$\alpha_{s\,to\,f}$	0.03	0 – 0.1	14.1 %	0	0.9 %
$\alpha_{i\,lim}$	0.15	0 – 0.30	14.1 %	0.30	0.2 %

Table 5.7: RMSE ranges and values for sensitivity study of albedo parameters, coarse increments, North Glacier.

Variable	Control Value	Value Range	Min RMSE	Optimum Value	Range RMSE
N08					
α_o	0.85	0.60 – 0.90	28.9 %	0.87	21.0 %
E_f	2400 m	2300 – 2500 m	27.3 %	2400 m	7.5 %
$\frac{d\alpha_i}{dZ}$	0 hm^{-1}	0 – 0.15 hm^{-1}	27.3 %	0 hm^{-1}	0 %
a_1	0.042 $\ln(^\circ C)^{-1}$	0.01 – 0.1 $\ln(^\circ C)^{-1}$	29.5 %	0.05 $\ln(^\circ C)^{-1}$	44.4 %
a_2	$-1.71\ day^{-\frac{1}{2}}$	-2 to $-1.5\ day^{-\frac{1}{2}}$	28.1 %	$-1.7\ day^{-\frac{1}{2}}$	33.7 %
a_3	0.01	0.005 – 0.015	28.0 %	0.011	14.1 %
a_4	88 hr m^{-1}	10 – 110 hr m^{-1}	27.2 %	90 hr m^{-1}	15.5 %
α_i	0.44	0.15 – 0.55	26.8 %	0.51	9.0 %
α_{slim}	0.66	0.55 – 0.75	35.1 %	0.67	57.9 %
α_{flim}	0.56	0.45 – 0.65	28.4 %	0.57	13.3 %
α_{stof}	0.03	0 – 0.10	27.3 %	0.01	12.7 %
N09					
α_o	0.85	0.60 – 0.90	10.0 %	0.90	2.8 %
E_f	2480 m	2300 – 2600 m	7.8 %	2570 m	3.7 %
$\frac{d\alpha_i}{dZ}$	0 hm^{-1}	0 – 0.20 hm^{-1}	9.9 %	0 hm^{-1}	18.7 %
a_1	0.03 $\ln(^\circ C)^{-1}$	0.01 – 0.1 $\ln(^\circ C)^{-1}$	9.9 %	0.03 $\ln(^\circ C)^{-1}$	18.2 %
a_2	$-1.61\ day^{-\frac{1}{2}}$	-2 to $-1.5\ day^{-\frac{1}{2}}$	9.8 %	-1.6 $day^{-\frac{1}{2}}$	19.1 %
a_3	0.014	0.005 – 0.02	9.7 %	0.016	5.3
a_4	60 hr m^{-1}	10 – 110 hr m^{-1}	9.9 %	20 hr m^{-1}	1.7 %
α_i	0.43	0.05 – 0.55	10.2 %	0.45	30.2 %
α_{slim}	0.66	0.55 – 0.75	9.6 %	0.61	19.2 %
α_{flim}	0.56	0.45 – 0.55	10.1 %	0.57	2.4 %
α_{stof}	0.03	0 – 0.1	9.9 %	0	0.3 %

Table 5.8: RMSE ranges and values for sensitivity study of albedo parameters, fine increments.

Variable	Control Value	Value Range	Min RMSE	Optimum Value	Range RMSE
S08					
a_1	$0.032\,\ln(°C)^{-1}$	$0.02 – 0.04\,\ln(°C)^{-1}$	20.5 %	$0.032\,\ln(°C)^{-1}$	6.5 %
a_2	$-1.54\,\text{day}^{-\frac{1}{2}}$	-1.6 to $-1.4\,\text{day}^{-\frac{1}{2}}$	20.3 %	$-1.56\,\text{day}^{-\frac{1}{2}}$	1.2 %
a_3	0.007	0.006 – 0.008	20.2 %	0.007	0.5 %
a_4	$44\,\text{hr}\,\text{m}^{-1}$	$1 – 10\,\text{hr}\,\text{m}^{-1}$	19.5 %	$10\,\text{hr}\,\text{m}^{-1}$	5.4 %
α_i	0.34	0.25 – 0.40	19.7 %	0.36	4.8 %
S09					
a_1	$0.031\,\ln(°C)^{-1}$	$0.025 – 0.040\,\ln(°C)^{-1}$	14.3 %	$0.031\,\ln(°C)^{-1}$	2.3 %
a_2	$-1.68\,\text{day}^{-\frac{1}{2}}$	-1.72 to $-1.58\,\text{day}^{-\frac{1}{2}}$	14.3 %	$-1.68\,\text{day}^{-\frac{1}{2}}$	1.9 %
a_3	0.011	0.010 – 0.013	14.3 %	0.012	0.4 %
a_4	$30\,\text{hr}\,\text{m}^{-1}$	$15 – 25\,\text{hr}\,\text{m}^{-1}$	14.0 %	$19\,\text{hr}\,\text{m}^{-1}$	0.8 %
α_i	0.33	0.25 - 0.45	13.5 %	0.37	6.1 %
N08					
a_1	$0.042\,\ln(°C)^{-1}$	0.035 - $0.055\,\ln(°C)^{-1}$	28 %	$0.043\,\ln(°C)^{-1}$	15.3 %
a_2	$-1.71\,\text{day}^{-\frac{1}{2}}$	-1.75 to $-1.65\,\text{day}^{-\frac{1}{2}}$	27.3 %	$-1.71\,\text{day}^{-\frac{1}{2}}$	14.1 %
a_3	0.01	0.01 – 0.012	27.3 %	0.01	8.6 %
a_4	$88\,\text{hr}\,\text{m}^{-1}$	$80 – 100\,\text{hr}\,\text{m}^{-1}$	27.2 %	$90\,\text{hr}\,\text{m}^{-1}$	2.8 %
α_i	0.44	0.4 – 0.55	26.8 %	0.51	9.0 %
N09					
a_1	$0.3\,\ln(°C)^{-1}$	0.25 – 0.45	9.8 %	$0.033\,\ln(°C)^{-1}$	1.2 %
a_2	$-1.61\,\text{day}^{-\frac{1}{2}}$	-1.65 to $-1.55\,\text{day}^{-\frac{1}{2}}$	9.8 %	$-1.6\,\text{day}^{-\frac{1}{2}}$	0.5 %
a_3	0.014	0.015 – 0.017	9.7 %	0.016	0.3 %
α_i	0.43	0.35 – 0.5	9.9 %	0.43	8.3 %

Table 5.9: MPE ranges and values for sensitivity study of albedo parameters, coarse increments, South Glacier.

Variable	Control Value	Value Range	Min MPE	Optimum Value	Range MPE
S08					
α_o	0.85	0.63 – 0.90	−1.6 %	0.63	4.1 %
E_f	2450 m	2300 – 2500 m	0.1 %	2500 m	8.9 %
$\frac{d\alpha_i}{dZ}$	0.15 hm^{-1}	0 – 0.3 hm^{-1}	−1.8 %	0.3 hm^{-1}	8.5 %
a_1	0.032 $\ln(°C)^{-1}$	0.01 – 0.1 $\ln(°C)^{-1}$	0.1 %	0.05 $\ln(°C)^{-1}$	44.6 %
a_2	−1.54 $day^{-\frac{1}{2}}$	−2 to −1 $day^{-\frac{1}{2}}$	0.3 %	−1.3 $day^{-\frac{1}{2}}$	28.2 %
a_3	0.007	0.005 – 0.015	−0.2 %	0.015	7.0 %
a_4	44 $hr\,m^{-1}$	10 – 100 $hr\,m^{-1}$	1.6 %	10 $hr\,m^{-1}$	9.4 %
α_i	0.34	0.1 – 0.55	4.0 %	0.30	35.7 %
α_{slim}	0.66	0.55 – 0.75	−1.7 %	0.65	56.0 %
α_{flim}	0.56	0.45 – 0.65	−1.8 %	0.49	7.6 %
α_{stof}	0.03	0 – 0.09	−4.0 %	0.02	0.6 %
α_{ilim}	0.21	0.1 – 0.3	−3.8 %	0.1	3.7 %
S09					
α_o	0.85	0.60 – 0.9-	−3.1 %	0.6	0.5 %
E_f	2450 m	2300 – 2600 m	−0.7 %	2480 m	9.7 %
$\frac{d\alpha_i}{dZ}$	0.11 hm^{-1}	0 – 0.2 hm^{-1}	−2.1 %	0.2 hm^{-1}	3.2 %
a_1	0.031 $\ln(°C)^{-1}$	0.01 – 0.1 $\ln(°C)^{-1}$	2.8 %	0.04 $\ln(°C)^{-1}$	60.0 %
a_2	−1.68 $day^{-\frac{1}{2}}$	−2 to −1.5 $day^{-\frac{1}{2}}$	1.4 %	−1.6	45.1 %
a_3	0.011	0.005 – 0.015	0.4 %	0.014	17.1 %
a_4	30 $hr\,m^{-1}$	10 – 100 $hr\,m^{-1}$	−0.5 %	20 $hr\,m^{-1}$	12.0 %
α_i	0.33	0 – 0.55	−1.2 %	0.3	29.9 %
α_{slim}	0.66	0.55 – 0.75	−0.2 %	0.65	49.7 %
α_{flim}	0.56	0.45 – 0.65	−3.5 %	0.65	0 %
α_{stof}	0.03	0 – 0.1	−3.0 %	0	1.1 %
α_{ilim}	0.15	0 – 0.3	−3.5 %	0	0.8 %

Table 5.10: MPE ranges and values for sensitivity study of albedo parameters, coarse increments, North Glacier.

Variable	Control Value	Value Range	Min MPE	Optimum Value	Range MPE
N08					
α_o	0.85	0.60 – 0.90	0 %	0.87	34.3 %
E_f	2400 m	2300 – 2500 m	−0.1 %	2300 m	12.3 %
$\frac{d\alpha_i}{dZ}$	$0\,\mathrm{hm}^{-1}$	$0 – 0.15\,\mathrm{hm}^{-1}$	2.1 %	$0\,\mathrm{hm}^{-1}$	0 %
a_1	$0.042\,\ln(^\circ\mathrm{C})^{-1}$	$0.01 – 0.1\,\ln(^\circ\mathrm{C})^{-1}$	−2.1 %	$0.04\,\ln(^\circ\mathrm{C})^{-1}$	94.9 %
a_2	$-1.71\,\mathrm{day}^{-\frac{1}{2}}$	-2 to $-1.5\,\mathrm{day}^{-\frac{1}{2}}$	4.8 %	$-1.7\,\mathrm{day}^{-\frac{1}{2}}$	63.6 %
a_3	0.010	0.005 – 0.015	1.0 %	0.01	34.7 %
a_4	$88\,\mathrm{hr\,m}^{-1}$	$10 – 110\,\mathrm{hr\,m}^{-1}$	0.5 %	$70\,\mathrm{hr\,m}^{-1}$	32.9 %
α_i	0.44	0.15 – 0.55	0.4 %	0.47	4.6 %
α_{slim}	0.66	0.55 – 0.75	−3.8 %	0.67	141.3 %
α_{flim}	0.56	0.45 – 0.65	−0.3 %	0.63	15.6 %
α_{stof}	0.01	0 – 0.1	−1.3 %	0	12.4 %
N09					
α_o	0.85	0.60 – 0.90	−0.1 %	0.81	9.4 %
E_f	2480 m	2300 – 2600 m	−0.2	2510 m	5.4 %
$\frac{d\alpha_i}{dZ}$	$0\,\mathrm{hm}^{-1}$	$0 – 0.2\,\mathrm{hm}^{-1}$	0 %	$0.02\,\mathrm{hm}^{-1}$	16.7 %
a_1	$0.030\,\ln(^\circ\mathrm{C})^{-1}$	$0.01 – 0.1\,\ln(^\circ\mathrm{C})^{-1}$	−0.4 %	$0.04\,\ln(^\circ\mathrm{C})^{-1}$	26.3 %
a_2	$-1.6\,\mathrm{day}^{-\frac{1}{2}}$	-2 to $-1.5\,\mathrm{day}^{-\frac{1}{2}}$	−0.3 %	$-1.5\,\mathrm{day}^{-\frac{1}{2}}$	22.9 %
a_3	0.014	0.005 – 0.02	−0.5 %	0.02	7.3 %
a_4	$60\,\mathrm{hr\,m}^{-1}$	$10 – 110\,\mathrm{hr\,m}^{-1}$	−0.3 %	$10\,\mathrm{hr\,m}^{-1}$	2.6 %
α_i	0.43	0.05 – 0.55	1.6 %	0.40	48.2 %
α_{slim}	0.66	0.55 – 0.75	0.9 %	0.63	26.9 %
α_{flim}	0.56	0.45 – 0.55	−0.9 %	0.45	3.0 %
α_{stof}	0.01	0 – 0.10	−2.0 %	0.01	0.1 %

Table 5.11: MPE ranges and values for sensitivity study of albedo parameters, fine increments.

Variable	Control Value	Value Range	Min MPE	Optimum Value	Range MPE
S08					
$\frac{d\alpha_i}{dZ}$	$0.15\,\mathrm{hm}^{-1}$	$0.05 - 0.15\,\mathrm{hm}^{-1}$	−4.1 %	$0.15\,\mathrm{hm}^{-1}$	4.4 %
a_1	$0.032\,\ln(^\circ\mathrm{C})^{-1}$	$0.02 - 0.04\,\ln(^\circ\mathrm{C})^{-1}$	−2.0 %	$0.04\,\ln(^\circ\mathrm{C})^{-1}$	14.2 %
a_2	$-1.54\,\mathrm{day}^{-\frac{1}{2}}$	-1.6 to $-1.4\,\mathrm{day}^{-\frac{1}{2}}$	−1.2 %	$-1.4\,\mathrm{day}^{-\frac{1}{2}}$	5.9 %
a_3	0.007	0.006 – 0.008	−4.1 %	0.007	1.4 %
a_4	$44\,\mathrm{hr\,m}^{-1}$	$1 - 10\,\mathrm{hr\,m}^{-1}$	−0.2 %	$12\,\mathrm{hr\,m}^{-1}$	13.2 %
α_i	0.34	0.25 – 0.40	−0.6 %	0.31	13.9 %
S09					
a_1	$0.031\,\ln(^\circ\mathrm{C})^{-1}$	$0.025 - 0.040\,\ln(^\circ\mathrm{C})^{-1}$	−0.1 %	$0.035\,\ln(^\circ\mathrm{C})^{-1}$	12.5 %
a_2	$-1.68\,\mathrm{day}^{-\frac{1}{2}}$	-1.72 to -1.58 $\mathrm{day}^{-\frac{1}{2}}$	0.2 %	$-1.62\,\mathrm{day}^{-\frac{1}{2}}$	9.5 %
a_3	0.011	0.010 – 0.013	−1.1 %	0.013	4.7 %
a_4	$30\,\mathrm{hr\,m}^{-1}$	$15 - 25\,\mathrm{hr\,m}^{-1}$	0%	$17\,\mathrm{hr\,m}^{-1}$	3.8 %
α_i	0.33	0.25 – 0.45	−0.4 %	0.29	14.7 %
N08					
a_1	$0.042\,\ln(^\circ\mathrm{C})^{-1}$	$0.035 - 0.055\,\ln(^\circ\mathrm{C})^{-1}$	0.6 %	$0.041\,\ln(^\circ\mathrm{C})^{-1}$	30.0 %
a_2	$-1.71\,\mathrm{day}^{-\frac{1}{2}}$	-1.75 to $-1.65\,\mathrm{day}^{-\frac{1}{2}}$	0.6 %	$-1.72\,\mathrm{day}^{-\frac{1}{2}}$	15.0 %
a_3	0.010	0.010 – 0.012	0.5 %	0.010	4.9 %
a_4	$88\,\mathrm{hr\,m}^{-1}$	$80 - 100\,\mathrm{hr\,m}^{-1}$	−0.5 %	$84\,\mathrm{hr\,m}^{-1}$	4.9 %
α_i	0.44	0.4 – 0.55	0.3 %	0.48	17.7 %
N09					
a_1	$0.30\,\ln(^\circ\mathrm{C})^{-1}$	0.25 – 0.45	0 %	$0.045\,\ln(^\circ\mathrm{C})^{-1}$	4.2 %
a_2	$-1.61\,\mathrm{day}^{-\frac{1}{2}}$	-1.65 to $-1.55\,\mathrm{day}^{-\frac{1}{2}}$	−0.9 %	$-1.55\,\mathrm{day}^{-\frac{1}{2}}$	1.9 %
a_3	0.014	0.015 – 0.017	−1.4 %	0.016	0.5 %
α_i	0.43	0.35 – 0.50	0.3%	0.41	20.9 %

5.1.3 Roughness parameters

The Brock et al. (2006) parameterization of aerodynamic roughness length evolution contains six parameters: the quantity of snowfall required to reset the roughness length to initial conditions (Z_{thr}), the invariant roughness length of ice ($Z_{o\text{i}}$), and $b_{1:4}$ which determine the shape of the evolution function. In all of the simulations, except for North Glacier 2008, perturbing the roughness length parameters creates a range in RMSE of 2%. For North Glacier 2008, the RMSE range between $9-12\%$ (Tables 5.12, 5.13 and Figure 5.4). Overall this demonstrates that the roughness length has only a very limited control over model skill. This is particularly reassuring for the roughness length of ice, as this parameter is poorly constrained.

As recommended by Brock et al. (2006) ice roughness length is parameterized in two ways: first, as a mean value of all measured ice roughness lengths, and second, as a value selected stochastically from the log-normal probability density function derived from all measured ice roughness lengths. The two methods produce results that are identical to the second decimal place. Therefore the mean value is used in all further simulations as it is less computationally burdensome.

Aerodynamic roughness length is commonly used as a tuning parameter in energy balance models (e.g Hock and Holmgren, 2005). In order to facilitate comparison with previous models, we tuned the South Glacier 2008 data set using snow and ice aerodynamic roughness lengths. The best fit produced a RMSE 1.5% lower than the control run RMSE, but used roughness lengths much larger that those observed in the field: 9 mm for snow and 5.5 mm for ice. This result indicates that tuning with roughness length has very limited ability to optimize a DEBM in our study area; roughness values obtained from tuning will not necessary reflect actual roughness lengths, but instead act to absorb error from other aspects of the model (Anslow et al., 2008).

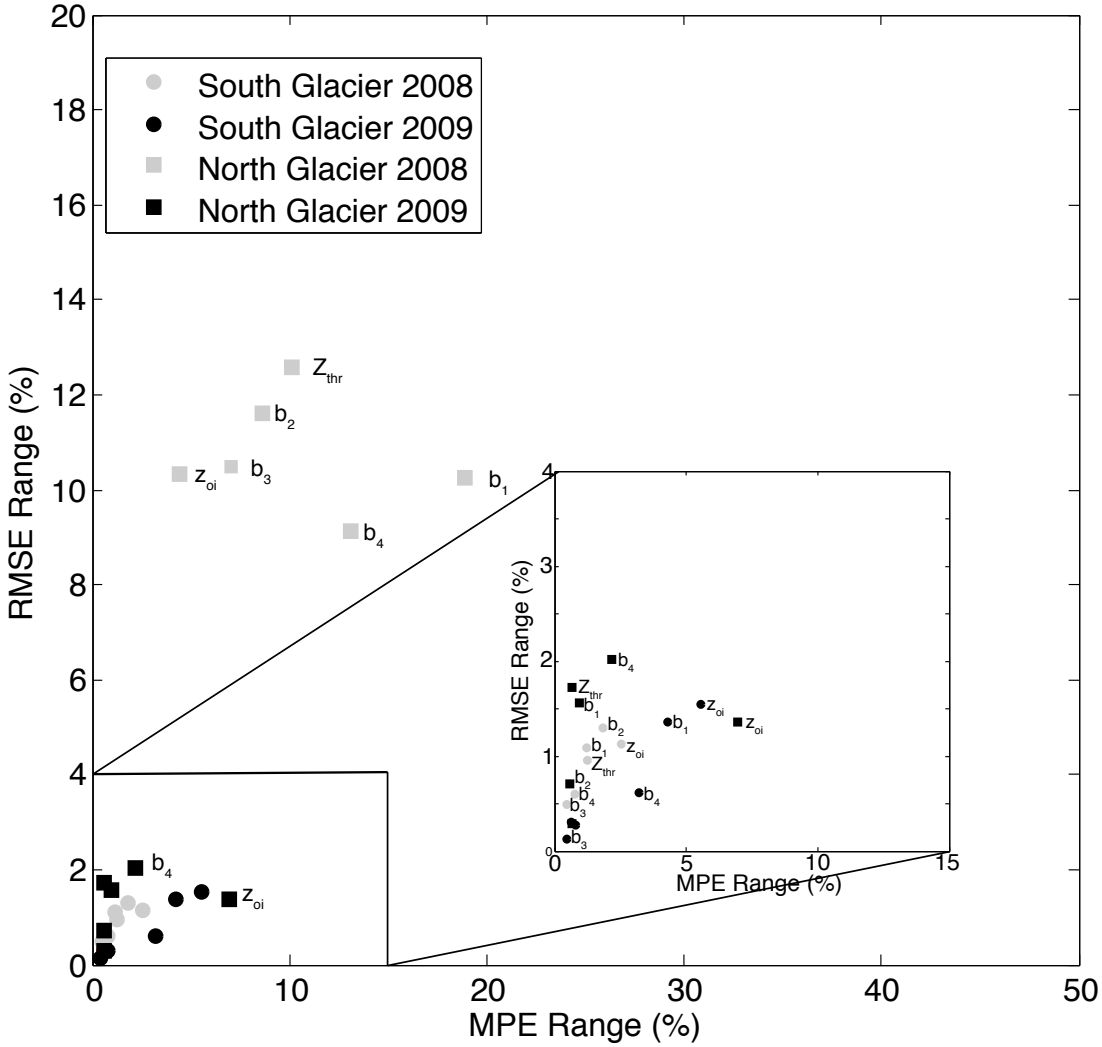

Figure 5.4: Roughness parameters displayed by their sensitivity ranges in MPE vs. RMSE.

Table 5.12: RMSE ranges and values for sensitivity study of roughness parameters.

Variable	Control Value	Value Range	Min RMSE	Optimum Value	Range RMSE
S08					
Z_{thr}	0.01 m	0.01 – 0.05 m	20.3 %	0.04 m	1.0 %
b_1	0.91 mm	0.2 – 2 mm	20.0 %	1.4 mm	1.1 %
b_2	1.36 °C	0.5 – 1.5 °C	19.8 %	1 °C	1.3 %
b_3	0.05 °C	0.01 – 0.1 °C	20.2 %	0.02 °C	0.5 %
b_4	2.3 mm	1 – 3 mm	20.2 %	1.6 mm	0.6 %
$z_{o\text{i}}$	0.65 mm	0.01 – 10 mm	20.0 %	5.5 mm	1.1 %
S09					
Z_{thr}	0.01 m	0.01 – 0.05 m	14.0 %	0.01 m	0.3 %
b_1	0.91 mm	0.2 – 2 mm	14.1 %	0.2 %	1.4 %
b_2	1.36 °C	0.5 – 1.5 °C	14.2 %	0.9 °C	0.3 %
b_3	0.05 °C	0.01 – 0.1 °C	14.3 %	0.08 °C	0.1 %
b_4	2.3 mm	1 – 3 mm	14.3 %	2.2 mm	0.6 %
$z_{o\text{i}}$	0.65 mm	0.01 – 10 mm	14.1 %	0.01 mm	1.6 %
N08					
Z_{thr}	0.01 m	0.01 – 0.05 m	27.0 %	0.02 m	12.6 %
b_1	0.91 mm	0.2 – 2 mm	29.3 %	1.4 mm	10.2 %
b_2	1.36 °C	0.5 – 1.5 °C	26.0 %	1.3 °C	11.6 %
b_3	0.05 °C	0.01 – 0.1 °C	27.2 %	0.05 °C	10.5 %
b_4	2.3 mm	1 – 3 mm	29.5 %	2.4 mm	9.1 %
$z_{o\text{i}}$	0.2 mm	0.01 – 10 mm	27.4 %	2 mm	10.3 %
N09					
Z_{thr}	0.01 m	0.01 – 0.05 m	9.7 %	0.04 m	1.7 %
b_1	0.91 mm	0.2 – 2 mm	9.9 %	1 mm	1.6 %
b_2	1.36 °C	0.5 – 1.5 °C	9.8 %	1.3 °C	0.7 %
b_3	0.05 °C	0.01 – 0.1 °C	9.9 %	0.01 °C	0.3 %
b_4	2.3 mm	1 – 3 mm	9.9 %	2.2 mm	2.0 %
$z_{o\text{i}}$	0.2 mm	0.01 – 1 mm	10.1 %	0.01 mm	1.4 %

Table 5.13: MPE ranges and values for sensitivity study of roughness parameters.

Variable	Control Value	Value Range	Min MPE	Optimum Value	Range MPE
S08					
Z_{thr}	0.01 m	0.01 – 0.05 m	−3.6 %	0.04 m	1.2 %
b_1	0.91 mm	0.2 – 2 mm	−3.9 %	1.8 mm	1.2 %
b_2	1.36 °C	1 – 3 °C	−3.5 %	1 °C	1.8 %
b_3	0.05 °C	0.01 – 0.1 °C	−3.9 %	0.01 °C	0.5 %
b_4	2.3 mm	1 – 3 mm	−4.1 %	2.2 mm	0.8 %
$z_{o\text{i}}$	0.65 mm	0.01 – 10 mm	−3.0 %	10 mm	2.5 %
S09					
Z_{thr}	0.01 m	0.01 – 0.05 m	−3.2 %	0.05 m	0.6 %
b_1	0.91 mm	0.2 – 2 mm	−1.0 %	2 mm	4.3 %
b_2	1.36 °C	0.5 – 1.5 °C	−3.1 %	0.5 °C	0.8 %
b_3	0.05 °C	0.01 – 0.1 °C	−3.3 %	0.01 °C	0.5 %
b_4	2.3 mm	1 – 3 mm	−1.6 %	1 mm	3.2 %
$z_{o\text{i}}$	0.65 mm	0.01 – 10 mm	0 %	6 mm	5.6 %
N08					
Z_{thr}	0.01 m	0.01 – 0.05 m	−0.3 %	0.03 m	10.1 %
b_1	0.91 mm	0.2 – 2 mm	0.4 %	1.2 mm	18.9 %
b_2	1.36 °C	0.5 – 1.5 °C	−0.3 %	1.2 °C	8.6 %
b_3	0.05 °C	0.01 – 0.1 °C	1.0 %	0.09 °C	7.0 %
b_4	2.3 mm	1 – 3 mm	−0.3 %	2.4 mm	13.1 %
$z_{o\text{i}}$	0.2 mm	0.01 – 10 mm	0.1 %	9 mm	4.5 %
N09					
Z_{thr}	0.01 m	0.01 – 0.05 m	−1.9 %	0.02 m	0.7 %
b_1	0.91 mm	0.2 – 2 mm	−1.8 %	1.2 mm	0.9 %
b_2	1.36 °C	0.5 – 1.5 °C	−1.7 %	1.2 °C	0.6 %
b_3	0.05 °C	0.01 – 0.1 °C	−1.9 %	0.01 °C	0.7 %
b_4	2.3 mm	1 – 3 mm	−1.5 %	1 mm	2.2 %
$z_{o\text{i}}$	0.2 mm	0.01 – 1 mm	0.2 %	3 mm	7.0 %

5.1.4 Lapse Rates

The DEBM utilizes a lapse rate for temperature Γ_T and a lapse rate for precipitation Γ_P. The RMSE range created by perturbing the temperature lapse rate is high for North Glacier 2008: 32%, and moderate for the other simulations: $3-7\%$ (Tables 5.14, 5.15, Figure 5.5). This relatively modest sensitivity is somewhat surprising considering the strong effect temperature has on turbulent heat fluxes, simulated albedo evolution, and simulated roughness length evolution.

Perturbing the precipitation lapse rate has a moderate effect on the RMSE range of $3-11\%$. The RMSE range is lower in the 2009 simulations than the 2008 simulations likely because there was far more summer snowfall in 2008 than 2009.

Table 5.14: RMSE ranges and values for sensitivity study of lapse rates.

Variable	Control Value	Value Range	Min RMSE	Optimum Value	Range RMSE
S08					
Γ_T	$-6.03\,K\,km^{-1}$	-9 – $0\,K\,km^{-1}$	19.6 %	$0\,K\,km^{-1}$	5.7 %
Γ_p	$2.3\,mm\,km^{-1}$	0 – $10\,mm\,km^{-1}$	20.2 %	$0\,mm\,km^{-1}$	6.2 %
S09					
Γ_T	$-6.03\,K\,km^{-1}$	-9 – $0\,K\,km^{-1}$	12.9 %	$-4\,K\,km^{-1}$	6.9 %
Γ_p	$2.3\,mm\,km^{-1}$	0 – $10\,mm\,km^{-1}$	14.1 %	$1\,mm\,km^{-1}$	1.9 %
N08					
Γ_T	$-5.3\,K\,km^{-1}$	-9 – $0\,K\,km^{-1}$	28.2 %	$-5\,K\,km^{-1}$	32.8 %
Γ_p	$1.2\,mm\,km^{-1}$	0 – $10\,mm\,km^{-1}$	31.6 %	$2\,mm\,km^{-1}$	10.9 %
N09					
Γ_T	$-5.3\,K\,km^{-1}$	-9 – 0	9.7 %	$-5\,K\,km^{-1}$	5.8 %
Γ_p	$1.2\,mm\,km^{-1}$	0 – $10\,mm\,km^{-1}$	10.2 %	$1\,mm\,km^{-1}$	4.4 %

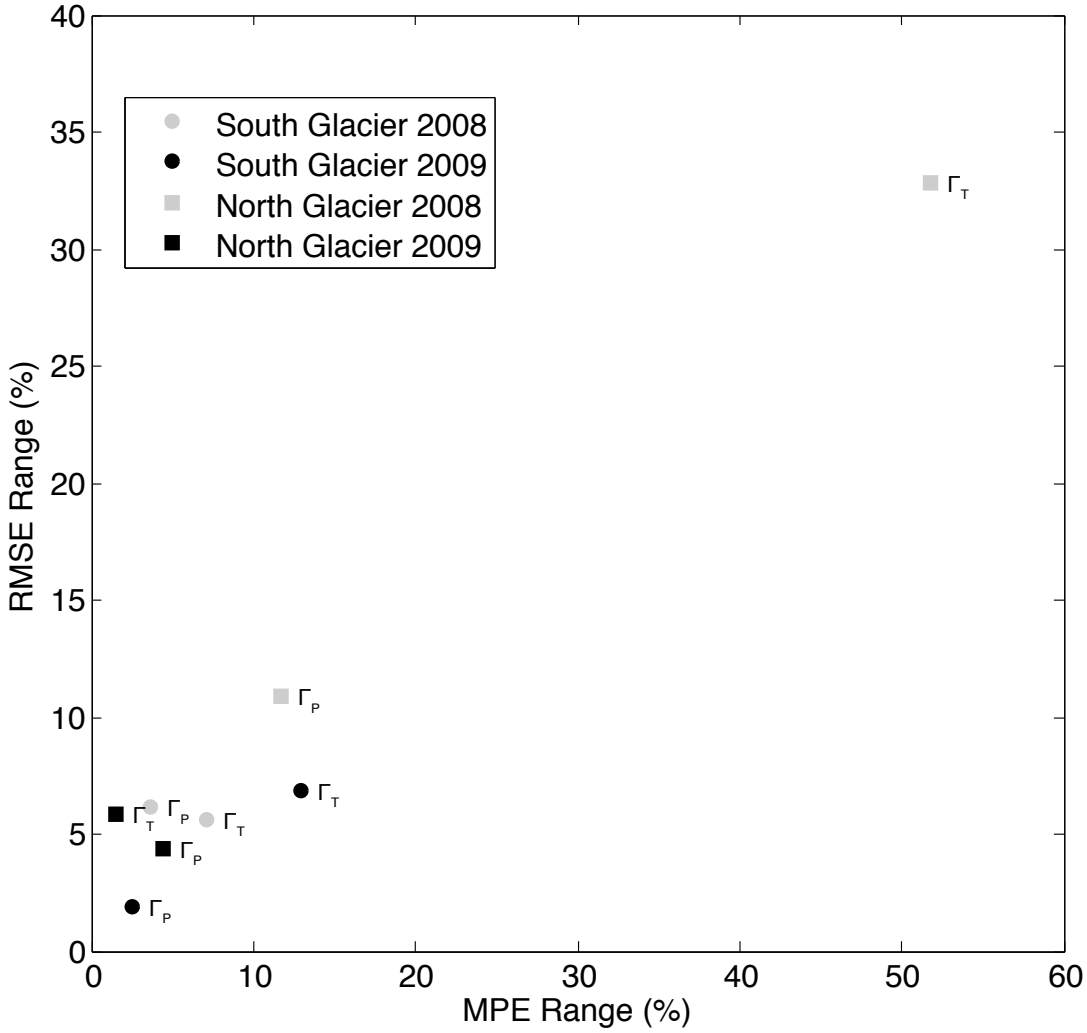

Figure 5.5: Lapse rates displayed by their sensitivity ranges in MPE vs. RMSE.

Table 5.15: MPE ranges and values for sensitivity study of lapse rates.

Variable	Control Value	Value Range	Min MPE	Optimum Value	Range MPE
S08					
Γ_T	$-6.03\,K\,km^{-1}$	-9 – $0\,K\,km^{-1}$	$-2.0\,\%$	$0\,K\,km^{-1}$	$7.1\,\%$
Γ_p	$2.3\,mm\,km^{-1}$	0 – $10\,mm\,km^{-1}$	$-4.0\,\%$	$1\,mm\,km^{-1}$	$3.6\,\%$
S09					
Γ_T	$-6.03\,K\,km^{-1}$	-9 – $0\,K\,km^{-1}$	$-0.4\,\%$	$-4\,K\,km^{-1}$	$12.9\,\%$
Γ_p	$2.3\,mm\,km^{-1}$	0 – $10\,mm\,km^{-1}$	$-1.4\,\%$	$4\,mm\,km^{-1}$	$2.5\,\%$
N08					
Γ_T	$-5.3\,K\,km^{-1}$	-9 – $0\,K\,km^{-1}$	$0.3\,\%$	$-6\,K\,km^{-1}$	$51.8\,\%$
Γ_p	$1.2\,mm\,km^{-1}$	0 – $10\,mm\,km^{-1}$	$0.9\,\%$	$4\,mm\,km^{-1}$	$11.7\,\%$
N09					
Γ_T	$-5.3\,K\,km^{-1}$	-9 – $0\,K\,km^{-1}$	$-1.9\,\%$	$-6\,K\,km^{-1}$	$1.5\,\%$
Γ_p	$1.2\,mm\,km^{-1}$	0 – $10\,mm\,km^{-1}$	$-0.6\,\%$	$10\,mm\,km^{-1}$	$4.4\,\%$

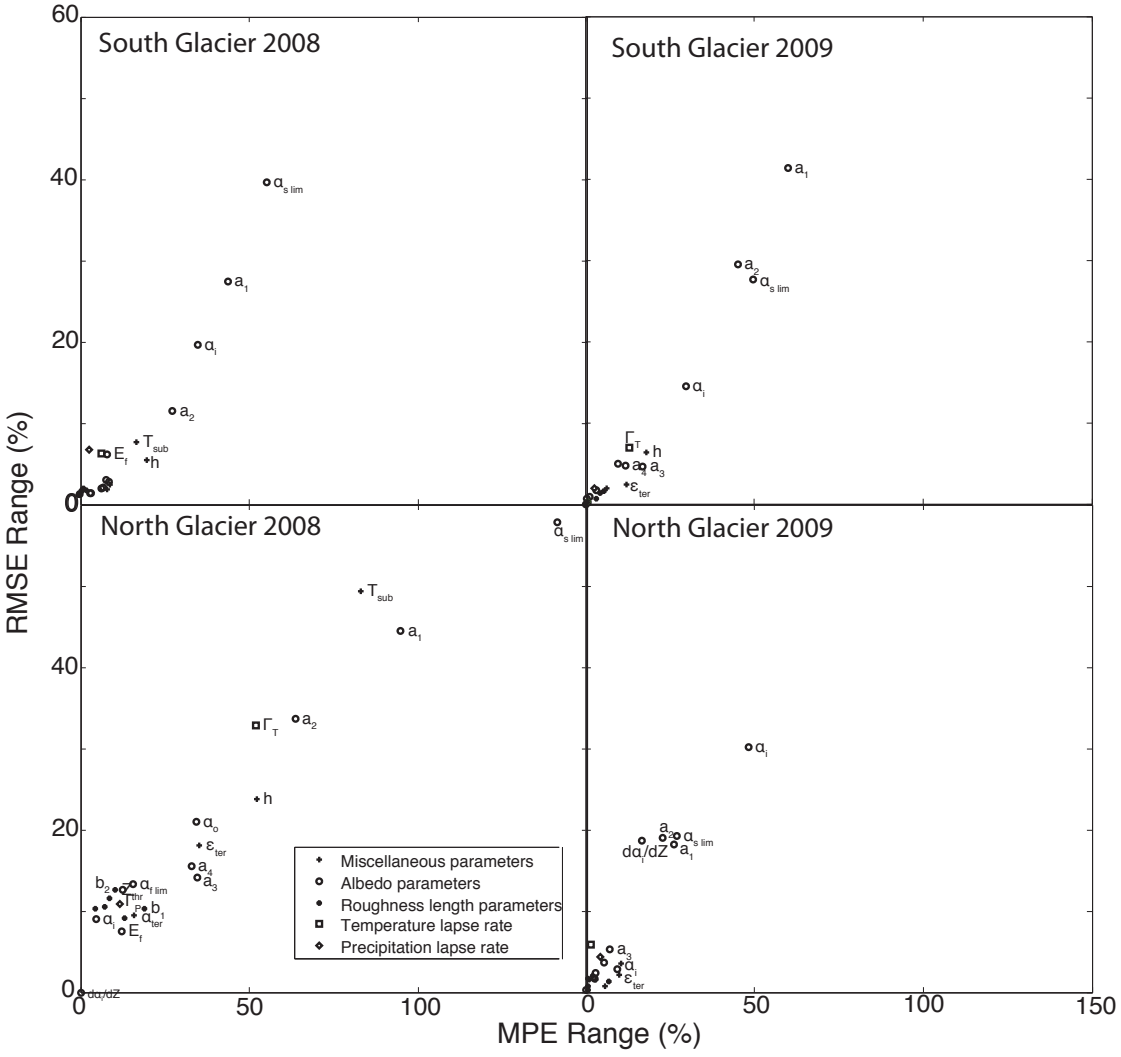

Figure 5.6: Parameters displayed by their sensitivity ranges in MPE vs. RMSE. Each panel is one simulation. Notice that the albedo parameters tend to the upper right of the panels.

5.1.5 Optimum parameter runs

To assess the effect of parameter optimization on model skill a series of tests were carried out in which the control run parameter values were replaced by the parameter values that individually minimize the RMSE for each of the data sets. Results show that using the optimized parameter values reduces the skill of the model for three of the data sets (South Glacier 2008, South Glacier 2009 and North Glacier 2008) and slightly improved model skill for North Glacier 2009 (Table 5.16). This result demonstrates that the model cannot be tuned by individually optimizing each parameter value.

Table 5.16: MPE and RMSE for control parameter values and simulations with parameter values that individually minimize RMSE.

Data-set	Control MPE (%)	Control RMSE(%)	Optimized MPE(%)	Optimized RMSE(%)
S08	-11.0	22.7	15.0	30.6
S09	-10.4	14.3	-15.6	21.3
N08	17.8	30.5	7.1	37.7
N09	-10.6	15.4	4.0	14.8

5.2 Model sensitivity to perturbing meteorological inputs

The DEBM is forced by nine meteorological variables: barometric pressure (p_c), relative humidity (ϕ), air temperature (T_a), wind speed (u_z), direct shortwave radiation (I), diffuse shortwave radiation (D), incoming longwave radiation (L_{in}), rainfall rate(P_r) and snowfall rate (P_s); and one initial condition, initial snow depth in w.e. (*swe*). Each of these variables is associated with a measurement uncertainty taken from the instrument manuals for the measured meteorological variables and estimated from field evidence for initial snow depth (Table 5.18 – 5.21).

To assess the model sensitivity to measurement uncertainty the method of Anslow et al. (2008) was followed. (Wherein the error associated with each variable is interpreted as a systematic error instead of a random error and the magnitude of the error is added to that of the variable for all time steps.) This method produces a maximum range of model error associated with the uncertainty in each variable, a worst case scenario. The variables were perturbed one at a time. As with the sensitivity tests for the model parameters MPE and RMSE ranges are used to quantify the sensitivity to measurement uncertainty in each variable.

The results of this analysis show that the model is sensitive to three variables in particular: wind speed, incoming longwave radiation, and initial w.e. snow depth (Table 5.18 – 5.21 and Figure 5.7). These are the variables that are the least well constrained, due to the assumption of spatial uniformity for wind speed, the quality of the instrument used to infer incoming longwave radiation, and the spatial complexity in initial snow distribution. As for the parameter sensitivities, the North Glacier 2008 data set has a higher sensitivity to changes in any variable compared to the other simulations.

To distinguish whether the model is sensitive to a given perturbation in the variable or the constraint on the uncertainty associated with the variable each variable was perturbed by $\pm$10%(Table 5.22 – 5.25, Figure 5.8). The results of this test show that the model is most sensitive to a $\pm$10 % change in temperature, incoming longwave radiation and incoming direct shortwave radiation. Some of the perturbations in this test are physically unrealistic such as a 10 % change in temperature which is approximately a $\pm$27 K perturbation in temperature. Nonetheless this demonstrates that the model is very sensitive to temperature, but that the small uncertainty associated with measuring temperature and the

ease of extrapolating temperature compensate for the high sensitivity. In the reverse the model is relatively insensitive to a 10 % change in wind speed but the uncertainty associated with wind speed are much greater than 10 %, therefore wind speed contributes more to overall model uncertainty.

The deviations from measured values that produce the minimum RMSE either increase the amount of heat received by the glacier or reduce snowfall or initial snow-depth. This makes sense as three of the control runs (South Glacier 2008, South Glacier 2009 and North Glacier 2009) underestimate melt. Whether this indicates that there is an actual systematic offset in one or more of the variables or a deficiency of model design is unknown.

Table 5.17: Meteorological forcings that drive the DEBM, their units and symbols.

Variable symbol	Units	Meteorological variable
p_c	mbar	Barometric pressure
ϕ	%	Relative humidity
T_a	°C	Air temperature
u_z	ms^{-1}	Wind speed
I	Wm^{-2}	Direct incoming shortwave
D	Wm^{-2}	Diffuse incoming shortwave
L_{in}	Wm^{-2}	Incoming longwave
P_r	$m\,hr^{-1}$	Rainfall rate
P_s	$m\,hr^{-1}$	Snowfall rate
swe	m	Initial snow depth

Table 5.18: South Glacier RMSE sensitivity to uncertainty in meteorological variables and initial snow-depth.

Met. Variable	Uncertainty	Min RMSE	Optimum Deviation	Range RMSE
S08				
p_c	± 0.5 mbar	22.8 %	0.2 mbar	0 %
ϕ	± 4 %	22.4 %	4 %	0.8 %
T_a	± 0.28 K	21.8 %	0.28 K	2.3 %
u_z	± 3 ms^{-1}	21.0 %	1 ms^{-1}	4.7 %
I	± 3 %	21.5 %	3 %	3.4 %
D	± 3 %	22.2 %	3 %	1.3 %
L_{in}	± 5 %	20.6 %	4 %	8.9 %
P_r	± 20 %	22.8 %	0 %	0 %
P_s	± 20 %	21.8 %	-18 %	2.1 %
swe	± 50 %	22.6	-50	12.0 %
S09				
p_c	± 0.5 mbar	16.2 %	0.5 mbar	0 %
ϕ	± 4 %	15.7 %	4%	1.4 %
T_a	± 0.28 K	15.1 %	0.28 K	3.4 %
u_z	± 3 ms^{-1}	16.2 %	0 ms^{-1}	17.1 %
I	± 3 %	15.6 %	2 %	2.3 %
D	± 3 %	15.9 %	3 %	0.8 %
L_{in}	± 5 %	15.4 %	3 %	9.7 %
P_r	± 20 %	16.2 %	0 %	0 %
P_s	± 20 %	15.8 %	-20 %	0.6 %
swe	± 50 %	13.2 %	-10 %	17.9 %

Table 5.19: North Glacier RMSE sensitivity to uncertainty in meteorological variables and initial snow-depth.

Met. Variable	Uncertainty	Min RMSE	Optimum Deviation	Range RMSE
N08				
p_c	± 0.5 mbar	39.3 %	-0.1 mbar	0.3 %
ϕ	± 4 %	28.0 %	3 %	12.2 %
T_a	± 0.28 K	28.9 %	0.06 K	15.7 %
u_z	± 3 ms^{-1}	32.7 %	2 ms^{-1}	41.8 %
I	± 3 %	28.1 %	1 %	11.5 %
D	± 3 %	27.9 %	3 %	11.7 %
L_{in}	± 5 %	33.6 %	1 %	48.3 %
P_r	± 20 %	39.6 %	0 %	0 %
P_s	± 20 %	31.5 %	-4 %	9.7 %
swe	± 50 %	28.3 %	0 %	37.5 %
N09				
p_c	± 0.5 mbar	15.2 %	0.4 mbar	0 %
ϕ	± 4 %	13.2 %	4 %	3.0 %
T_a	± 0.28 K	12.3 %	0.28 K	4.9 %
u_z	± 3 ms^{-1}	12.5 %	1 ms^{-1}	19.3 %
I	± 3 %	12.4 %	2 %	5.4 %
D	± 3 %	13.5 %	1 %	1.6 %
L_{in}	± 5 %	10.4 %	5 %	11.7 %
P_r	± 20 %	15.2 %	0 %	0 %
P_s	± 20 %	14.0 %	-2 %	1.1 %
swe	± 50 %	9.9 %	-40 %	12.9 %

Table 5.20: South Glacier MPE sensitivity to uncertainty in meteorological variables and initial snow-depth.

Met. Variable	Uncertainty	Min MPE	Optimum Deviation	Range MPE
S08				
p_c	± 0.5 mbar	-9.9 %	0.2 mbar	0 %
ϕ	± 4 %	-8.9 %	4 %	2.0 %
T_a	± 0.28 K	-7.0 %	0.28 K	6.0 %
u_z	± 3 ms^{-1}	-2.1 %	1 ms^{-1}	21.1 %
I	± 3 %	-4.9 %	3 %	9.9 %
D	± 3 %	-8.2 %	3 %	3.6 %
L_{in}	± 5 %	-0.6 %	4 %	22.8 %
P_r	± 20 %	-9.9 %	0 %	0 %
P_s	± 20 %	-7.8 %	-18 %	4.5 %
swe	± 50 %	-4.2 %	-50 %	17.0 %
S09				
p_c	± 0.5 mbar	-10 %	0.5 mbar	0 %
ϕ	± 4 %	-8.2 %	4 %	3.7 %
T_a	± 0.28 K	-6.2 %	0.28 K	8.0 %
u_z	± 3 ms^{-1}	1.7 %	1 ms^{-1}	39.0 %
I	± 3 %	-4.4 %	3 %	9.2 %
D	± 3 %	-8.7 %	3 %	2.8 %
L_{in}	± 5 %	0.2 %	4 %	24.7 %
P_r	± 20 %	-10 %	0 %	0 %
P_s	± 20 %	-7.5 %	-20 %	3.7 %
swe	± 50 %	0.06 %	-25 %	37.5 %

Table 5.21: North Glacier MPE sensitivity to uncertainty in meteorological variables and initial snow depth.

Met. Variable	Uncertainty	Min MPE	Optimum Deviation	Range MPE
N08				
p_c	± 0.5 mbar	-10.6 %	-0.1 mbar	0.4 %
ϕ	± 4 %	-1.2 %	3 %	10.7 %
T_a	± 0.28 K	-0.6 %	0.06 K	25.9 %
u_z	± 3 ms^{-1}	-11.0 %	0 ms^{-1}	58.7 %
I	± 3 %	-0.9 %	1 %	22.7 %
D	± 3 %	0 %	3 %	11.7 %
L_{in}	± 5 %	4.0 %	1 %	76.5 %
P_r	± 20 %	-11.0 %	0 %	0 %
P_s	± 20 %	-2.6 %	16 %	9.3 %
swe	± 50 %	0 %	25 %	41.0 %
N09				
p_c	± 0.5 mbar	-9.6 %	0.5 mbar	0 %
ϕ	± 4 %	-7.8 %	4 %	3.3 %
T_a	± 0.28 K	-6.5 %	0.28 K	6.2 %
u_z	± 3 ms^{-1}	2.7 %	1 ms^{-1}	50.3 %
I	± 3 %	-5.8 %	3 %	7.8 %
D	± 3 %	-8.2 %	3 %	2.3 %
L_{in}	± 5 %	0.28 K	5 %	19.6 %
P_r	± 20 %	-9.7 %	0 %	0 %
P_s	± 20 %	-8.3 %	-18 %	2.6 %
swe	± 50 %	-2.4 %	-40 %	15.7 %

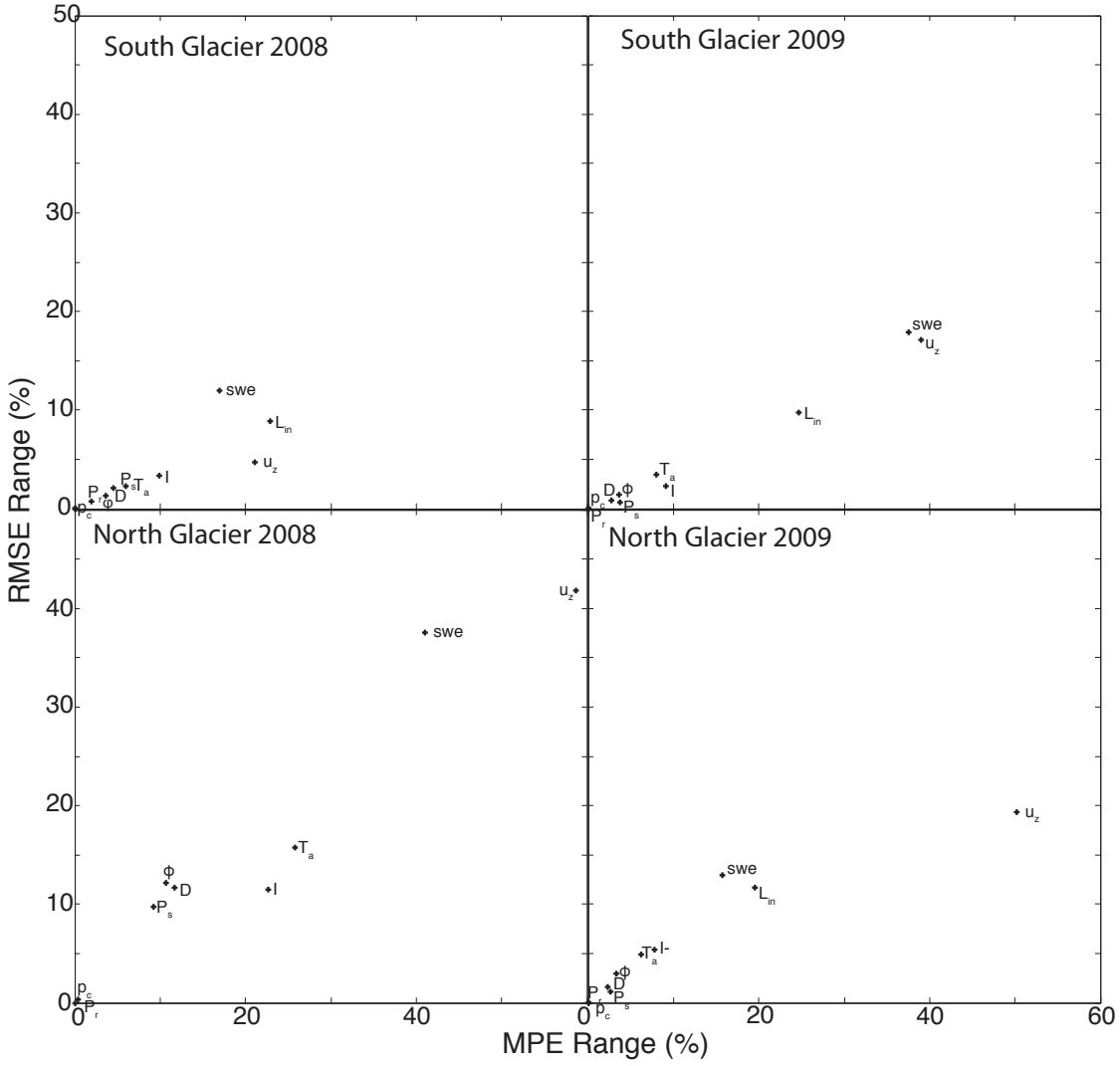

Figure 5.7: Sensitivity ranges in MPE vs. RMSE for meteorological variable and initial snow-depth uncertainty. Each panel is one simulation. Notice that wind speed, incoming longwave radiation and initial snow-depth tend to the upper right of the panels.

Table 5.22: South Glacier RMSE sensitivity to a $\pm 10\,\%$ perturbation in meteorological variables and initial snow depth.

Met. Variable	Uncertainty	Min. RMSE	Optimum deviation	Range RMSE
S08				
p_c	$\pm$10%	22.5 %	10.0 %	0.4 %
ϕ	$\pm$10%	22.0 %	10.0 %	2.0 %
T_a	$\pm$10%	22.8 %	0.0 %	306.7 %
u_z	$\pm$10%	21.9 %	10.0 %	1.0 %
I	$\pm$10%	21.1 %	4.0 %	10.6 %
D	$\pm$10%	21.3 %	10.0 %	4.0 %
L_{in}	$\pm$10%	20.6 %	4.0 %	19.7 %
P_r	$\pm$10%	22.8 %	0.0 %	0.0 %
P_s	$\pm$10%	22.2 %	-10.0	1.0 %
swe	$\pm$10%	21.8 %	-4.0 %	9.8 %
S09				
p_c	$\pm$10%	15.8 %	10.0 %	0.9 %
ϕ	$\pm$10%	15.1 %	10.0 %	3.7 %
T_a	$\pm$10%	16.2 %	0.0 %	385.2 %
u_z	$\pm$10%	15.7 %	10.0 %	1.5 %
I	$\pm$10%	15.6 %	2.0 %	15.1 %
D	$\pm$10%	15.7 %	10.0 %	1.9 %
L_{in}	$\pm$10%	15.8 %	2.0 %	16.5 %
P_r	$\pm$10%	16.2 %	0.0 %	0.0 %
P_s	$\pm$10%	16.2 %	-2.0 %	0.2 %
swe	$\pm$10%	13.2 %	-8.0 %	4.5 %

Table 5.23: North Glacier RMSE sensitivity to a $\pm 10\,\%$ perturbation in meteorological variables and initial snow-depth.

Met. Variable	Uncertainty	Min. RMSE	Optimum deviation	Range RMSE
N08				
p_c	$\pm$10%	32.8 %	$-2.0\,\%$	6.8 %
ϕ	$\pm$10%	26.6 %	6.0 %	13.0 %
T_a	$\pm$10%	39.6 %	0.0 %	695.5 %
u_z	$\pm$10%	33.3 %	$-7.0\,\%$	6.6 %
I	$\pm$10%	31.6 %	2.0 %	75.1 %
D	$\pm$10%	28.1 %	4.0 %	11.5 %
L_{in}	$\pm$10%	39.6 %	0.0 %	86.9 %
P_r	$\pm$10%	39.6 %	0.0 %	0.0 %
P_s	$\pm$10%	31.5 %	$-4.0\,\%$	8.6 %
swe	$\pm$10%	28.3 %	0.0 %	21.7 %
N09				
p_c	$\pm$10%	13.1 %	10.0 %	2.6 %
ϕ	$\pm$10%	12.0 %	10.0 %	5.0 %
T_a	$\pm$10%	15.2 %	0.0 %	205.0 %
u_z	$\pm$10%	12.8 %	8.0 %	4.6 %
I	$\pm$10%	11.0 %	8.0 %	12.7 %
D	$\pm$10%	12.5 %	6.0 %	4.4 %
L_{in}	$\pm$10%	10.4 %	4.0 %	22.9 %
P_r	$\pm$10%	15.2 %	0.0 %	0.0 %
P_s	$\pm$10%	14.0 %	$-2.0\,\%$	1.1 %
swe	$\pm$10%	12.1 %	$-10.0\,\%$	2.7 %

Table 5.24: South Glacier MPE sensitivity to a ±10 % perturbation in meteorological variables and initial snow-depth.

Met. Variable	Uncertainty	Min. MAE	Optimum deviation	Range MAE
S08				
p_c	±10%	−9.4 %	10.0 %	0.9 %
ϕ	±10%	−7.6 %	10.0 %	5.0 %
T_a	±10%	−9.9 %	0.0 %	418.5 %
u_z	±10%	−8.5 %	10.0 %	1.7 %
I	±10%	0.7 %	6.0 %	32.0 %
D	±10%	−3.3 %	10.0 %	11.9 %
L_{in}	±10%	−0.6 %	4.0 %	49.2 %
P_r	±10%	−9.9 %	0.0 %	0.0 %
P_s	±10%	−8.8 %	−10.0 %	2.5 %
swe	±10%	−10.1 %	−4.0 %	6.4 %
S09				
p_c	±10%	−9.0 %	10.0 %	2.3 %
ϕ	±10%	−5.3 %	10.0 %	9.2 %
T_a	±10%	−10.0 %	0.0 %	472.8 %
u_z	±10%	−7.5 %	10.0 %	4.6 %
I	±10%	0.8 %	6.0 %	35.9 %
D	±10%	−5.4 %	10.0 %	7.3 %
L_{in}	±10%	0.2 %	4.0 %	43.6 %
P_r	±10%	−10.0 %	0.0 %	0.0 %
P_s	±10%	−9.2 %	−10.0 %	1.4 %
swe	±10%	−6.4 %	−10.0 %	7.8 %

Table 5.25: North Glacier MPE sensitivity to a ±10 % perturbation in meteorological variables and initial snow-depth.

Met. Variable	Uncertainty	Min. MAE	Optimum deviation	Range MAE
N08				
p_c	±10%	−6.5 %	10.0 %	4.5 %
ϕ	±10%	0.3 %	6.0 %	18.2 %
T_a	±10%	−11.0 %	0.0 %	832.8 %
u_z	±10%	−2.3 %	−10.0 %	10.2 %
I	±10%	−1.2 %	2.0 %	96.4 %
D	±10%	1.3 %	6.0 %	31.1 %
L_{in}	±10%	−11.0 %	0.0 %	148.4 %
P_r	±10%	−11.0 %	0.0 %	0.0 %
P_s	±10%	−5.9 %	−4.0 %	6.0 %
swe	±10%	11.4 %	6.0 %	18.5 %
N09				
p_c	±10%	−7.7 %	10.0 %	3.3 %
ϕ	±10%	−5.6 %	10.0 %	7.2 %
T_a	±10%	−9.7 %	0.0 %	319.5 %
u_z	±10%	−7.1 %	8.0 %	6.4 %
I	±10%	0.0 %	8.0 %	24.2 %
D	±10%	−6.1 %	10.0 %	7.3 %
L_{in}	±10%	−2.0 %	4.0 %	40.3 %
P_r	±10%	−9.7 %	0.0 %	0.0 %
P_s	±10%	−9.0 %	−2.0 %	1.0 %
swe	±10%	−6.8 %	−10.0 %	3.5 %

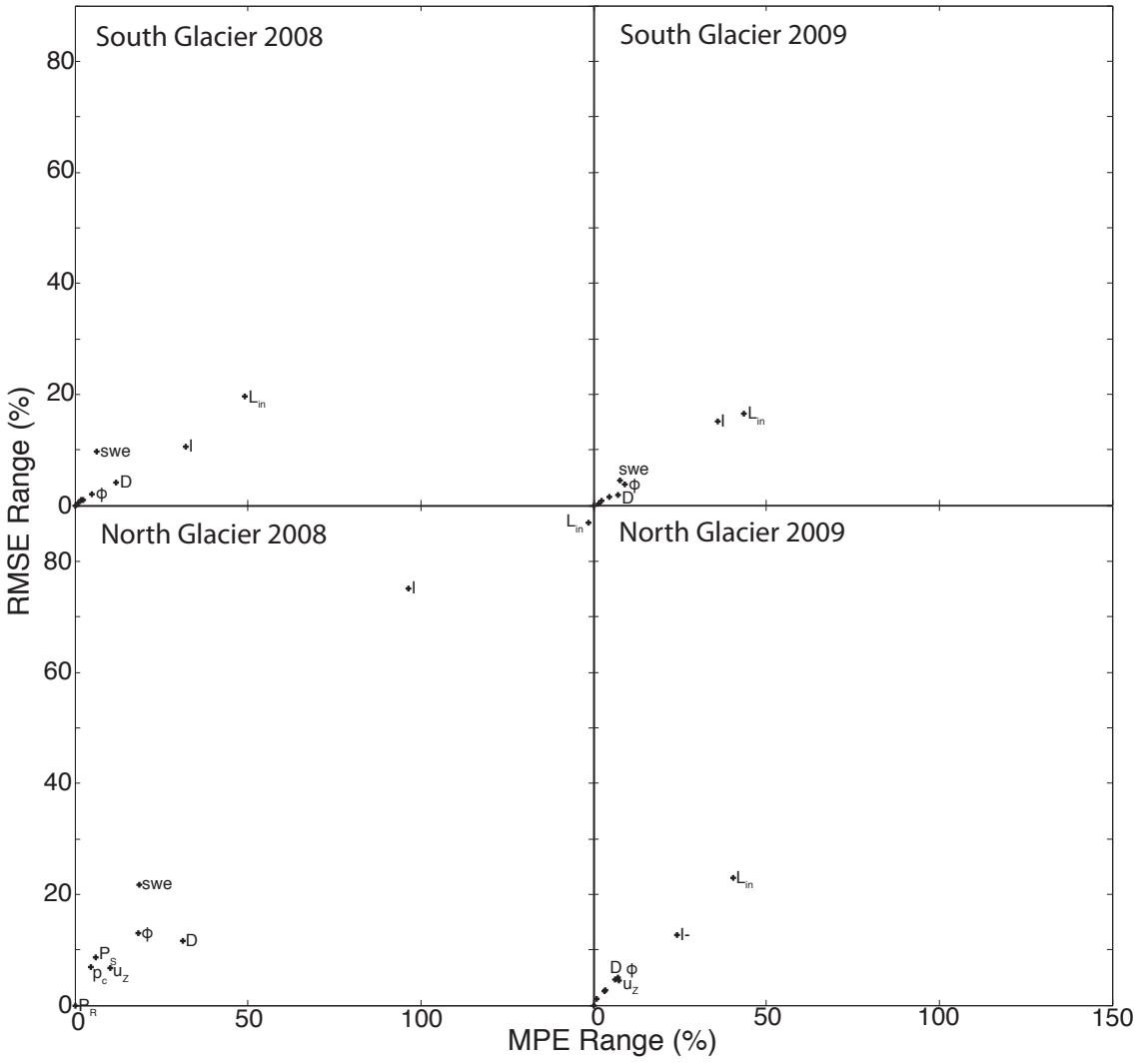

Figure 5.8: Sensitivity ranges for a $\pm 10\,\%$ perturbation in meteorological variables and initial snow-depth displayed in MPE vs. RMSE. Each panel is one simulation. Temperature is not shown as its sensitivity range is much greater than the other variables.

5.3 Summary

There are two important results from these sensitivity tests that are relevant to the transferability experiments. The first is that model sensitivity to parameters is dominated by the albedo parameters. Therefore the ability or inability of the model to transfer in space and time will depend on the similarity in albedo parameters between the various simulations, especially α_i, a_1, a_2 and $\alpha_{s\,lim}$. The second important result is that the model is very sensitive to variations in wind speed and initial snow-depth which are highly variable in space especially in complex glacierized topography (In contrast to incoming longwave radiation). Systematic differences in local wind speed and initial snow-depth may limit the transferability of the DEBM meteorological variables.

Chapter 6

Transferability Experiments

6.1 Introduction

Distributed energy balance melt models (DEBMs) require a large number of inputs and parameters that are observed on only a small number of well studied glaciers (Hock, 2005). For this reason simple (enhanced temperature index) models or similar approaches tend to be used for the modelling of glacier melt at the regional or global scale (e.g. Raper and Braithwaite, 2006, de Woul and Hock, 2005, Hock, 2003, Oerlemans et al., 2005), despite the high probability of these models breaking down under significantly altered climate conditions (Hock et al., 2007). To overcome this deficiency of empirical modelling ways must be found to extend physically based melt models over large spatial domains. Here we take the first steps toward this goal by assessing the transferability of a DEBM over the scale of a small subarctic mountain range.

Data required to run the DEBM were collected from the two Donjek Range study glaciers in the summers of 2008 and 2009, creating four data sets of meteorological variables and parameter values. For full details of how each parameter is derived see *Modelling Methods*. For details of how meteorological variable were collected see *Field Measurements and Data Processing*. Table 6.1 and 6.2 displays the parameter values for each data set.

Model transferability is the ability of a model calibrated for one time and location to produce realistic results at another time and/or location. I describe transferability here both in terms of model parameter values and meteorological driving variables. The former

is the ability of parameters calibrated for one time or location to describe another, while the latter is the ability of meteorological variables measured at one site to force a model at another site. Ideally, a model will have both high parameter transferability and high driving transferability, such that a model calibrated at one well-studied site can be used successfully at surrounding sites.

A series of experiments were carried out to assess the transferability of the DEBM. Each experiment consists of four tests, one for each data set. The DEBM was run with locally derived parameters and locally measured meteorological variables to establish a control from which the transferability experiments can be compared (see *Model Validation*). To gauge transferability in space the parameters from South Glacier 2008 were used in North Glacier 2008, parameters from South Glacier 2009 were used in North Glacier 2009 and vice-versa. To gauge transferability in time the parameters from South Glacier 2008 were used in South Glacier 2009, parameters from North Glacier 2008 used in North Glacier 2009 and vice-versa. To examine the robustness of the transferability in both time and space the parameters from South Glacier 2008 were used in North Glacier 2009, the parameters from South Glacier 2009 used in North Glacier 2008 and vice-versa (Figure 6.1).

Transferring meteorological variables is desirable as there are typically only a small number of meteorological stations in any glacierized region, but it is often necessary to model mass balance over the entire region. Transferring meteorological variables in time is illogical, therefore meteorological variables are transferred only in space in the meteorological transfer experiment. The meteorological variables from South Glacier 2008 replace those in North Glacier 2008, the variables from South Glacier 2009 replace those in North Glacier 2009 and vice-versa (Figure 6.2). Transferring both meteorological variables and parameters follows the same pattern as transferring meteorological variables (Figure 6.3). Additional experiments were carried out wherein ice albedo, initial snow-depth and summer snowfall were independently retained from their data sets while all of the other parameters and/or meteorological variables were transfered. These experiments establish which parameter and meteorological variables dominate errors generated in the transferability experiments and which quantities ought to be determined individually for each glacier in a region.

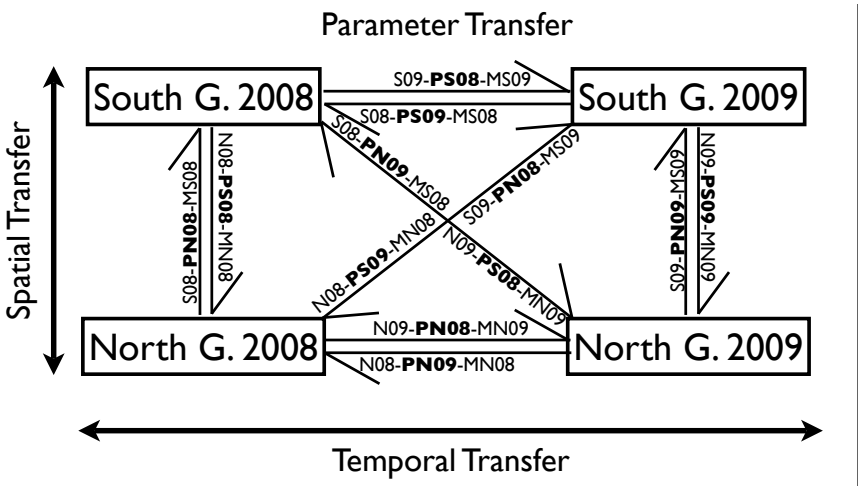

Figure 6.1: Diagram of parameter transfer tests. Parameters can be transfered both spatially and temporally resulting in 12 possible combinations of glacier sites, years and parameter-sets. Tests are labelled with unique codes where, "P" indicated parameters, "M" indicated meteorological forcing, "S" indicates South Glacier, "N" indicates North Glacier and years are represented by their last two digits. Quantities that have been transfered are bolded. For example the code S08-**PN08**-**MS08** represents the experiment simulating South Glacier 2008 using parameter values derived on North Glacier 2008 forced with meteorological variables measured on South Glacier 2008.

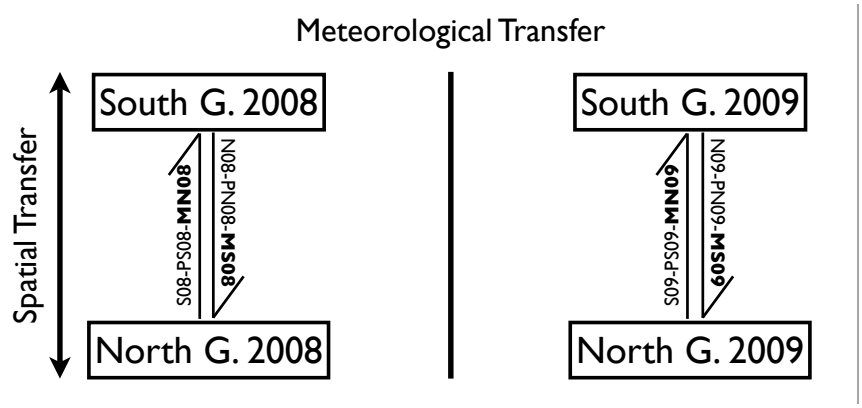

Figure 6.2: Diagram of meteorological variable transfer experiments. Meteorological variables can be transfered only in space resulting in four possible combinations of glacier sites and variables.

Due to the large number of tests carried out (10 experiments which consisted of 4 tests each), the test are assigned unique identification codes. The first three digits of the code denote which glacier and year are being simulated (e.g. S08 for South Glacier 2008 or N09 for North Glacier 2009). After a dash there is the letter "P" that stands for "parameters" and another three digits that show where the parameters originate (e.g. S08-**PN09** would mean South Glacier 2008 simulated using the parameters of North Glacier 2009). After a second dash there is the letter "M" that stands for "meteorological variables" and another three digits that show where the meteorological variable were measured (e.g. S09-**PN09**-**MN09** means South Glacier 2009 simulated using parameters from North Glacier 2009 and meteorological variables from North Glacier 2009). For the experiments where some of the parameters or meteorological variables are not transfered, these variables or parameters are placed in brackets in front of the rest of the test's name (e.g. (α_i,*swe*,P_s)N08-**PS08**-**MS08** means North Glacier 2008 simulated with parameters from South Glacier 2008 except ice albedo, and forced with meteorological variables measured on South Glacier 2008 except initial snow-depth and snowfall rate). Quantities that have been transfered are bolded.

Similar to the control runs (see *Model Validation*) error is quantified using two statistics, Mean Percentage Error (MPE), a measure of model bias,

$$MPE = \frac{\sum_{i=1}^{n}(M_{si} - M_{mi})}{n\overline{M_m}} \times 100\,\%, \tag{6.1}$$

and Root Mean Square Error (RMSE), a measure model precision,

$$RMSE_p = \frac{\sqrt{\sum_{i=1}^{n}(M_{si} - M_{mi})^2}}{\sqrt{n}\overline{M_m}} \times 100\,\%, \tag{6.2}$$

$$RMSE_a = \frac{\sqrt{\sum_{i=1}^{n}(M_{si} - M_{mi})^2}}{\sqrt{n}}, \tag{6.3}$$

where M_{si} is the simulated melt in grid point i, M_{mi} is the measured melt at the stake located in the grid point i, $\overline{M_m}$ is the mean of the measured melt and n is the number of ablation stakes surveyed. For assessing model transferability I found it useful to compute RMSE both as a relative error $RMSE_p$ expressed in percent (%) and as an absolute error $RMSE_a$ expresses in water equivalent meters (w.e. m).

Table 6.1: Model parameters that are taken as invariant for both glaciers and all years. Superscripts indicate where parameter values are taken from unless derived for this study: [p] Paterson (1994), [a] Anslow et al. (2008).

Parameter	Value	Description	Units
α_{ter}	0.21	Albedo of surrounding terrain	
$^{a}\varepsilon_{ter}$	0.95	Emissivity of surrounding terrain	
$^{p}\rho_{i}$	900	Density of ice	$kg\,m^{-3}$
T_{sub}	-30	Minimum subsurface temperature	°C
h	0.10	Thickness of subsurface	m
$^{p}\alpha_{o}$	0.85	Initial albedo of snow	
$^{p}\alpha_{slim}$	0.66	Lower limit of snow albedo	
$^{p}\alpha_{flim}$	0.56	Lower limit of firn albedo	
$^{p}\alpha_{stof}$	0.03	Albedo snow–firn transition	
Z_{thr}	0.01	Fresh snow depth threshold	m
b_1	0.91	Rate constant	mm
b_2	1.36	Rate constant	°C
b_3	0.054	Rate constant	°C
b_4	2.3	Rate constant	mm

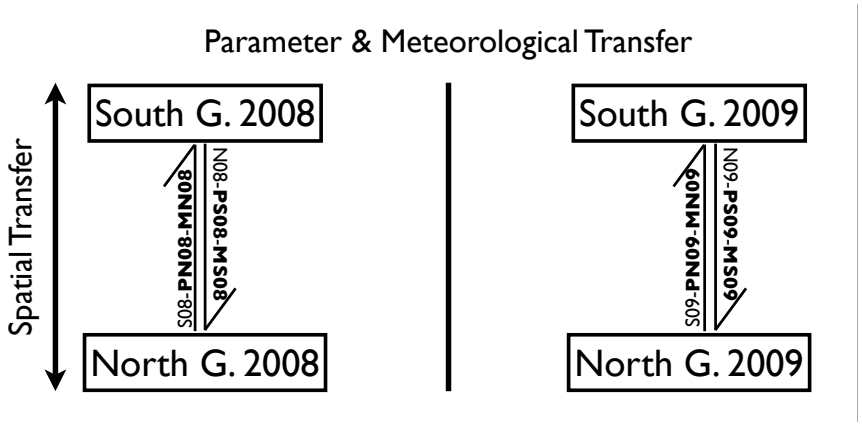

Figure 6.3: Diagram of parameter and meteorological variable transfer experiments. Meteorological variables can be transfered only in space resulting in four possible combinations of glacier sites, variables and parameters.

Table 6.2: Site- or time-specific model parameters. All parameter values where derived for this study. S08 is South Glacier 2008, S09 is South Glacier 2009, N08 is North Glacier 2008 and N09 is North Glacier 2009.

Parameter	S08	S09	N08	N09	Description	Units
ρ_s	293	346	265	264	Density of snow	$\mathrm{kg\,m^{-3}}$
E_f	2450	2450	2400	2480	Firn line elevation	
$\frac{d\alpha_i}{dZ}$	0.11	0.11	0	0	Change α_i with elevation	$(100\,\mathrm{m})^{-1}$
a_1	0.032	0.031	0.042	0.030	Albedo rate constant	$\ln(^\circ\mathrm{C})^{-1}$
a_2	-1.54	-1.68	-1.71	-1.61	Albedo time constant	$\mathrm{day}^{-\frac{1}{2}}$
a_3	0.0074	0.0112	0.0104	0.0142	Albedo rate constant	
a_4	44	30	88	60	Albedo rate constant	$\mathrm{hr\,m^{-1}}$
α_i	0.34	0.33	0.44	0.43	Ice Albedo	
$\alpha_{i\,lim}$	0.16	0.16	0.27	0.27	Lower limit of ice albedo	
z_{oi}	0.65	0.65	0.20	0.20	Roughness length of ice	mm
Γ_T	-6.0	-6.0	-5.3	-5.3	Temperature lapse rate	$\mathrm{K\,km^{-1}}$
Γ_p	2.3	2.3	1.2	1.2	Precipitation lapse rate	$\mathrm{mm\,km^{-1}}$

6.2 Parameter transferability in time

Results of the four tests in which parameter values are transferred in time (TP experiment), that is the parameters from the 2008 data set are used on the same glacier for 2009 and vice-versa, are compared to the validation data in Figures 6.4– 6.5 and Table 6.3. The comparison between the measured and simulated ablation at the stake locations shows that for South Glacier the TP tests are as good or better than the control runs. The North Glacier TP tests are not as similar to the control run as the South Glacier TP tests. The comparison between the USDG record of ablation and the simulated ablation at the AWS demonstrates a different pattern. For South Glacier 2008 the TP test systematically underestimates ablation as compared to both the USDG record and the control run. For South Glacier 2009 the TP test closely track the USDG record at the beginning and end of the summer but over estimates ablation during the mid-summer season. For North Glacier 2008 the TP test predicts more ablation than the USDG record and slightly overestimates ablation compared to the control simulation. For North Glacier 2009 the TP test closely tracks the control simulation, underestimating ablation at the beginning and end of the season and over estimating ablation during mid-summer.

Table 6.3: Difference between simulated and measured ablation at stake locations for the temporal parameter transfer tests.

Simulation	MPE (%)	$RMSE_p$ (%)	$RMSE_a$ (m)
S08-**PS09**-MS08	−11	23	0.30
S09-**PS08**-MS09	−9	13	0.13
N08-**PN09**-MN08	22	40	0.14
N09-**PN08**-MN09	−14	20	0.25

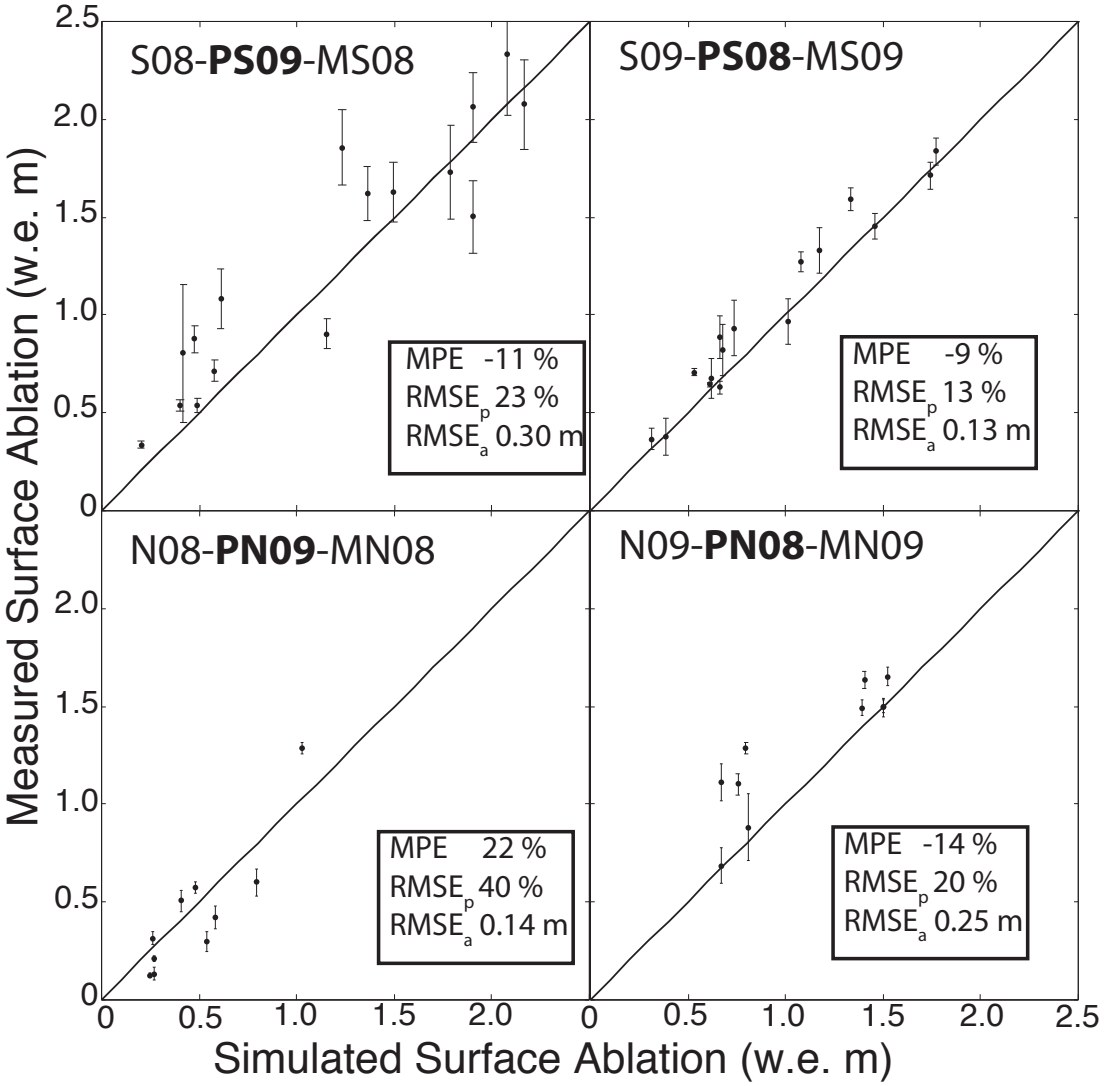

Figure 6.4: Comparison of the results of temporal parameter transfer tests to ablation stake measurements. Notice that the South Glacier errors are close to those for the control runs and that the North Glacier errors are larger than those for those found in the control runs.

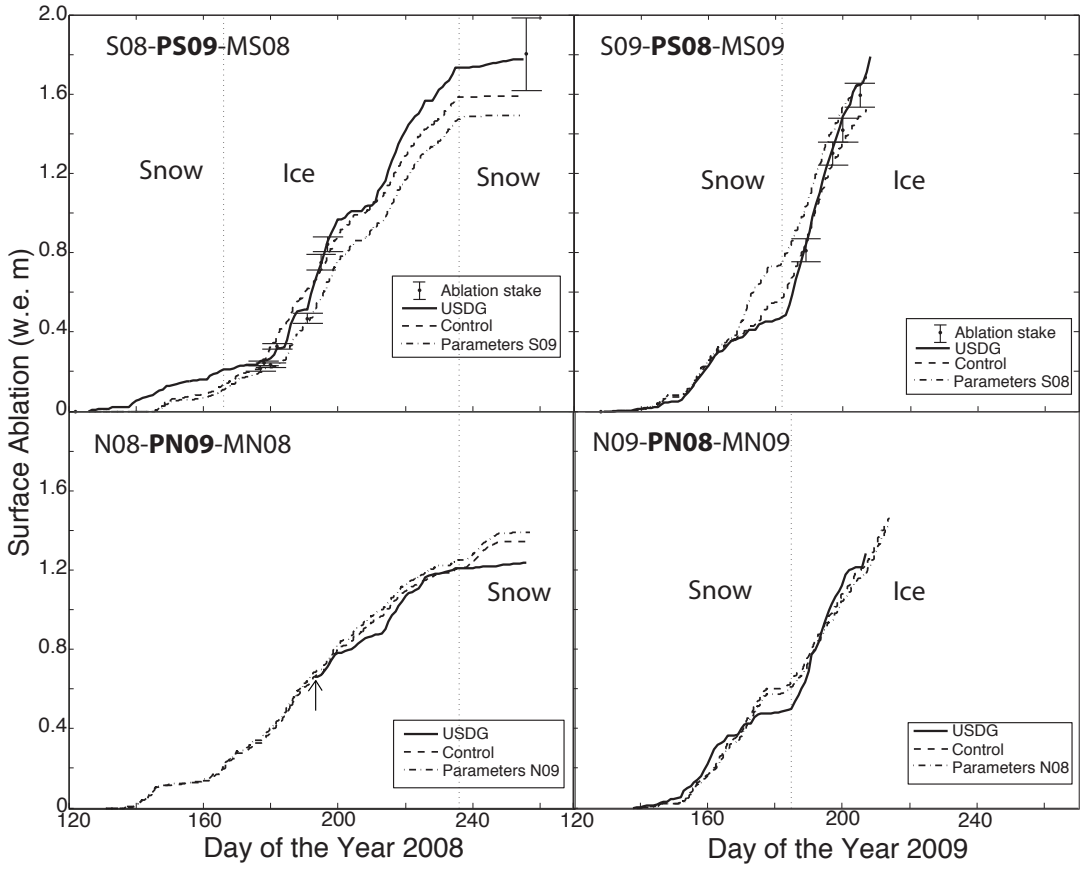

Figure 6.5: Comparison of USDG record of ablation and modelled ablation for the temporal parameter transfer experiment. Control runs are also shown for comparison. For South Glacier ablation stake measurements from near the USDG are also shown. Dotted vertical lines delineate snow–ice transitions. Arrow indicates when the USDG on North Glacier began functioning in 2008.

The TP experiment is compared to the control runs in Figure 6.6 – 6.5 and Table 6.4 – 6.6. These results demonstrate that transferring parameters in time for South Glacier produces only small changes in simulated ablation. This is seen by the dominance of near-zero difference in ablation across South Glacier (Figure 6.6). The RMSE between the control runs and TP experiment is under 10 % (Table 6.4) which confirms the spatial similarity in calculated ablation between the control and TP experiment. Similarly the difference between the control runs and TP experiment is small for mass balance and energy balance components. The result for North Glacier is more complicated (Figure 6.6). The North Glacier 2008 TP test exhibits a patchy pattern of overestimation and underestimation except in the high accumulation zone. The North Glacier 2009 TP test has a more uniform pattern with a zone of overestimated ablation mid-glacier. The patchiness of the North Glacier 2008 simulation results in a higher relative (absolute) RMSE of 35 % (0.16m) while the RMSE for North Glacier 2009 is similar to that of the South Glacier simulations. The differences with respect to the control run in energy balance components is larger than that for South Glacier, but these difference cancel such that the differences in melt energy are $1.2\,\mathrm{W\,m^{-2}}$ and $-2.3\,\mathrm{W\,m^{-2}}$ for 2008 and 2009 respectively (Table 6.6). The difference in mass balance is 4 cm for both years (Table 6.5).

Table 6.4: Difference between the spatially distributed ablation for the temporal parameter transfer experiment and the control runs expressed as MPE and RMSE.

Simulation	MPE (%)	$\mathrm{RMSE_p}$ (%)	$\mathrm{RMSE_a}$ (m)
S08-**PS09**-MS08	−3	9	0.07
S09-**PS08**-MS09	3	5	0.04
N08-**PN09**-MN08	8	35	0.16
N09-**PN08**-MN09	−5	7	0.06

Overall, transferring parameters in time produces relatively small changes in the simulation of energy and mass balance for both glaciers. This indicates that it may be possible to run the simulations for many years before parameters would have to be changed, although a longer record of parameter values is needed to validate this hypothesis.

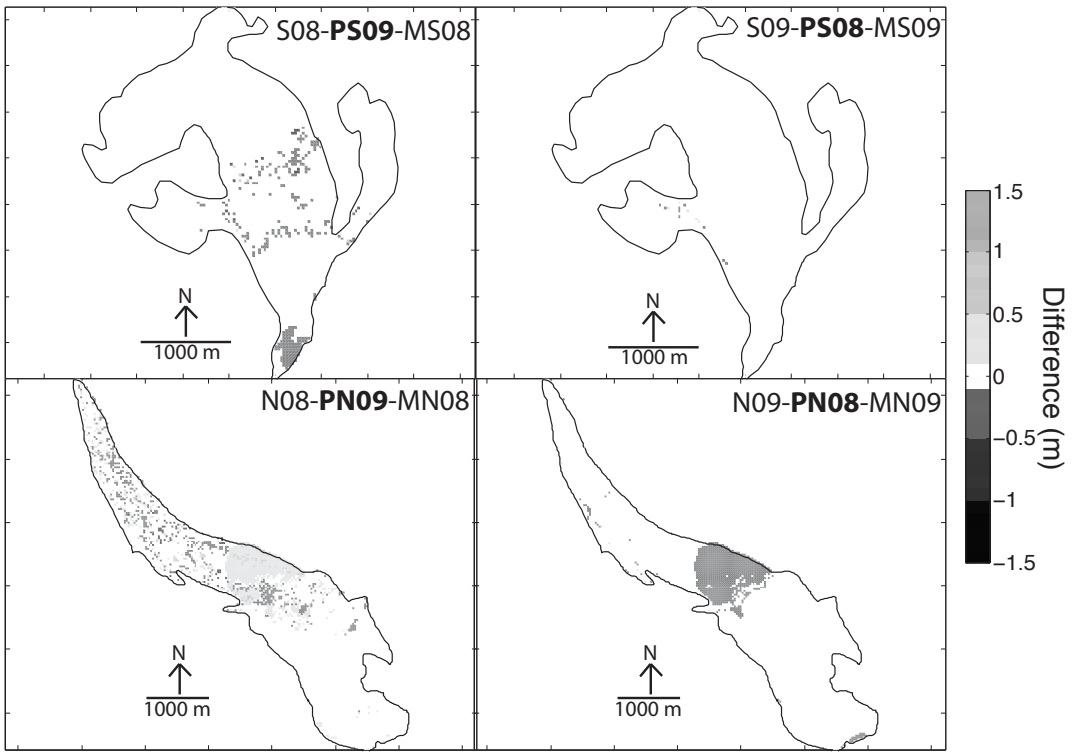

Figure 6.6: Difference in spatially distributed ablation as calculated by the temporal parameter transfer experiment and the spatially distributed ablation in the control runs. Note that white delineates near-zero difference.

Table 6.5: Spatially averaged mass balance components as estimated for the temporal parameter transfer experiments, and difference in summer ablation and mass balance with respect to the control runs. C_{w} is winter surface accumulation, C_{s} is summer surface accumulation, A_{s} is summer surface ablation, B_{n} is surface net balance, $\triangle A_s$ is the difference in summer ablation, and $\triangle B_n$ is the difference in net mass balance with respect to the control run. Units are in w.e. m.

Simulation	C_w	C_s	A_s	B_n	$\triangle A_s$	$\triangle B_n$
S08-**PS09**-MS08	0.33	0.28	−0.77	−0.17	0.02	0.01
S09-**PS08**-MS09	0.53	0.05	−0.84	−0.25	−0.03	−0.02
N08-**PN09**-MN08	0.23	0.17	−0.5	−0.11	−0.04	−0.04
N09-**PN08**-MN09	0.38	0.07	−0.66	−0.21	0.04	0.04

Table 6.6: Difference in spatially averaged energy balance components between temporal parameter transfer experiment and control runs. $\triangle S_{\mathrm{net}}$ is the difference in net shortwave radiation, $\triangle L_{\mathrm{net}}$ is the difference in net longwave radiation, $\triangle Q_{\mathrm{H}}$ is the difference in sensible heat flux, $\triangle Q_{\mathrm{L}}$ is the difference in latent heat flux, $\triangle Q_{\mathrm{g}}$ is the difference in subsurface heat flux, and $\triangle Q_{\mathrm{M}}$ is the difference in the energy available for melt. Units are in $\mathrm{W\,m^{-2}}$

Simulation	$\triangle S_{\mathrm{net}}$	$\triangle L_{\mathrm{net}}$	$\triangle Q_{\mathrm{H}}$	$\triangle Q_{\mathrm{L}}$	$\triangle Q_{\mathrm{g}}$	$\triangle Q_{\mathrm{M}}$
S08-**PS09**-MS08	−0.7	−0.1	−0.1	0.0	0.1	−0.8
S09-**PS08**-MS09	1.4	0.1	0.0	−0.1	0.0	1.4
N08-**PN09**-MN08	3.0	−1.3	−0.1	−0.2	−0.1	1.2
N09-**PN08**-MN09	−3.5	0.7	0.2	0.2	0.0	−2.3

6.3 Parameter transferability in space

Four tests were conducted in which parameters are transfered in space (SP experiment). That is, parameters from North Glacier 2008 are used for South Glacier 2008 and vice versa; parameter from South Glacier 2009 are used for North Glacier 2009 and vice-versa. Results of this experiment is compared to the validation data in Figures 6.7, 6.8 and Table 6.7. The ablation stake comparison (Figure 6.7) shows that by transferring parameters in space much larger errors are generated than in the control runs. The disagreement between the measured and simulated ablation is particularly striking for the North Glacier 2008 test where the relative (absolute) RMSE is 126 % (0.44 m). In general the SP experiment produces smaller errors for the 2009 simulations than the 2008 simulations. The comparison between the simulated and measured ablation at the AWS location shows a similar pattern. The 2008 simulations greatly underestimate ablation compared to both the USDG record and the control runs for the entire length of the simulation for North Glacier and after mid-summer for South Glacier. The South Glacier 2009 SP test closely tracks the control simulation except for a period in mid-summer and is overall close to the USDG record. The North Glacier 2009 SP test also closely tracks the control run at the beginning and end of the simulation but underestimates ablation mid-summer. Overall the SP experiment produces larger errors than either the control runs or the TP experiments, when compared to the validation data.

Table 6.7: Difference between simulated and measured ablation at stake locations for the spatial parameter transfer experiment.

Simulation	MPE(%)	$RMSE_p$ (%)	$RMSE_a$ (m)
S08-**PN08**-MS08	−32	41	0.53
S09-**PN09**-MS09	−14	22	0.22
N08-**PS08**-MN08	55	126	0.44
N09-**PS09**-MN09	11	29	0.37

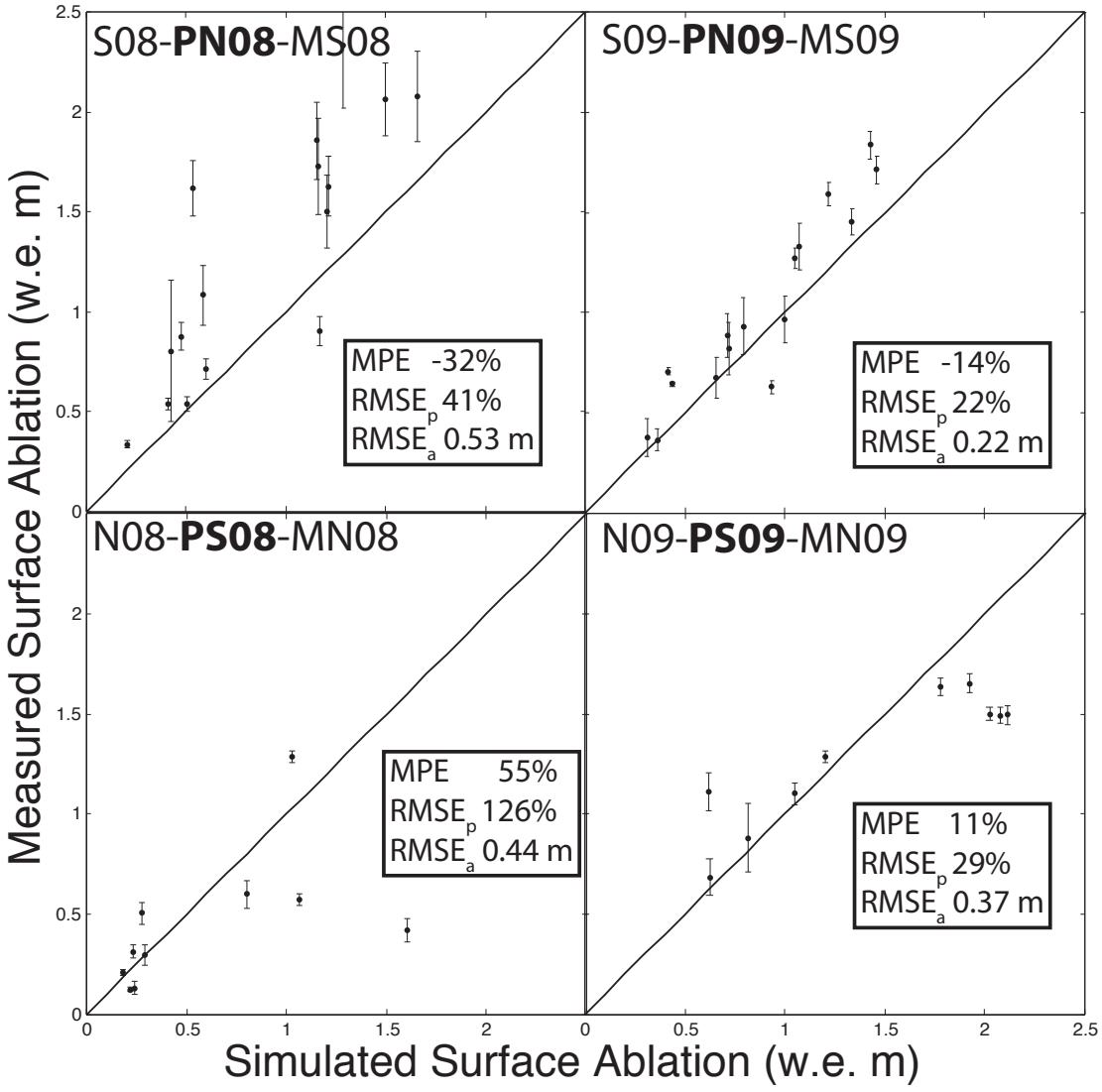

Figure 6.7: Comparison of the results of spatial parameter transfer experiment to ablation stake measurements. Notice that the errors are larger for both glaciers and years than in the control runs, especially for the 2008 simulations.

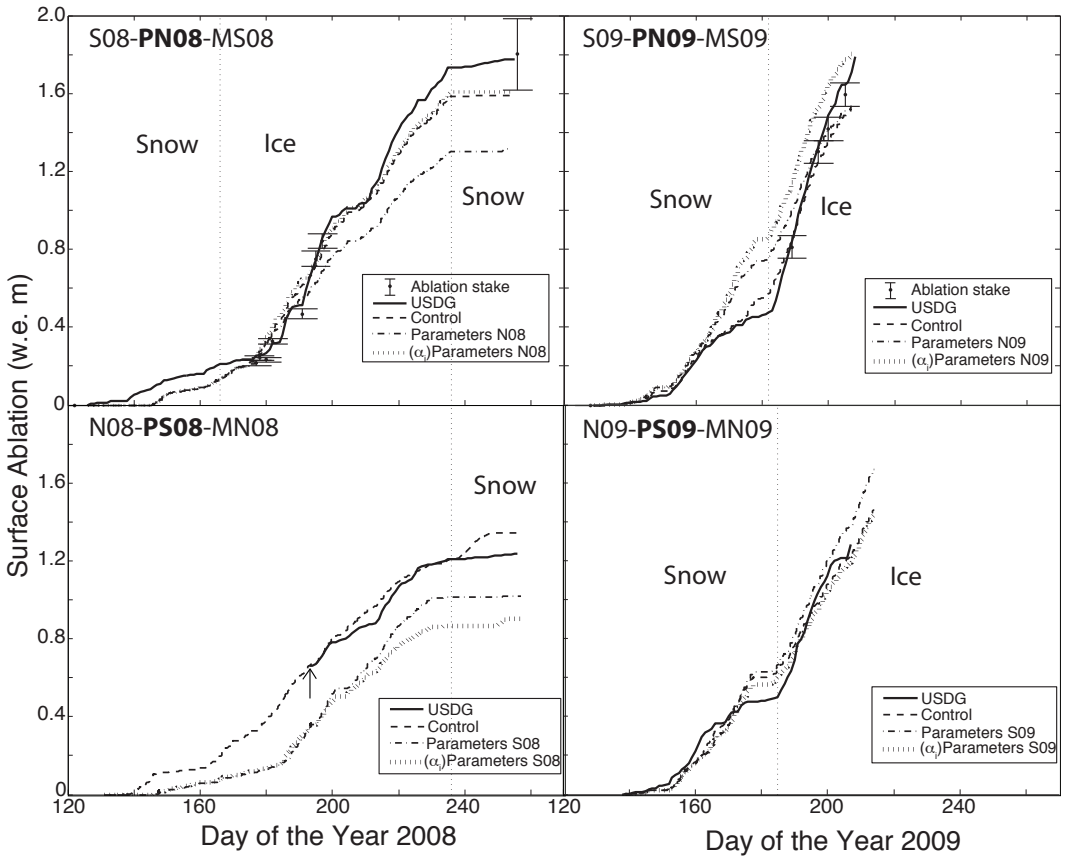

Figure 6.8: Comparison of USDG record of ablation and modelled ablation for the spatial parameter transfer experiment. Control runs are also shown for comparison. For South Glacier ablation stake measurements from near the USDG are also shown. Dotted vertical lines delineate snow–ice transitions. Arrow indicates when the USDG on North Glacier began functioning in 2008.

The SP experiment is compared to the control runs in Figures 6.8, 6.9 and Tables 6.8 – 6.10. The difference in spatially distributed ablation between the control runs and the SP experiment (Figure 6.9) demonstrates that the tests are most dissimilar in the ablation zone of the glaciers and around the ice–firn transition elevation. This is true for both glaciers but the difference is of opposite in sign, with underestimation of ablation on South Glacier and overestimation of ablation on North Glacier relative to the control run. The North Glacier 2008 test shows the patchy pattern characteristic for that data set. The effect on mass balance of spatially transferring the parameters (Table 6.9) ranges from 2–10 cm w.e., over double the effect of transferring parameters in time. The differences in energy balance components between the control runs and the SP experiment shows the largest energy balance difference in net shortwave radiation. This indicates poor transferability of either the snow albedo evolution model or of ice albedo.

Table 6.8: Difference between the spatially distributed ablation for the spatial parameter transfer experiment and the control runs expressed as MPE and RMSE.

Simulation	MPE %	$RMSE_p$ %	$RMSE_a$ m
S08-**PN08**-MS08	−15	34	0.27
S09-**PN09**-MS09	2	19	0.15
N08-**PS08**-MN08	29	76	0.35
N09-**PS09**-MN09	11	25	0.22

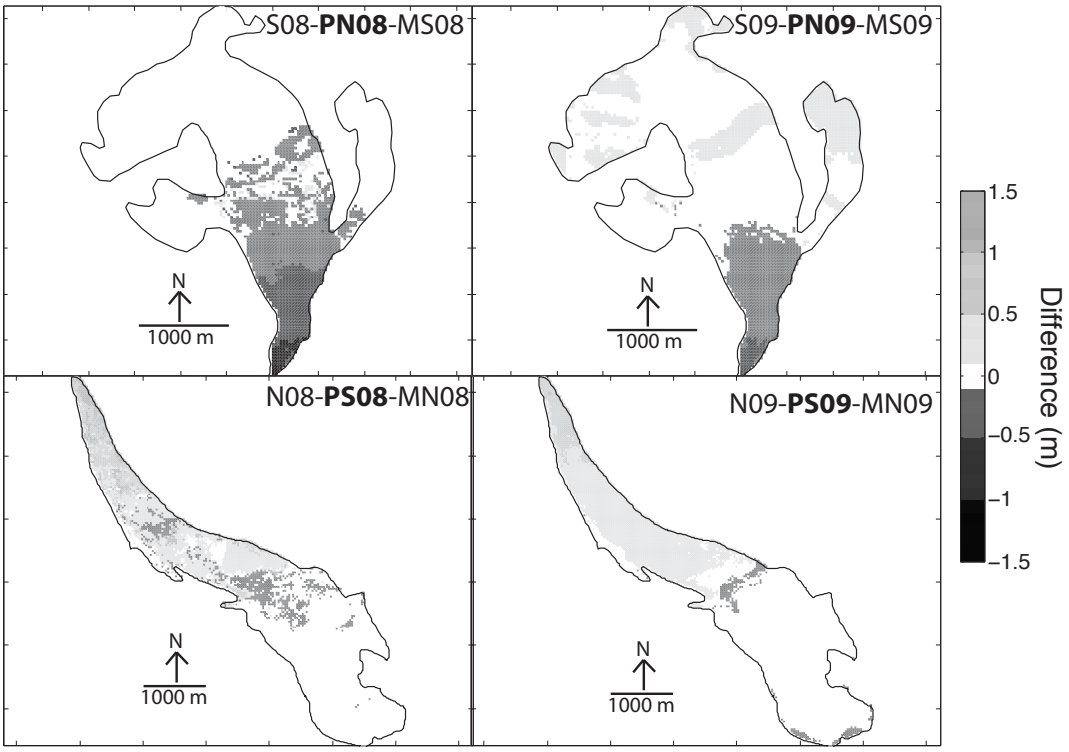

Figure 6.9: Difference in spatially distributed ablation as calculated by the spatial parameter transfer experiment and the spatially distributed ablation in the control runs. Note that white delineates near-zero difference.

Table 6.9: Spatially averaged mass balance components as estimated for the spatial parameter transfer experiments, and the difference in summer ablation and mass balance with respect to the control runs. C_{w} is winter surface accumulation, C_{s} is summer surface accumulation, A_{s} is summer surface ablation, B_{n} is surface net balance, $\triangle A_s$ is the difference in summer ablation, and $\triangle B_n$ is the difference in net mass balance with respect to the control run. Units are in w.e. m.

Simulation	C_w	C_s	A_s	B_n	$\triangle A_s$	$\triangle B_n$
S08-**PN08**-MS08	0.33	0.24	−0.67	−0.11	0.12	0.07
S09-**PN09**-MS09	0.53	0.04	−0.82	−0.25	−0.01	−0.02
N08-**PS08**-MN08	0.23	0.20	−0.60	−0.17	−0.13	−0.10
N09-**PS09**-MN09	0.38	0.08	−0.79	−0.33	−0.09	−0.08

Table 6.10: Difference in spatially averaged energy balance components between spatial parameter transfer experiment and control runs. $\triangle S_{\mathrm{net}}$ is the difference in net shortwave radiation, $\triangle L_{\mathrm{net}}$ is the difference in net longwave radiation, $\triangle Q_{\mathrm{H}}$ is the difference in sensible heat flux, $\triangle Q_{\mathrm{L}}$ is the difference in latent heat flux, $\triangle Q_{\mathrm{g}}$ is the difference in subsurface heat flux, and $\triangle Q_{\mathrm{M}}$ is the difference in the energy available for melt. Units are in $\mathrm{W\,m^{-2}}$

Simulation	$\triangle S_{\mathrm{net}}$	$\triangle L_{\mathrm{net}}$	$\triangle Q_{\mathrm{H}}$	$\triangle Q_{\mathrm{L}}$	$\triangle Q_{\mathrm{g}}$	$\triangle Q_{\mathrm{M}}$
S08-**PN08**-MS08	−4.4	0.2	0.3	0.1	0.1	−3.7
S09-**PN09**-MS09	1.3	−0.5	0	−0.1	0	0.7
N08-**PS08**-MN08	5.1	−0.4	−0.3	−0.3	0	4.2
N09-**PS09**-MN09	5.7	−0.4	0.1	−0.2	0	5.2

6.3.1 Assessing the role of ice albedo

To test whether the poor spatial transferability is a function of the large difference in average ice albedo between the two study sites (0.34 for South Glacier verses 0.44 for North Glacier) the SP experiment was repeated except with each glacier retaining locally measured ice albedo (SP-α_i experiment). The comparison between this experiment and the validation data are shown in Figure 6.8, 6.10 and Table 6.11. The comparison of simulated and measured ablation at the stake locations (Figure 6.10) shows that the RMSEs are larger than in the control runs but smaller than in the full SP experiment. The 2009 RMSEs in particular are close to their values from the control runs. The MPEs from the simulations, except for South Glacier 2008, are smaller than those found in the control runs. The North Glacier 2008 and South Glacier 2009 SP-α_i tests have MPEs of 1 % and -3 % respectively.

The comparison of the SP-α_i experiment to the USDG record shows a different pattern (Figure 6.8). The South Glacier 2008 and North Glacier 2009 SP-α_i tests are close to the control run, while the South Glacier 2009 SP-α_i test overestimates ablation with respect to both the control runs and the USDG record. The North Glacier 2008 SP-α_i test underestimates ablation compared to: the control run, the USDG record, and the full SP test. In general these results demonstrate that using locally derived ice albedo significantly improves the model performance.

Table 6.11: Differences between simulated and measured ablation at stake locations for the spatial parameter transfer experiment, but with locally-measured ice albedo retained.

Simulation	MPE (%)	$RMSE_p$ (%)	$RMSE_a$ (m)
(α_i)S08-**PN08**-MS08	-16	31	0.4
(α_i)S09-**PN09**-MS09	-3	15	0.15
(α_i)N08-**PS08**-MN08	1	35	0.12
(α_i)N09-**PS09**-MN09	-10	16	0.20

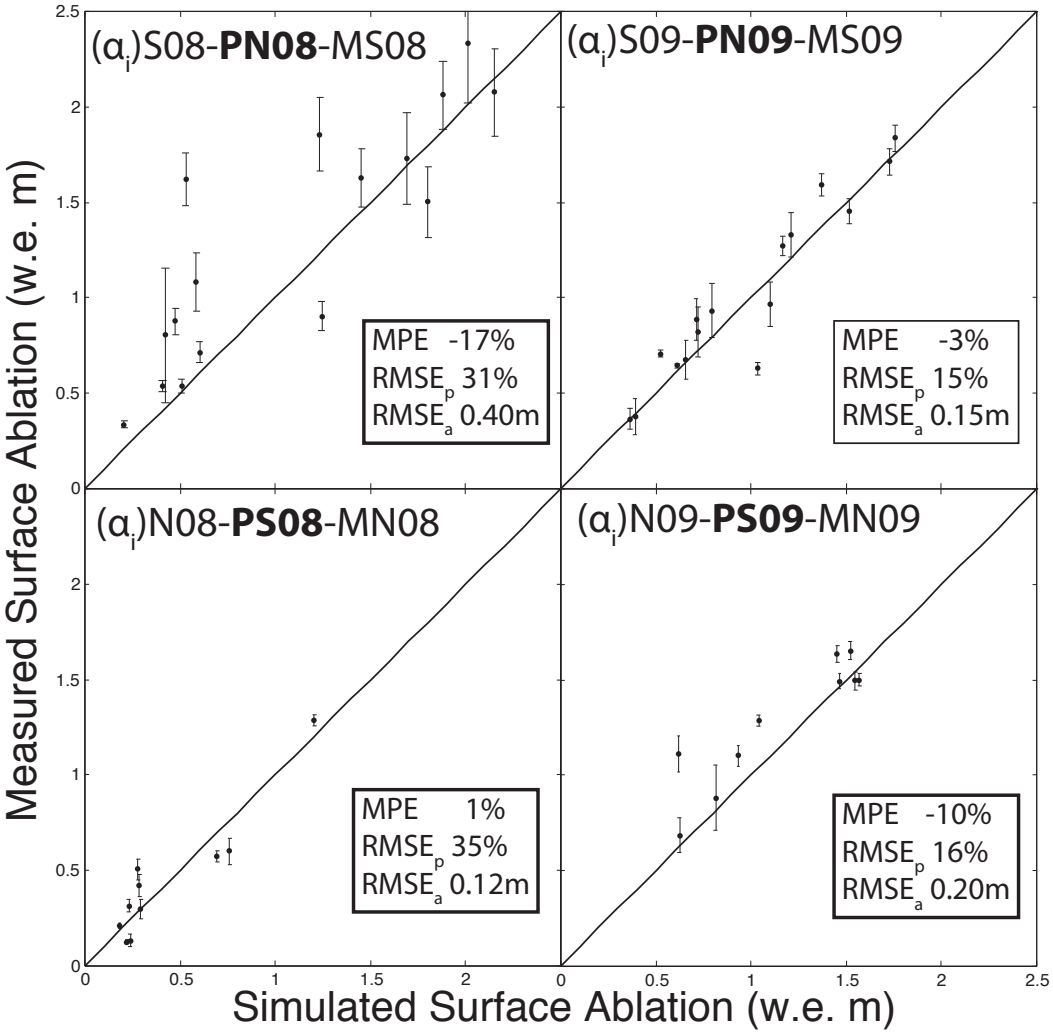

Figure 6.10: Comparison of the results of spatial parameter transfer experiment, but with locally-measured ice albedo retained. Notice that the errors are smaller than those produced when ice albedo was transfered.

The SP-α_i experiment is compared to the control runs in Figures 6.8, 6.11, and Tables 6.12 – 6.14. The differences in spatially distributed ablation demonstrate that most of the difference between these tests and the control runs are concentrated in the ice–firn transition region (Figure 6.11). This makes sense as the firn-line is at a different elevation on each glacier (Table 6.2). North Glacier 2009 shows the least difference from the control run, while North Glacier 2008 maintains its characteristic patchy pattern. South Glacier 2009 has the largest difference in simulated mass balance in these tests, with an additional 10 w.e. cm of ablation (Table 6.13). From Figure 6.11 one can see that this difference is concentrated in the region around the ice–firn transition. The differences in mass balance for the other simulations is smaller, between 1–4 w.e. cm. The differences in energy balance components are dominated by differences net shortwave radiation (Table 6.14).

Table 6.12: Difference between the spatially distributed ablation for the spatial parameter transfer experiment, but with locally-measured ice albedo retained and the control runs expressed as MPE and RMSE.

Simulation	MPE (%)	$RMSE_p$ (%)	$RMSE_a$ (m)
(α_i)S08-**PN08**-MS08	−3	10	0.08
(α_i)S09-**PN09**-MS09	11	15	0.13
(α_i)N08-**PS08**-MN08	5	40	0.18
(α_i)N09-**PS09**-MN09	−3	5	0.05

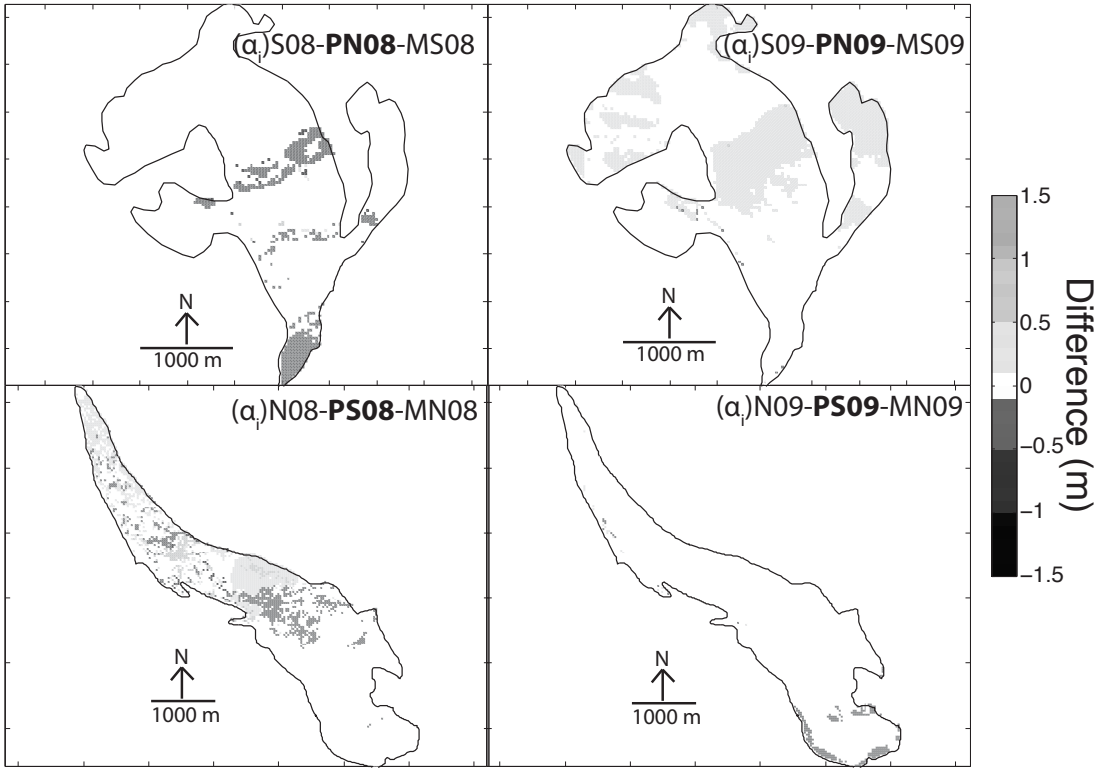

Figure 6.11: Difference in spatially distributed ablation as calculated by the spatial parameter transfer experiment, but with locally-measured ice albedo retained and the spatially distributed ablation in the control runs. Note that white delineates near-zero difference.

Table 6.13: Spatially averaged mass balance components as estimated for the spatial parameter transfer experiment, but with locally-measured ice albedo retained and the difference in summer ablation and mass balance with respect to the control runs. C_{w} is winter surface accumulation, C_{s} is summer surface accumulation, A_{s} is summer surface ablation, B_{n} is surface net balance, $\triangle A_s$ is the difference in summer ablation, and $\triangle B_n$ is the difference in net mass balance with respect to the control run. Units are in w.e. m.

Simulation	C_w	C_s	A_s	B_n	$\triangle A_s$	$\triangle B_n$
(α_{i})S08-**PN08**-MS08	0.33	0.24	−0.77	−0.21	0.02	−0.03
(α_{i})S09-**PN08**-MS09	0.53	0.04	−0.90	−0.33	−0.09	−0.10
(α_{i})N08-**PS08**-MN08	0.23	0.20	−0.49	−0.06	−0.02	0.01
(α_{i})N09-**PS09**-MN09	0.38	0.08	−0.68	−0.21	0.02	0.04

Table 6.14: Difference in spatially averaged energy balance components between spatial parameter transfer experiment, but with locally-measured ice albedo retained and control runs. $\triangle S_{\mathrm{net}}$ is the difference in net shortwave radiation, $\triangle L_{\mathrm{net}}$ is the difference in net longwave radiation, $\triangle Q_{\mathrm{H}}$ is the difference in sensible heat flux, $\triangle Q_{\mathrm{L}}$ is the difference in latent heat flux, $\triangle Q_{\mathrm{g}}$ is the difference in subsurface heat flux, and $\triangle Q_{\mathrm{M}}$ is the difference in the energy available for melt. Units are in W m^{-2}

Simulation	$\triangle S_{\mathrm{net}}$	$\triangle L_{\mathrm{net}}$	$\triangle Q_{\mathrm{H}}$	$\triangle Q_{\mathrm{L}}$	$\triangle Q_{\mathrm{g}}$	$\triangle Q_{\mathrm{M}}$
(α_{i})S08-**PN08**-MS08	−1.1	0.1	0.2	0.1	0.1	−0.6
(α_{i})S09-**PN09**-MS09	5.7	−0.5	0	−0.1	0	5.1
(α_{i})N08-**PS08**-MN08	1.2	0.1	−0.2	−0.3	0	0.8
(α_{i})N09-**PS09**-MN09	−0.9	−0.4	0.1	−0.1	0	−1.3

6.4 Parameter transfer in both space and time

For completeness, an experiment was carried out in which parameter values were transfered in both space and time (STP experiment). That is, the parameters from South Glacier 2008 were used for North Glacier 2009 and vice versa; the parameters from North Glacier 2008 were used for South Glacier 2009 and vice-versa. The comparison between the results of this experiment and the control runs are shown in Figures 6.12, 6.13, and Table 6.15. The comparison of the simulated and measured ablation at the stake locations shows that the STP experiment produced larger RMSE and MPE than the control runs, but in a more consistent fashion than the SP experiment, with larger errors for both years and glaciers (Figure 6.12). The comparison of the simulated ablation at the AWS location to the USDG record also shows a more consistent pattern than the SP experiment (Figure 6.13). Both 2008 tests underestimate ablation at the AWS location with respect to both the USDG record and control runs. The South Glacier 2008 STP test tracks the control run closely until mid-summer, while the North Glacier 2008 STP test consistently underestimates ablation throughout the summer. The South Glacier 2009 STP test agrees closely with the control run at the beginning and end of the summer, but overestimates ablation for the middle part of simulation. The North Glacier 2009 STP test tracks the control run closely until midway though the simulation when it diverges and overestimates ablation.

Table 6.15: Differences between simulated and measured ablation at stake locations for the spatial-temporal parameter transfer experiment.

Simulation	MPE(%)	$RMSE_p$ (%)	$RMSE_a$ (m)
S08-**PN09**-MS08	−25	36	0.46
S09-**PN08**-MS09	−21	25	0.26
N08-**PS09**-MN08	24	39	0.14
N09-**PS08**-MN09	11	29	0.37

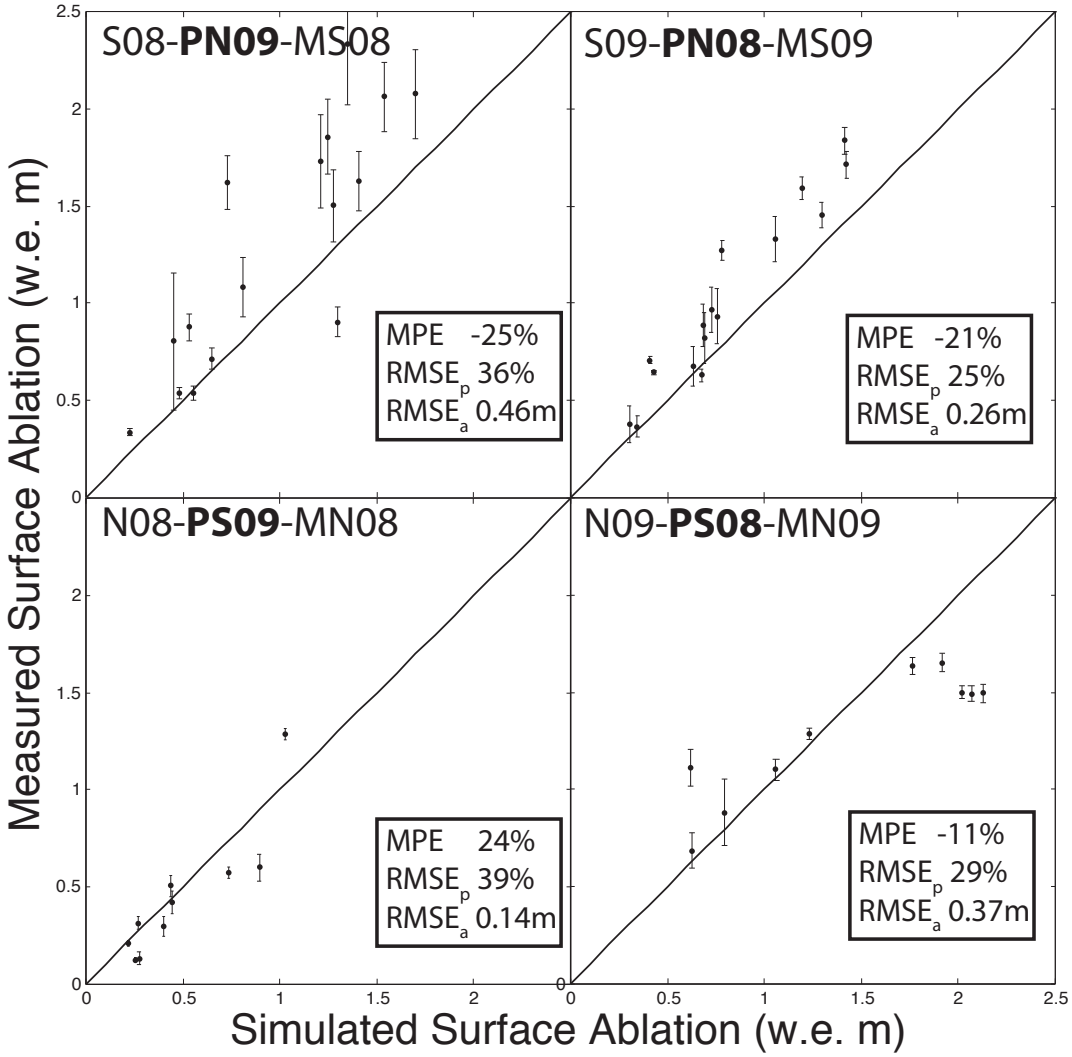

Figure 6.12: Comparison of results of the spatial-temporal parameter transfer experiment to ablation stake measurements.

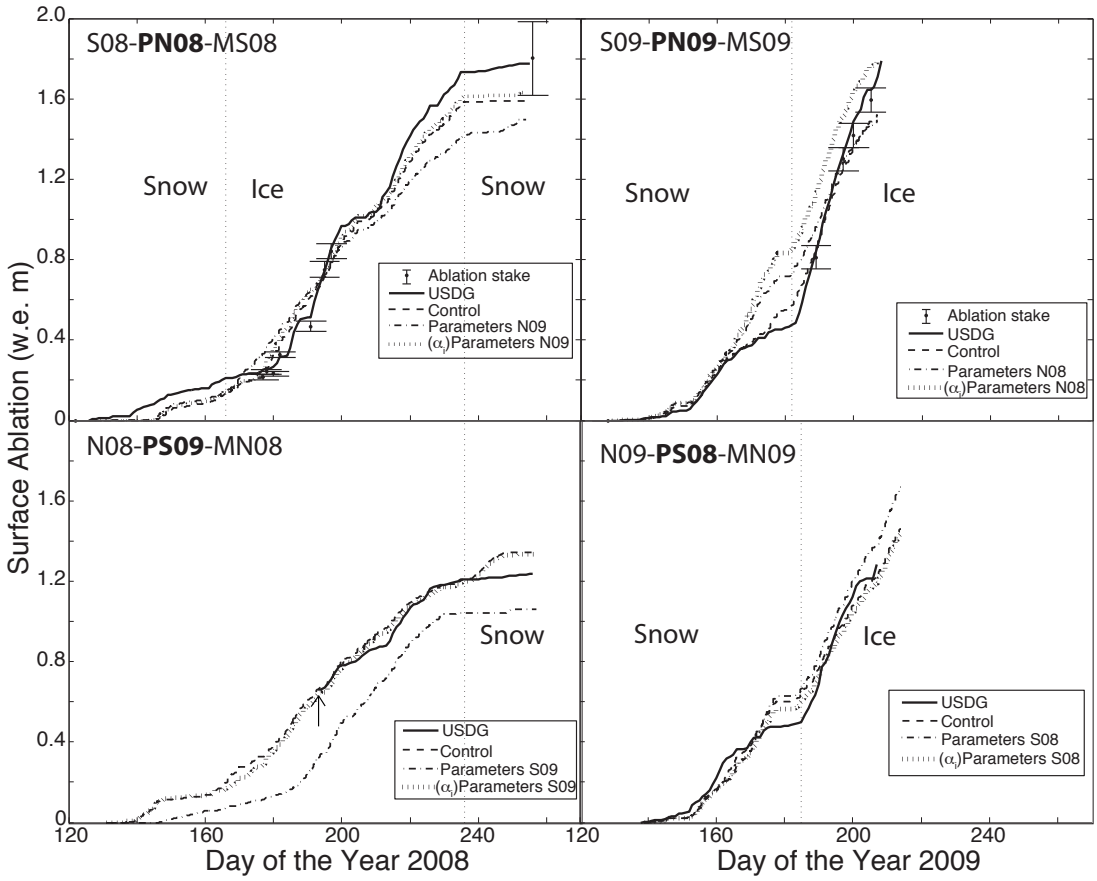

Figure 6.13: Comparison of USDG record of ablation and modelled ablation for the spatial-temporal parameter transfer experiment. Control runs are also shown for comparison. For South Glacier ablation stake measurements from near the USDG are also shown. Dotted vertical lines delineate snow–ice transitions. Arrow indicates when the USDG on North Glacier began functioning in 2008.

Results of the STP experiment are compared to the control runs in Figures 6.13, 6.14 and Tables 6.16 – 6.18. The difference in spatially distributed ablation between the STP experiment and the control runs (Figure 6.14) show the same general patterns as the SP experiment. That is, underestimation of ablation in the ablation zones of South Glacier, overestimation of ablation in the ablation zones of North Glacier, large differences near the ice–firn transition area on both glaciers and a patchy pattern on North Glacier in 2008. The absolute differences in mass balance between the STP experiment and the control runs range from 0–10 w.e. cm (Table 6.17), which places the mass balance errors in the same range as those for the SP experiment. The zero difference in mass balance for South Glacier 2008 is a surprising result considering how different this experiment is from the control run. However, examining Table 6.17 indicates that the zero difference results from a reduction in summer snowfall canceling a reduction in ablation. The differences in energy balance components (Table 6.18) indicates that like the other parameter transfer experiments, the differences for the STP experiment are dominated by net shortwave radiation. The exception is South Glacier 2008 where the difference in net shortwave radiation is zero; instead the difference in this simulation is dominated by net longwave radiation.

In general the STP experiment produces similar errors to those found in the SP experiment. This indicates that parameters derived on one glacier might be able to be used on another for several years without magnifying errors in estimated mass balance.

Table 6.16: Difference between the spatially distributed ablation for the spatial-temporal parameter transfer experiment and the control runs expressed as MPE and RMSE.

Simulation	MPE (%)	$RMSE_p$ (%)	$RMSE_a$ (m)
S08-**PN09**-MS08	−6	32	0.25
S09-**PN08**-MS09	−6	19	0.15
N08-**PS09**-MN08	35	74	0.34
N09-**PS08**-MN09	11	25	0.22

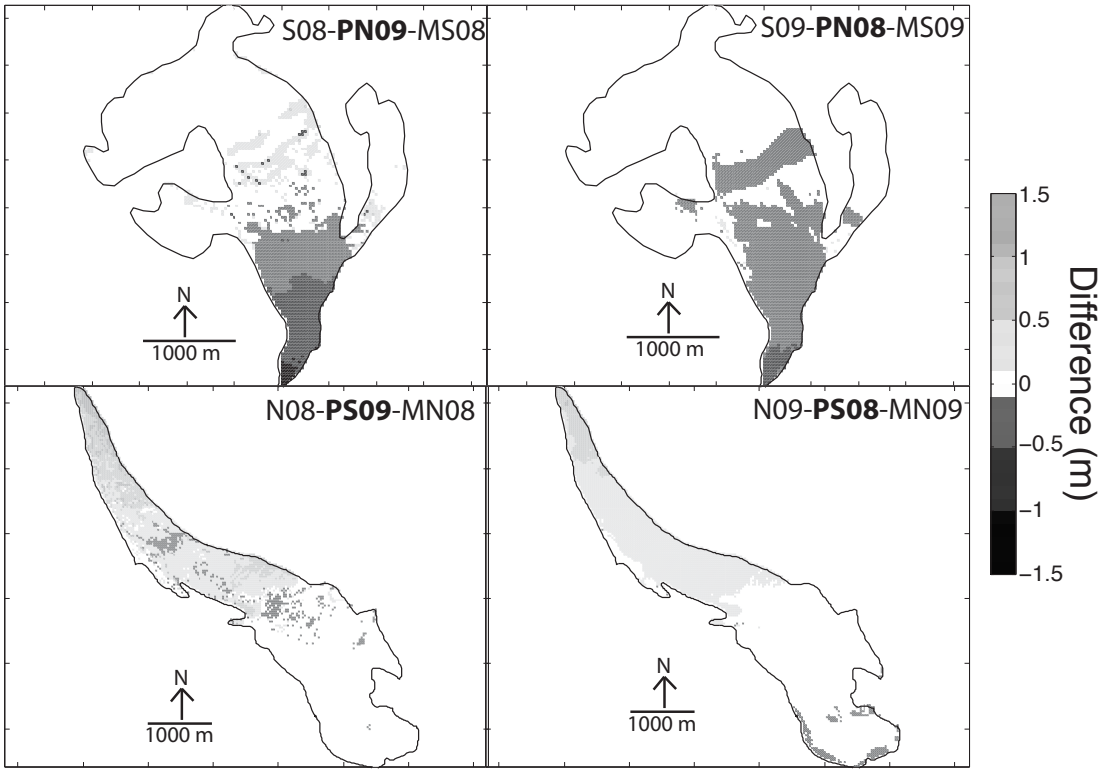

Figure 6.14: Difference in spatially distributed ablation as calculated by the spatial-temporal parameter transfer experiment and the spatially distributed ablation in the control runs. Note that white delineates near-zero difference.

Table 6.17: Spatially averaged mass balance components as estimated for the spatial-temporal parameter transfer experiment, and the difference in summer ablation and mass balance with respect to the control runs. C_{w} is winter surface accumulation, C_{s} is summer surface accumulation, A_{s} is summer surface ablation, B_{n} is surface net balance, $\triangle A_s$ is the difference in summer ablation, and $\triangle B_n$ is the difference in net mass balance with respect to the control run. Units are in w.e. m.

Simulation	C_w	C_s	A_s	B_n	$\triangle A_s$	$\triangle B_n$
S08-**PN09**-MS08	0.33	0.24	−0.74	−0.18	0.05	0
S09-**PN08**-MS09	0.53	0.04	−0.76	−0.19	0.05	0.04
N08-**PS09**-MN08	0.23	0.20	−0.63	−0.17	−0.13	−0.10
N09-**PS08**-MN09	0.38	0.08	−0.79	−0.33	−0.09	−0.08

Table 6.18: Difference in spatially averaged energy balance components between spatial-temporal parameter transfer experiment and control runs. $\triangle S_{\mathrm{net}}$ is the difference in net shortwave radiation, $\triangle L_{\mathrm{net}}$ is the difference in net longwave radiation, $\triangle Q_{\mathrm{H}}$ is the difference in sensible heat flux, $\triangle Q_{\mathrm{L}}$ is the difference in latent heat flux, $\triangle Q_{\mathrm{g}}$ is the difference in subsurface heat flux, and $\triangle Q_{\mathrm{M}}$ is the difference in the energy available for melt. Units are in $\mathrm{W\,m^{-2}}$

Simulation	$\triangle S_{\mathrm{net}}$	$\triangle L_{\mathrm{net}}$	$\triangle Q_{\mathrm{H}}$	$\triangle Q_{\mathrm{L}}$	$\triangle Q_{\mathrm{g}}$	$\triangle Q_{\mathrm{M}}$
S08-**PN09**-MS08	0	−1.5	−0.1	−0.1	0.2	−1.5
S09-**PN08**-MS09	−3.2	0.2	0.1	0.2	0	−2.8
N08-**PS09**-MN08	8.1	−2	−0.5	−0.6	0	5.1
N09-**PS08**-MN09	5.0	0.1	0.2	−0.1	0	5.3

6.4.1 Assessing the role of ice albedo

Much as in the SP experiment the difference in the ice albedo between the two study sites is an obvious potential source of error. To examine this, an experiment was carried out identical to the STP experiment except that locally measured ice albedo is retained (STP$-\alpha_i$ experiment). The comparison between this experiment and the control runs is shown in Figures 6.13, 6.15 and Table 6.19. The comparison between the ablation at the stake locations for the STP$-\alpha_i$ experiment and the measured ablation at the stakes shows that the errors created are larger than those for the control runs but smaller than those created by the STP experiment (Figure 6.15). The relative (absolute) RMSE ranges from 16–33 % (0.11–0.33 m) with the North Glacier 2008 test producing the largest relative error and the South Glacier 2008 test producing the largest absolute error (Table 6.19). Comparing the simulated ablation at the AWS location to the USDG record shows that in three of the tests the simulated ablation closely tracks that in the control runs. The exception is the South Glacier 2009 STP$-\alpha_i$ test where simulated ablation is overestimated relative to both the control run and the USDG record after 14th June 2009 (day 165) (Figure 6.13).

Table 6.19: Differences between simulated and measured ablation at stake locations for the spatial-temporal parameter transfer experiment, but with locally-measured ice albedo retained.

Simulation	MPE (%)	$RMSE_p$ (%)	$RMSE_a$ (m)
(α_i)S08-**PN09**-MS08	−11	26	0.33
(α_i)S09-**PN08**-MS09	−12	18	0.18
(α_i)N08-**PS09**-MN08	22	33	0.11
(α_i)N09-**PS08**-MN09	−11	16	0.20

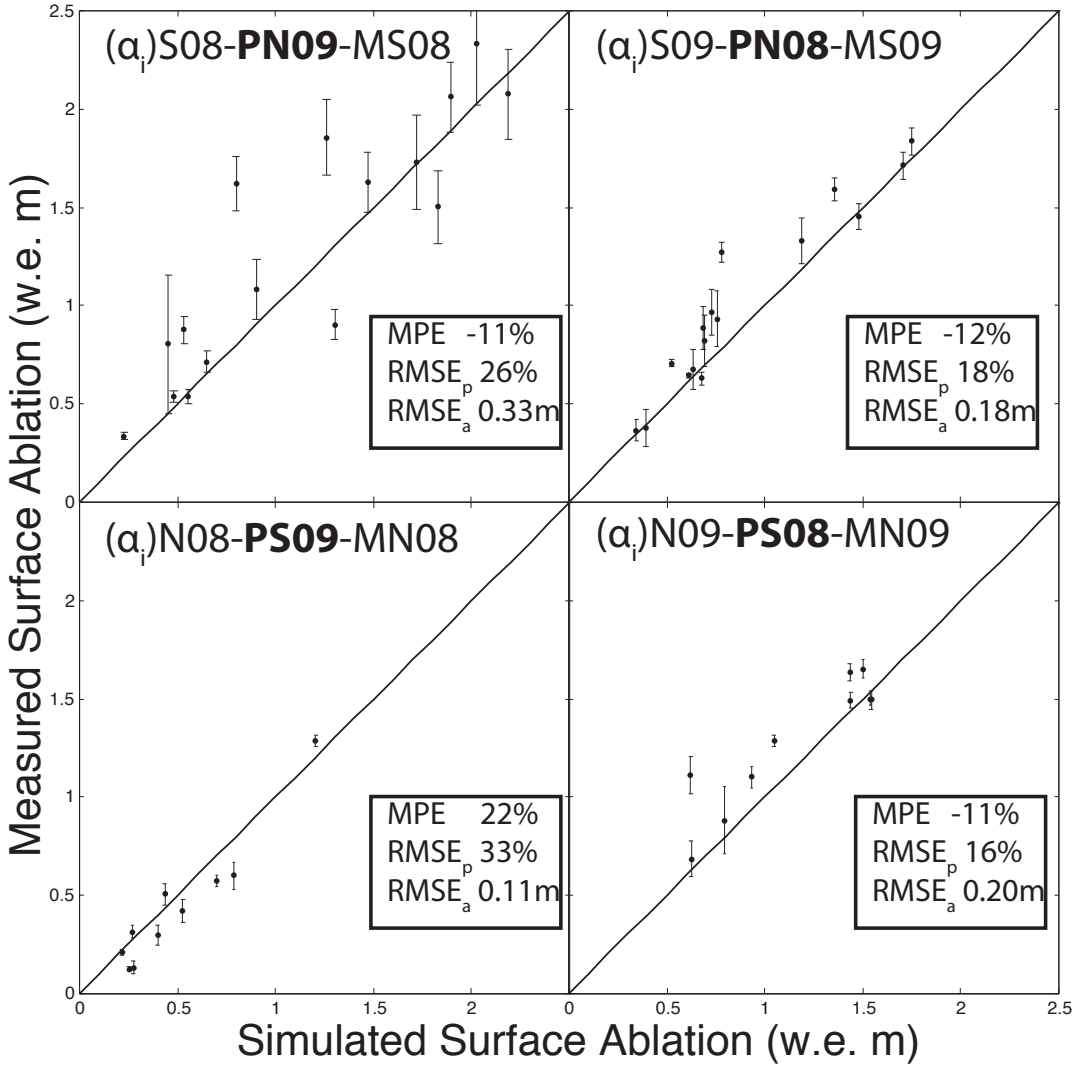

Figure 6.15: Comparison of results of the spatial-temporal parameter transfer experiment, but with locally-measured ice albedo retained to ablation stake measurements. Notice that the errors are smaller than those produced when ice albedo was transfered.

The STP$-\alpha_i$ experiment is compared to the control runs in Figures 6.13, 6.16 and Tables 6.20 – 6.22. The difference in spatially distributed ablation between this experiment and the control runs show that the differences are mostly confined to the ice–firn transition region in 2009 for both glaciers (Figure 6.16). In 2008 both glaciers show a patchy pattern of overestimation and underestimation of melt, this patchiness is more distinct and extensive for North Glacier than South Glacier. The absolute difference in mass balance ranges from 2–10 w.e. cm (Table 6.21), which is no better than for the STP experiment. The mass balance difference with respect to the control runs are closer to zero for three of the simulations. The net mass balance for South Glacier 2008 was 0 w.e. cm in the STP experiment and -10 w.e. cm in the STP$-\alpha_i$ experiment. In the STP$-\alpha_i$ test instead of a reduction in ablation compensating for additional summer snowfall, the reduction in summer snowfall is compounded by an overestimation of ablation. The differences in energy balance components are dominated by shortwave radiation (Table 6.22), with significant and opposing contributions from net longwave radiation for 2008. Overall, retaining the ice albedo improves the simulation of ablation, but not net mass balance.

Table 6.20: Difference between the spatially distributed ablation for the spatial-temporal parameter transfer experiment, but with locally-measured ice albedo retained and the control experiments expressed as MPE and RMSE.

Simulation	MPE (%)	$RMSE_p$ (%)	$RMSE_a$ (m)
(α_i)S08-**PN08**-MS08	6	14	0.11
(α_i)S09-**PN09**-MS09	2	11	0.09
(α_i)N08-**PS08**-MN08	11	43	0.02
(α_i)N09-**PS09**-MN09	-2	5	0.05

Together the parameter transfer experiments indicate that the parameters derived on a glacier for one year can be used in other years without introducing more uncertainty than that inherent in modelling glacier mass balance with a DEBM. Parameter transferability in

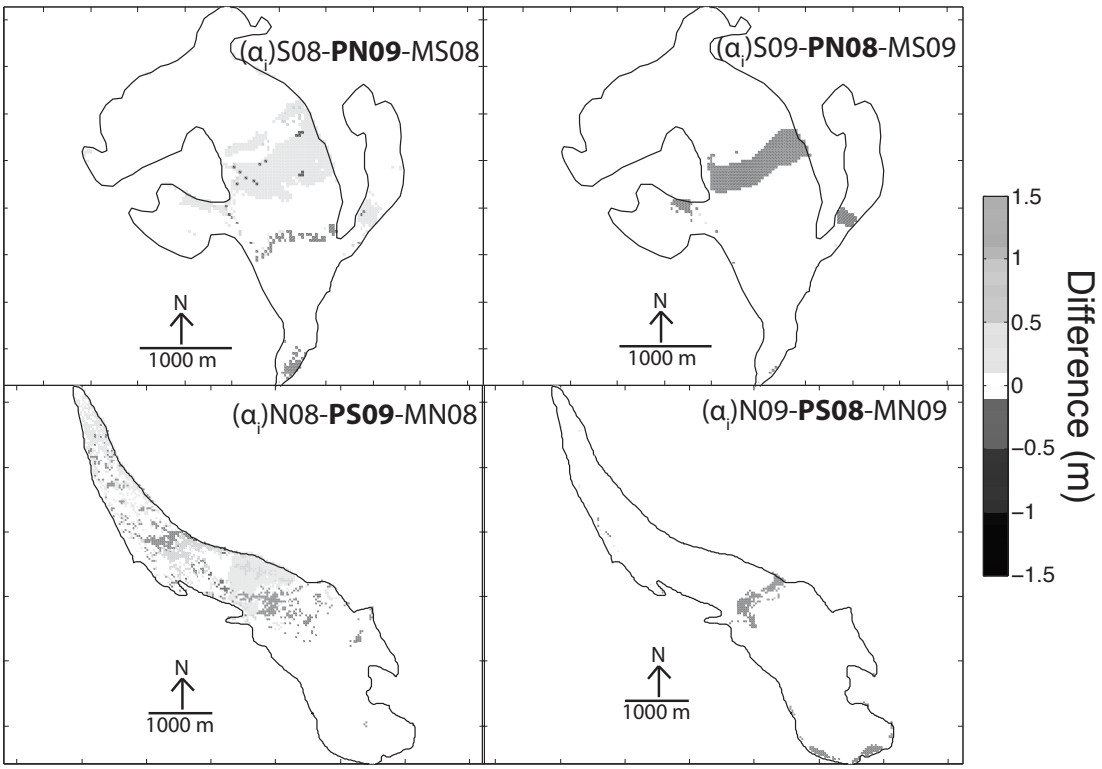

Figure 6.16: Difference in spatially distributed ablation as calculated by the spatial-temporal parameter transfer experiment, but with locally-measured ice albedo retained and the spatially distributed ablation in the control runs. Note that white delineates near-zero difference.

Table 6.21: Spatially averaged mass balance components as estimated for the spatial-temporal parameter transfer experiment, but with locally-measured ice albedo retained, and the difference in summer ablation and mass balance with respect to the control runs. C_{w} is winter surface accumulation, C_{s} is summer surface accumulation, A_{s} is summer surface ablation, B_{n} is surface net balance, $\triangle A_s$ is the difference in summer ablation, and $\triangle B_n$ is the difference in net mass balance with respect to the control run. Units are in w.e. m.

Simulation	C_w	C_s	A_s	B_n	$\triangle A_s$	$\triangle B_n$
(α_{i})S08-**PN08**-MS08	0.33	0.24	−0.84	−0.28	−0.05	−0.10
(α_{i})S09-**PN08**-MS09	0.53	0.04	−0.83	−0.25	−0.02	−0.03
(α_{i})N08-**PS08**-MN08	0.23	0.20	−0.52	−0.09	−0.05	−0.02
(α_{i})N09-**PS09**-MN09	0.38	0.08	−0.68	−0.22	0.02	0.03

Table 6.22: Difference in spatially averaged energy balance components between spatial-temporal parameter transfer experiment, but with locally-measured ice albedo retained and control runs. $\triangle S_{\mathrm{net}}$ is the difference in net shortwave radiation, $\triangle L_{\mathrm{net}}$ is the difference in net longwave radiation, $\triangle Q_{\mathrm{H}}$ is the difference in sensible heat flux, $\triangle Q_{\mathrm{L}}$ is the difference in latent heat flux, $\triangle Q_{\mathrm{g}}$ is the difference in subsurface heat flux, and $\triangle Q_{\mathrm{M}}$ is the difference in the energy available for melt. Units are in W m^{-2}

Simulation	$\triangle S_{\mathrm{net}}$	$\triangle L_{\mathrm{net}}$	$\triangle Q_{\mathrm{H}}$	$\triangle Q_{\mathrm{L}}$	$\triangle Q_{\mathrm{g}}$	$\triangle Q_{\mathrm{M}}$
(α_{i})S08-**PN08**-MS08	3.4	−1.7	−0.1	−0.2	0.2	−0.6
(α_{i})S09-**PN09**-MS09	0.4	0.1	0.1	0.2	0	0.8
(α_{i})N08-**PS08**-MN08	4.1	−1.5	−0.5	−0.6	0.1	1.7
(α_{i})N09-**PS09**-MN09	−1.3	0.3	0.2	−0.1	0	-0.9

space generally produces large deviations in ablation with respect to the control run, especially in the ablation zones of the glaciers. These deviations can be minimized by using locally derived ice albedo, but differences of up to 10 w.e. cm with respect to the control runs can be expected. This indicates that transferring parameter values over a large region would be greatly improved if local ice albedos can be measured. Transferring parameter values in both space and time together produced errors similar to those found by transferring parameters in space.

6.5 Transferring meteorological variables

To examine the transferability of the meteorological variables used to drive the DEBM an experiment was conducted in which the meteorological variables measured on one glacier were used to drive the DEBM for the other, while retaining the locally derived parameter values (M experiment). The comparison of this experiment to the validation data is shown in Figures 6.17, 6.18 and Table 6.23. A clear problem arises in this comparison for North Glacier in 2009 in that the meteorological data from South Glacier in 2009 ends on the 26th of July 2009 (day 207) while the ablation stakes on North Glacier were not surveyed until the 4th of August 2009 (day 216), over a week later at the height of the melt season. Given this situation one would expect the North Glacier 2009 DEBM forced with South Glacier 2009 meteorological data to underestimate melt compared to the ablation stake measurements. To make the simulated ablation more comparable to the stake measurements, the North Glacier 2009 M test was augmented with the last seven days of simulated melt from the control run for North Glacier 2009. Note that this extrapolation does not affect the comparison of the North Glacier 2009 M test and the North Glacier 2009 control run as only the periods where both data sets overlap is used in those comparisons.

The comparison between the simulations of ablation at the stake location and measured ablation shows an interesting duality (Figure 6.17). The tests for South Glacier have RMSE values close to those found in the control runs and have MPEs better than the control runs at 1–2 % biased (Table 6.23). The tests for North Glacier have RMSE and MPE values much greater than in the control runs, with a clear divergence from the 1:1 line. The comparison to the USDG record has a similar pattern (Figure 6.18). The South Glacier tests closely track the control runs, while the North Glacier tests drastically underestimate ablation.

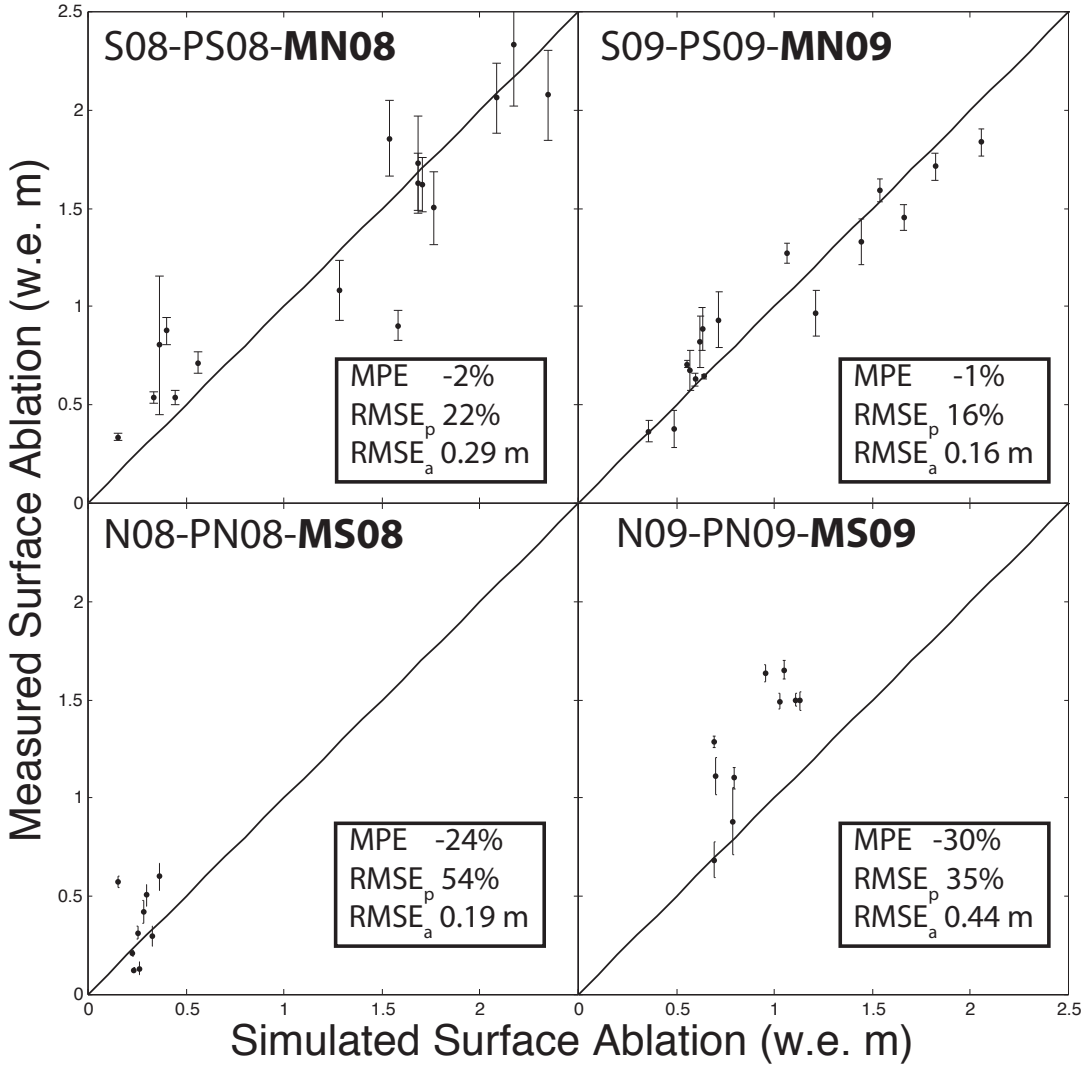

Figure 6.17: Comparison of results of the meteorological variable transfer experiment to ablation stake measurements.

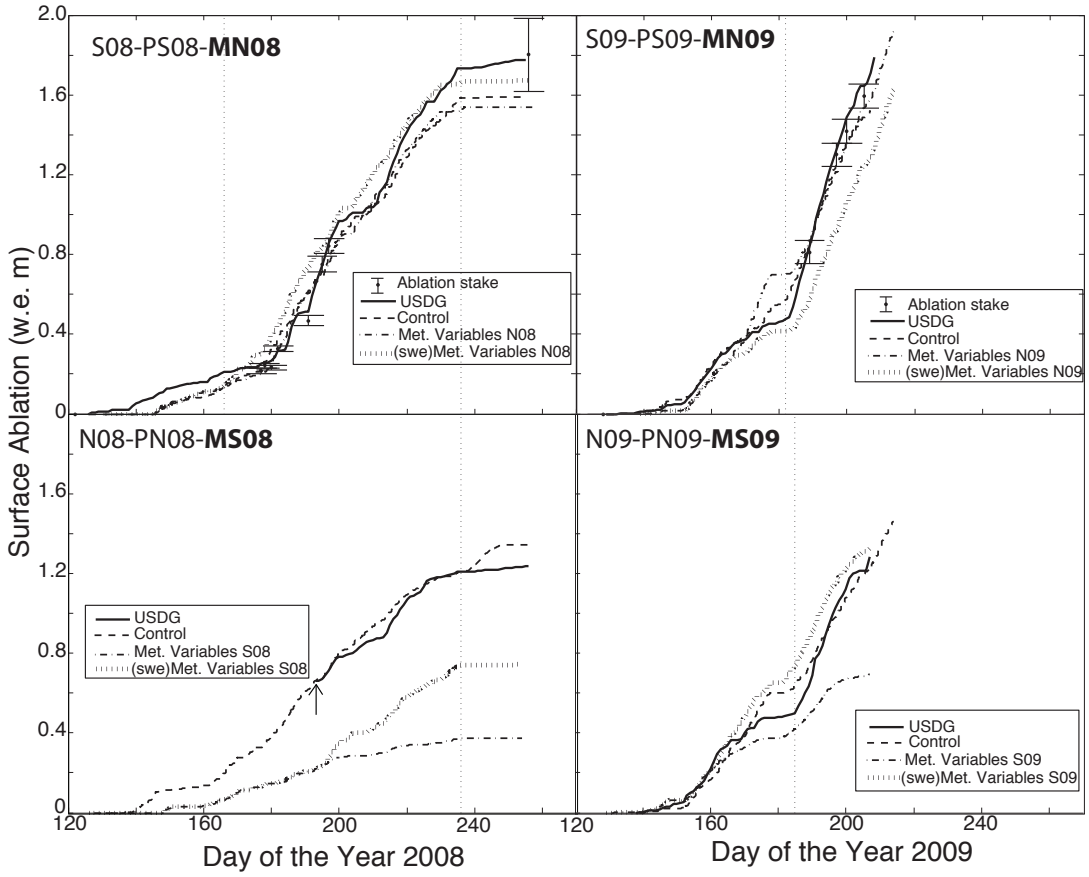

Figure 6.18: Comparison of USDG record of ablation and modelled ablation for the meteorological variable transfer experiment. Control runs are also shown for comparison. For South Glacier ablation stake measurements from near the USDG are also shown. Dotted vertical lines delineate snow–ice transitions. Arrow indicates when the USDG on North Glacier began functioning in 2008.

Table 6.23: Differences between simulated and measured ablation at stake locations for the meteorological variable transfer experiment.

Simulation	MPE (%)	$RMSE_p$ (%)	$RMSE_a$ (m)
S08-PS08-**MN08**	−2	22	0.29
S09-PS08-**MN09**	−1	16	0.16
N08-PN08-**MS08**	−24	54	0.19
N09-PN09-**MS09**	−30	35	0.44

The comparison between the M experiment and the control runs is shown in Figures 6.18, 6.19, and Tables 6.24 – 6.26. The difference in spatially distributed ablation between this experiment and the control runs demonstrate that most of the difference is concentrated in the ablation zone for both glaciers in both years (Figure 6.19). The South Glacier M tests overestimate melt in the ablation zone with respect to the control run. The North Glacier M tests underestimates melt in the ablation zone with respect to the control run. The absolute difference in estimated mass balance between the M tests and the control runs are very large, ranging from 25–50 w.e. cm (Table 6.25). The absolute difference in ablation is between 8–14 w.e. cm. Transferring meteorological parameters therefore creates mass balances completely unlike those found using locally derived variables, indicating that straight meteorological transfer should not be used for DEBMs in the Donjek Range study sites. The differences in energy balance components show that there are significant differences in all of the components from their control values (Table 6.26).

Table 6.24: Difference between the spatially distributed ablation for the meteorological variable transfer experiment and the control runs expressed as MPE and RMSE.

Simulation	MPE (%)	$RMSE_p$ (%)	$RMSE_a$ (m)
S08-PS08-**MN08**	10	27	0.22
S09-PS09-**MN09**	13	24	0.19
N08-PN08-**MS08**	−26	50	0.23
N09-PN09-**MS09**	−16	26	0.23

6.5.1 Assessing the role of initial snow-depth

From examining the mass balance components from Table 6.25 it becomes obvious that the largest source of difference in estimated mass balance between the M experiment and control runs is the estimated winter accumulation (C_w), which is the spatially averaged initial snow-depth. Unlike the true meteorological variables, initial snow-depth is not measured

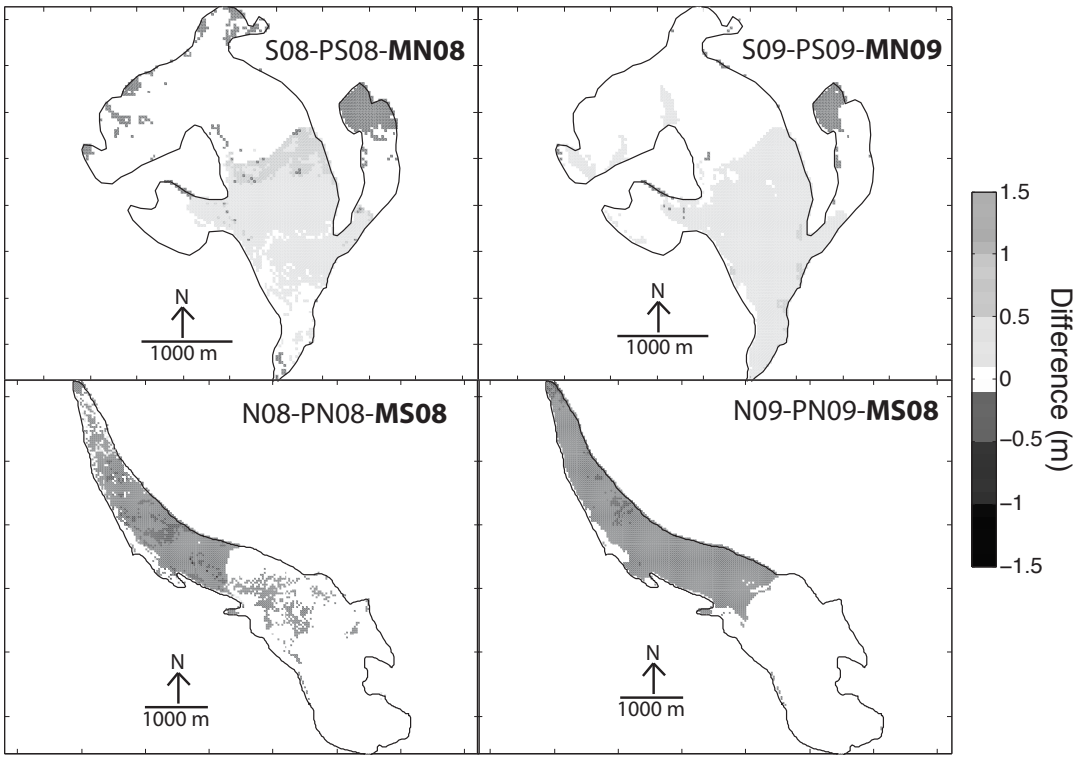

Figure 6.19: Difference in spatially distributed ablation as calculated by the meteorological variable transfer experiment and the spatially distributed ablation in the control runs. Note that white delineates near-zero difference.

Table 6.25: Spatially averaged mass balance components as estimated for the meteorological variable transfer experiment, and the difference in summer ablation and mass balance with respect to the control experiments. C_w is winter surface accumulation, C_s is summer surface accumulation, A_s is summer surface ablation, B_n is surface net balance, $\triangle A_s$ is the difference in summer ablation, and $\triangle B_n$ is the difference in net mass balance with respect to the control run. Units are in w.e. m.

Simulation	C_w	C_s	A_s	B_n	$\triangle A_s$	$\triangle B_n$
S08-PS08-**MN08**	0.23	0.21	−0.87	−0.43	−0.08	−0.25
S09-PS09-**MN09**	0.39	0.08	−0.92	−0.45	−0.11	−0.22
N08-PN08-**MS08**	0.33	0.34	−0.34	0.23	0.12	0.30
N09-PN09-**MS09**	0.76	0.04	−0.56	0.25	0.14	0.50

Table 6.26: Difference in spatially averaged energy balance components between meteorological variable transfer experiment and control runs. $\triangle S_\mathrm{net}$ is the difference in net shortwave radiation, $\triangle L_\mathrm{net}$ is the difference in net longwave radiation, $\triangle Q_\mathrm{H}$ is the difference in sensible heat flux, $\triangle Q_\mathrm{L}$ is the difference in latent heat flux, $\triangle Q_\mathrm{g}$ is the difference in subsurface heat flux, and $\triangle Q_\mathrm{M}$ is the difference in the energy available for melt. Units are in W m^{-2}

	$\triangle S_\mathrm{net}$	$\triangle L_\mathrm{net}$	$\triangle Q_\mathrm{H}$	$\triangle Q_\mathrm{L}$	$\triangle Q_\mathrm{g}$	$\triangle Q_\mathrm{M}$
S08-PS08-**MN08**	−3.1	3.5	1.3	0	0.7	2.4
S09-PS09-**MN09**	2.0	4.2	1.8	−2.3	0.6	6.2
N08-PN08-**MS08**	1.2	−3.6	−0.9	0.4	−0.8	−3.8
N09-PN09-**MS09**	−3.6	−4.8	−1.4	2.4	−0.6	−8.0

by the AWS but interpolated from snow-depth measurements made during the spring field campaign (see *Data Processing)*. Transferring this initial condition by imposing the regression parameters from one glacier on the other is an imprecise way of extrapolating initial snow-depth. To isolate the effect of transferring this quantity four tests were conducted in which all of the meteorological variables but initial snow-depth were transferred from one glacier to the other.

The meteorological variable transfer experiment retaining local initial snow-depth (M$-$*swe*) is compared to the validation data in Figures 6.18, 6.20 and Table 6.27. The comparison between the simulated and the measured ablation at the stake locations (Figure 6.20) shows that for three of the tests the RMSE and MPE are larger than in the control runs, while for the North Glacier 2009 test the errors are smaller than in the control run. The South Glacier tests reproduce ablation with less skill than in the M experiment, while the North Glacier tests reproduce ablation with more skill. The overall effect is that the experiment has lower skill than the control run but produces equal magnitudes of error for both glaciers. The pattern is similar for the comparison with respect to the USDG record. The South Glacier tests are further from the USDG record than the M experiment but the North Glacier tests are closer to the USDG record (Figure 6.18). The North Glacier 2008 M$-$*swe* test underestimates ablation significantly at the AWS location, but not as poorly as in M experiment.

Table 6.27: Differences between simulated and measured ablation at stake locations for the meteorological variable transfer experiment, but with locally-measured initial snow-depth retained.

Simulation	MPE (%)	$RMSE_p$ (%)	$RMSE_a$ (m)
(*swe*)S08-PS08-**MN08**	-13	28	0.36
(*swe*)S09-PS08-**MN09**	-19	26	0.27
(*swe*)N08-PN08-**MS08**	14	38	0.13
(*swe*)N09-PN09-**MS09**	-2	11	0.14

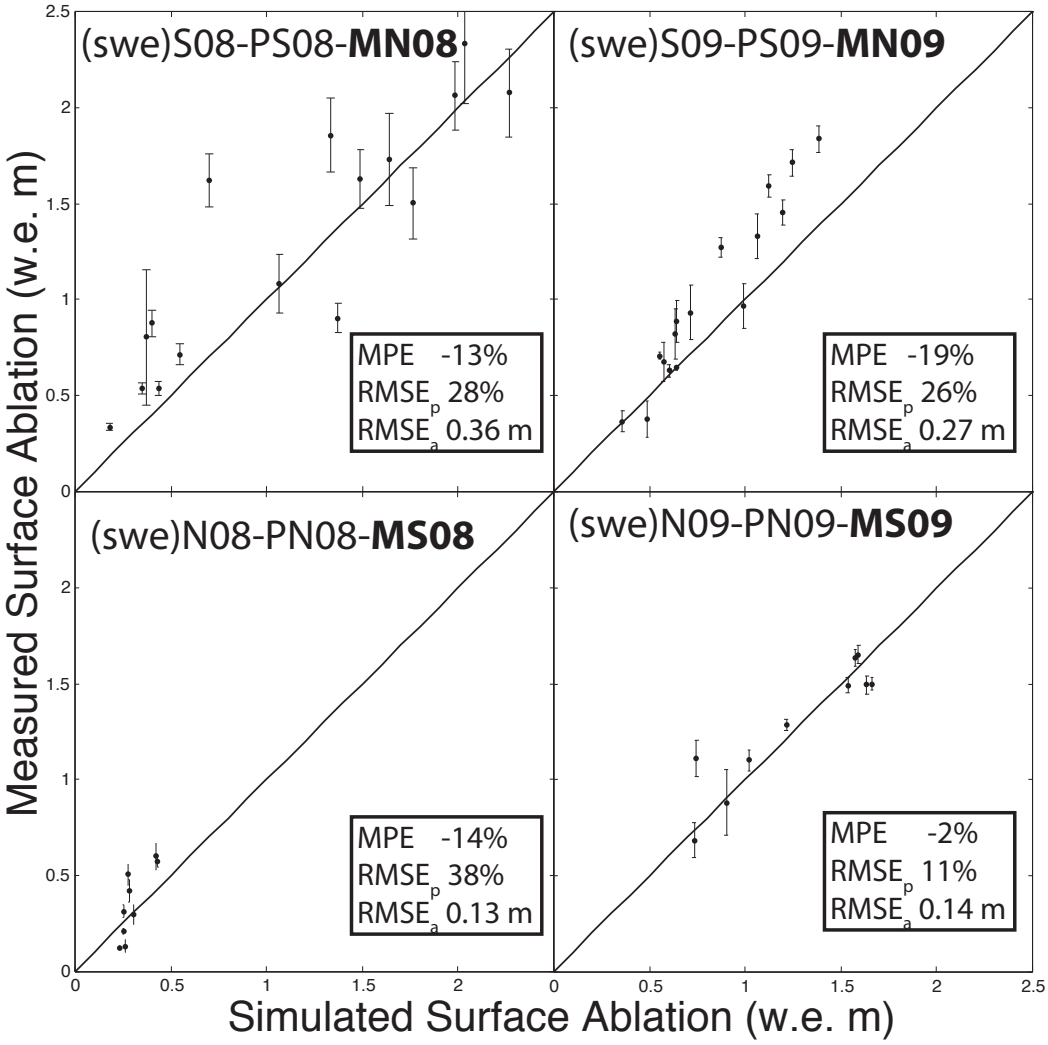

Figure 6.20: Comparison of results of the meteorological variable transfer experiment, but with locally-measured snow-depth retained to ablation stake measurements.

The comparison between the M−*swe* experiment and the control runs are shown in Figures 6.18, 6.21 and Tables 6.28 – 6.30. The difference in spatially distributed ablation between this experiment and the control runs show an expected pattern (Figure 6.21). The South Glacier 2008 M−*swe* test overestimates ablation with respect to the control run, while the North Glacier 2008 M−*swe* test underestimates ablation. The South Glacier 2009 M−*swe* test underestimates ablation with respect to the control run, while the North Glacier 2008 M−*swe* test overestimates ablation. If meteorological variables measured on one glacier cause underestimation when used to force a DEBM on another, meteorological variables measured on the other will cause an overestimation on the first glacier. The absolute difference in mass balance between this experiment and the control runs range from 9–14 w.e. cm and absolute difference in ablation range from 1–8 w.e. cm (Table 6.29). These differences are smaller than those calculated in the M experiment but larger than those calculated in the parameter transfer experiments. There are large differences in all of the energy balance components, but of opposing signs such that they mostly cancel out (Table 6.30).

Table 6.28: Difference between the spatially distributed ablation for the meteorological variable transfer experiment, but with locally-measured initial snow-depth retained and the control runs expressed as MPE and RMSE.

Simulation	MPE (%)	$RMSE_p$ (%)	$RMSE_a$ (m)
(*swe*)S08-PS08-**MN08**	1	19	0.15
(*swe*)S09-PS09-**MN09**	−8	18	0.15
(*swe*)N08-PN08-**MS08**	−15	35	0.16
(*swe*)N09-PN09-**MS09**	−9	13	0.11

Overall, transferring meteorological variables creates larger errors in the DEBM simulations than transferring parameter values. Significant errors in mass balance occur unless the initial snow-depth is known for each glacier.

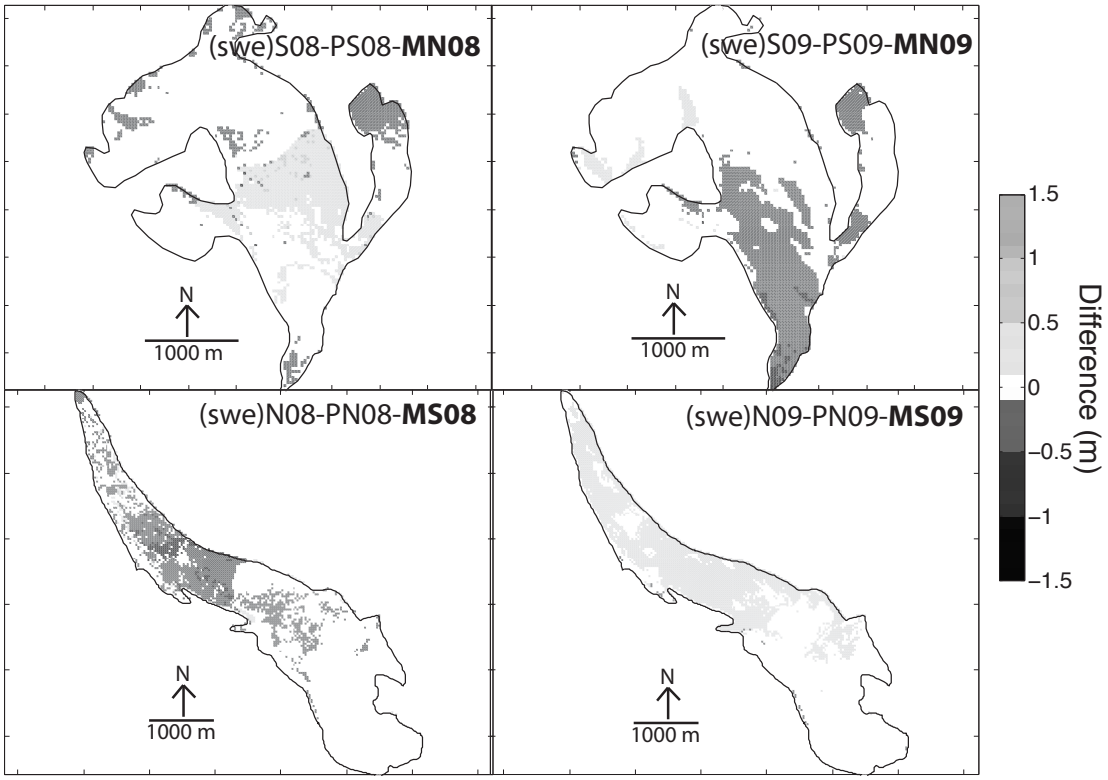

Figure 6.21: Difference in spatially distributed ablation as calculated by the meteorological variable transfer experiment, but with locally-measured initial snow-depth retained and the spatially distributed ablation in the control runs. Note that white delineates near-zero difference.

Table 6.29: Spatially averaged mass balance components as estimated for the meteorological variable transfer experiment, but with locally-measured initial snow depth, and the difference in summer ablation and mass balance with respect to the control runs. C_{w} is winter surface accumulation, C_{s} is summer surface accumulation, A_{s} is summer surface ablation, B_{n} is surface net balance, $\triangle A_s$ is the difference in summer ablation, and $\triangle B_n$ is the difference in net mass balance with respect to the control run. Units are in w.e. m.

Simulation	C_w	C_s	A_s	B_n	$\triangle A_s$	$\triangle B_n$
(*swe*)S08-PS08-**MN08**	0.33	0.21	−0.80	−0.27	−0.01	−0.09
(*swe*)S09-PS09-**MN09**	0.53	0.08	−0.75	−0.14	0.06	0.09
(*swe*)N08-PN08-**MS08**	0.23	0.24	−0.40	0.07	0.07	0.14
(*swe*)N09-PN09-**MS09**	0.38	0.04	−0.78	−0.35	−0.08	−0.10

Table 6.30: Difference in spatially averaged energy balance components between meteorological variable transfer experiment, but with locally-measured initial snow-depth retained and control runs. $\triangle S_{\mathrm{net}}$ is the difference in net shortwave radiation, $\triangle L_{\mathrm{net}}$ is the difference in net longwave radiation, $\triangle Q_{\mathrm{H}}$ is the difference in sensible heat flux, $\triangle Q_{\mathrm{L}}$ is the difference in latent heat flux, $\triangle Q_{\mathrm{g}}$ is the difference in subsurface heat flux, and $\triangle Q_{\mathrm{M}}$ is the difference in the energy available for melt. Units are in $\mathrm{W\,m^{-2}}$

Simulation	$\triangle S_{\mathrm{net}}$	$\triangle L_{\mathrm{net}}$	$\triangle Q_{\mathrm{H}}$	$\triangle Q_{\mathrm{L}}$	$\triangle Q_{\mathrm{g}}$	$\triangle Q_{\mathrm{M}}$
(*swe*)S08-PS08-**MN08**	−5.2	3.5	1.3	0.1	0.7	0.3
(*swe*)S09-PS09-**MN09**	−8.0	4.5	1.7	−2.2	0.6	−3.5
(*swe*)N08-PN08-**MS08**	3.1	−3.8	−0.9	0.3	−0.9	−2.1
(*swe*)N09-PN09-**MS09**	9.7	−5.4	−1.6	2.4	−0.6	4.5

6.6 Transferring parameters and meteorological variables

The optimally transferable glacier melt model is one that can be driven by and calibrated with data from one well studied glacier, and then extended unaltered to all glaciers within some large region with minimal error. To test the model in this capacity an experiment is conducted in which both the parameter values and meteorological variables are transfered from one glacier to the other (MP experiment).

The comparison between the validation data and the results of this experiment are shown in Figures 6.22, 6.23 and Table 6.31. The comparison between the simulated and the measured ablation at the stake locations shows that for three of the tests the errors produced are significantly larger than in the control runs (Figure 6.22); the South Glacier 2009 test is the exception with an RMSE only 3 % larger than the control run and an MPE 1 % closer to zero than the control run (Table 6.31). Together this experiment display similar levels of error to both the M, SP and STP experiments. The comparison between the MP experiment at the AWS locations and the USDG records shows more complex relationships than the previous experiments (Figure 6.23). The South Glacier 2008 MP test overestimates ablation for the early part of the simulation before closely tracking the control run after 20th of July 2008 (day 200). The South Glacier 2009 MP test closely tracks both the USDG record and control run for both the beginning and end of the simulation with a period of divergence in mid-summer. The North Glacier 2008 MP test underestimates both the control run and the USDG record for the entire simulation, and the North Glacier 2009 MP test diverges from the control after 19th of June 2009 (day 170), underestimating ablation.

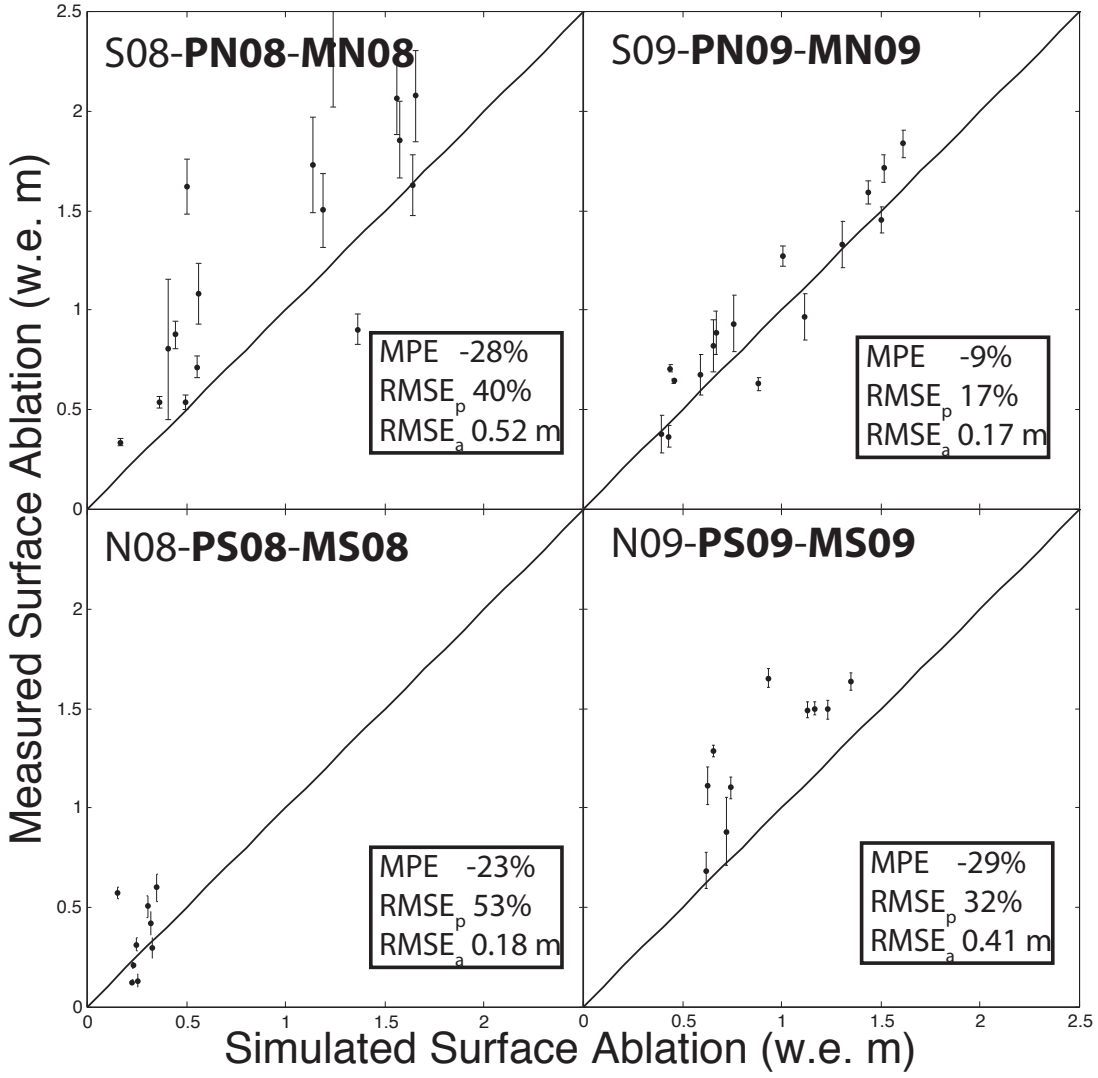

Figure 6.22: Comparison of results of the parameter and meteorological variable transfer experiment to ablation stake measurements.

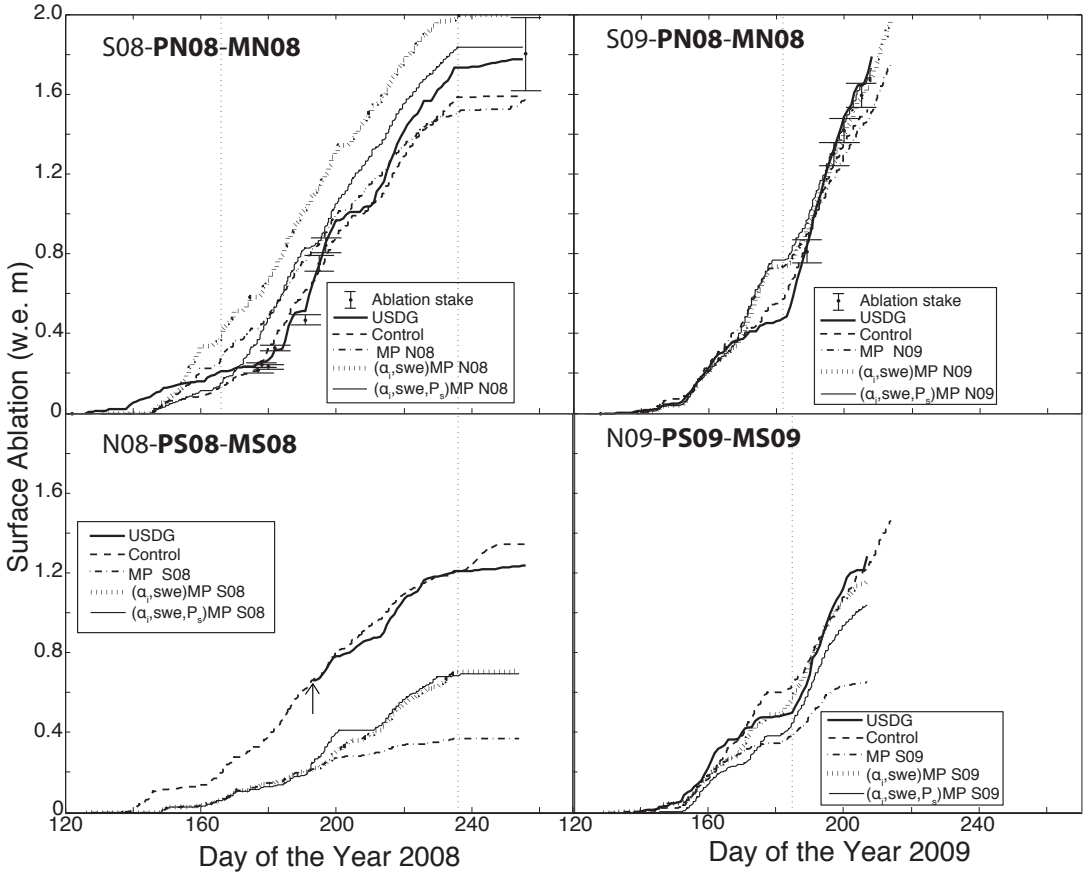

Figure 6.23: Comparison of USDG record of ablation and modelled ablation for the parameter and meteorological variable transfer experiment. Control runs are also shown for comparison. For South Glacier ablation stake measurements from near the USDG are also shown. Dotted vertical lines delineate snow–ice transitions. Arrow indicates when the USDG on North Glacier began functioning in 2008.

Table 6.31: Differences simulated and measured ablation at stake locations for the parameter and meteorological variable transfer experiment.

Simulation	MPE (%)	$RMSE_p$ (%)	$RMSE_a$ (m)
S08-**PN08**-**MN08**	−28	40	0.52
S09-**PN08**-**MN09**	−9	17	0.17
N08-**PS08**-**MS08**	−23	53	0.18
N09-**PS09**-**MS09**	−29	32	0.41

The comparison between the MP experiment and the control runs are shown in Figures 6.23, 6.24 and Tables 6.32 – 6.34. The differences in spatially distributed ablation between this experiment and the control runs show more complicated patterns than in the previously discussed experiments (Figure 6.24). The South Glacier 2008 MP test has a region of underestimated ablation in the low ablation zone, a region of overestimation in the mid-ablation zone, and a second region of underestimation near the ice–firn transition zone, with respect to the control run. The South Glacier 2009 MP test has a small region of underestimated ablation near the terminus of the glacier and a wavy pattern of overestimated ablation and small differences in the rest of the ablation zone, with respect to the control run . The North Glacier 2008 MP test displays overestimation near the terminus, a region of underestimation of ablation in the rest of the ablation zone and patchy underestimation in the accumulation zone, with respect to the control run. The North Glacier 2009 MP test displays the simplest pattern with underestimation of ablation over the entire ablation zone, with respect to the control run. The difference in mass balance components between the MP experiment and the control runs is large for all four tests (Table 6.33). The absolute difference in ablation ranges from 5–18 w.e. cm and absolute difference in mass balance between 12–55 w.e. cm, with North Glacier taking on positive instead of negative mass balance. The net result is a poor simulation of mass balance when using one site as an extension of the other. The differences in energy balance components are large for each of the components with no component standing out as the largest source of error (Table 6.34). The overall result of the MP experiment is that extending the DEBM over a large region without re-calibration leads to large errors.

6.6.1 Assessing the role of Ice albedo and initial snow-depth

Given that the ideal outcome of full transferability is not possible within acceptable error limits, it is reasonable to test if there are parameters or variables that could be found independently for each glacier, while being able to transfer most of the meteorological variables and parameter values. The two most logical quantities to retain at their locally derived values are ice albedo and initial snow-depth, as these quantities improved model performance

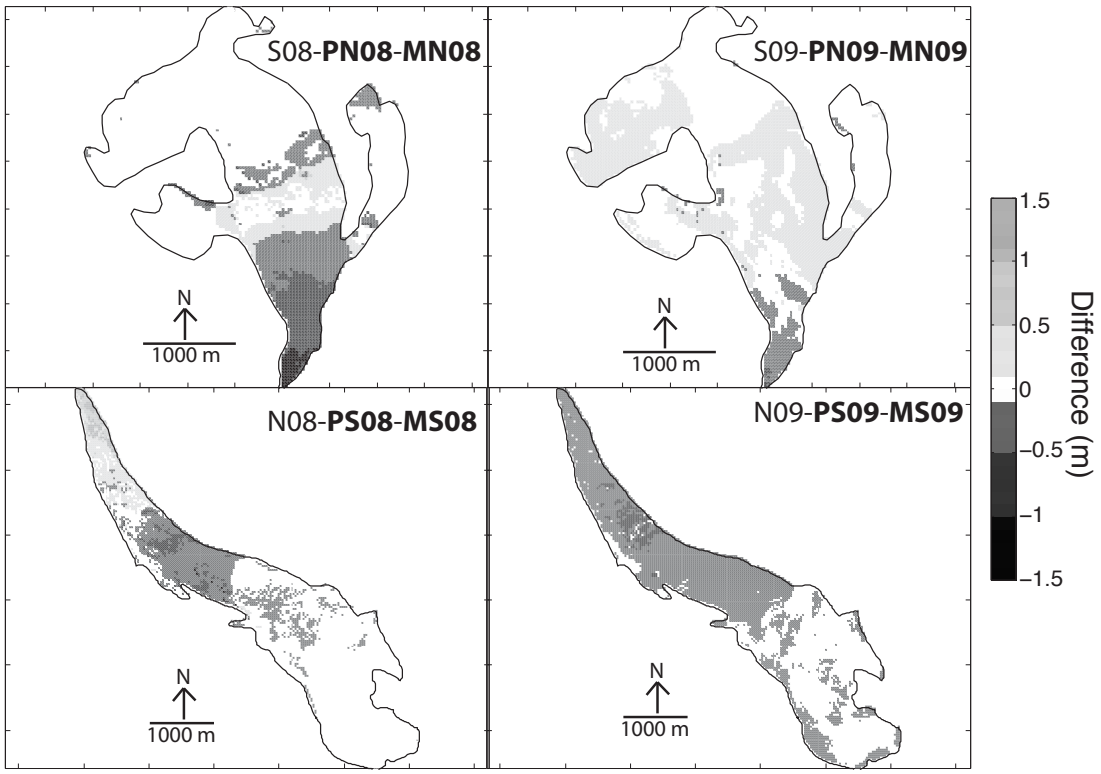

Figure 6.24: Difference in spatially distributed ablation as calculated by the parameter and meteorological variable transfer experiment and the spatially distributed ablation in the control runs. Note that white delineates near-zero difference.

Table 6.32: Difference between the spatially distributed ablation for the parameter and meteorological variable transfer experiment and the control runs expressed as MPE and RMSE.

Simulation	MPE (%)	$RMSE_p$ (%)	$RMSE_a$ (m)
S08-**PN08**-**MN08**	−12	35	0.27
S09-**PN09**-**MN09**	10	19	0.15
N08-**PS08**-**MS08**	−12	60	0.28
N09-**PS09**-**MS09**	−21	27	0.23

Table 6.33: Spatially averaged mass balance components as estimated for the parameter and meteorological variable transfer experiment, and the difference in summer ablation and mass balance with respect to the control runs. C_{w} is winter surface accumulation, C_{s} is summer surface accumulation, A_{s} is summer surface ablation, B_{n} is surface net balance, $\triangle A_s$ is the difference in summer ablation, and $\triangle B_n$ is the difference in net mass balance with respect to the control run. Units are in w.e. m.

Simulation	C_w	C_s	A_s	B_n	$\triangle A_s$	$\triangle B_n$
S08-**PN08**-**MN08**	0.23	0.17	−0.70	−0.30	0.10	−0.12
S09-**PN09**-**MN09**	0.39	0.06	−0.89	−0.44	−0.08	−0.21
N08-**PS08**-**MS08**	0.33	0.30	−0.41	0.22	0.05	0.29
N09-**PS09**-**MS09**	0.76	0.06	−0.52	0.30	0.18	0.55

Table 6.34: Difference in spatially averaged energy balance components between parameter and meteorological variable transfer experiment and control runs. $\triangle S_{\mathrm{net}}$ is the difference in net shortwave radiation, $\triangle L_{\mathrm{net}}$ is the difference in net longwave radiation, $\triangle Q_{\mathrm{H}}$ is the difference in sensible heat flux, $\triangle Q_{\mathrm{L}}$ is the difference in latent heat flux, $\triangle Q_{\mathrm{g}}$ is the difference in subsurface heat flux, and $\triangle Q_{\mathrm{M}}$ is the difference in the energy available for melt. Units are in $\mathrm{W\,m^{-2}}$

Simulation	$\triangle S_{\mathrm{net}}$	$\triangle L_{\mathrm{net}}$	$\triangle Q_{\mathrm{H}}$	$\triangle Q_{\mathrm{L}}$	$\triangle Q_{\mathrm{g}}$	$\triangle Q_{\mathrm{M}}$
S08-**PN08**-**MN08**	−8.7	3.4	1.6	0.2	0.6	−3.0
S09-**PN09**-**MN09**	0.2	4.0	1.9	−2.1	0.6	4.6
N08-**PS08**-**MS08**	3.6	−3.3	−1.3	0.2	−0.8	−1.7
N09-**PS09**-**MS09**	−6.4	−3.9	−1.9	2.4	−0.7	−10.4

in the PS, STP and M experiments. Therefore an experiment was carried out in which all of the parameters were transfered except for ice albedo, and all of the meteorological variables are transfered except initial snow-depth (MP$-\alpha_i$,swe experiment).

The comparison between the MP$-\alpha_i$,swe experiment and the validation data are shown in Figures 6.23, 6.25 and Table 6.35. The comparison between the simulated and measured ablation at the stake locations (Figure 6.25) shows that for the 2008 simulations the errors are larger than the control runs but smaller than in the full MP experiment. The South Glacier 2009 MP$-\alpha_i$,swe test has larger error than either the control run or the full MP test, but with an RMSE of 24 % (Table 6.35) the error is smaller than many of the other transfer experiments. The North Glacier 2009 MP$-\alpha_i$,swe test has the same RMSE as the control run and an MPE close to zero. Only the North Glacier 2008 MP$-\alpha_i$,swe test shows a trend that greatly deviates from the 1 : 1 line. The comparison between the MP$-\alpha_i$,swe experiment and the USDG record shows that the South Glacier 2008 test overestimates ablation compared to both the USDG record and the control run (Figure 6.23). The North Glacier 2008 MP$-\alpha_i$,swe test underestimates ablation compared to the USDG record and control run, but not as badly as the full MP experiment. The South Glacier 2009 MP$-\alpha_i$,swe test tracks the USDG record except for a period in mid-summer and the North Glacier 2009 MP$-\alpha_i$,swe test tracks the control run in the early part of the simulation and the USDG record in the latter part of the simulation.

Table 6.35: Difference between simulated and measured ablation at stake locations for the parameter and meteorological variable transfer experiment, but with locally-measured ice albedo and initial snow-depth.

Simulation	MPE (%)	$RMSE_p$ (%)	$RMSE_a$ (m)
(α_i,*swe*)S08-**PN08**-**MN08**	−11	32	0.41
(α_i,*swe*)S09-**PN08**-**MN09**	−14	24	0.25
(α_i,*swe*)N08-**PS08**-**MS08**	−19	43	0.15
(α_i,*swe*)N09-**PS09**-**MS09**	−6	15	0.20

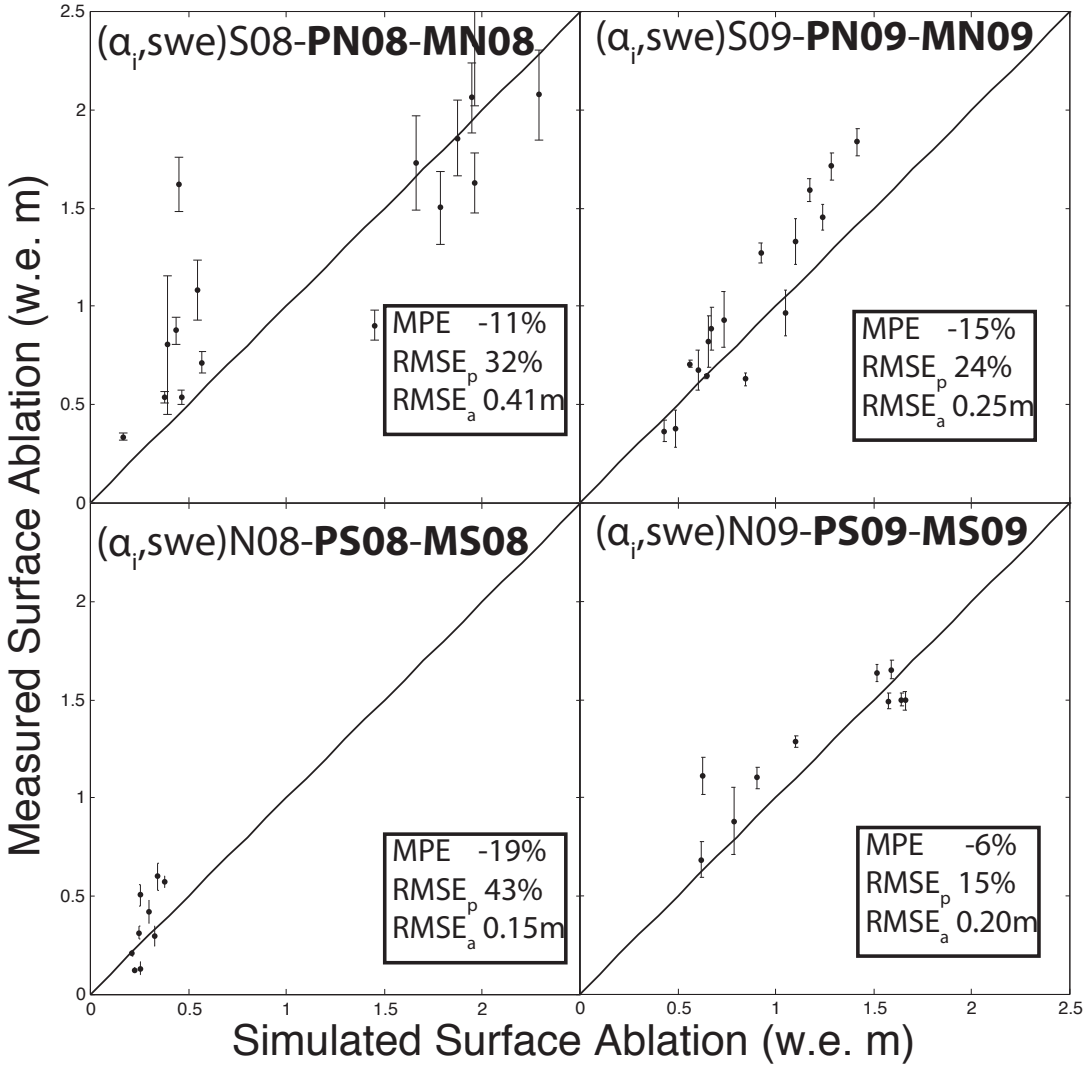

Figure 6.25: Comparison of results of parameter and meteorological variable transfer experiment, but with locally-measured ice albedo and initial snow-depth retained to ablation stake measurements.

The comparison between the MP$-\alpha_i$,swe experiment and the control runs are shown in Figures 6.23, 6.26, Tables 6.36 – 6.38. The difference between the spatially distributed ablation in this experiment and the spatially distributed ablation in the control runs show general improvement from the full MP experiment (Figure 6.26). The South Glacier 2008 MP$-\alpha_i$,swe test displays one band of overestimation of ablation in the mid-ablation zone and one band of underestimation of ablation near the ice–firn transition, with respect to the control run. The South Glacier 2009 MP$-\alpha_i$,swe test shows a band of overestimation of ablation near the ice–firn transition and a wavy pattern of underestimation in the ablation zone, with respect to the control run. The North Glacier 2008 MP$-\alpha_i$,swe test displays patches of over and underestimation in the ablation zone with underestimation dominant and the North Glacier 2009 MP$-\alpha_i$,swe test show only small differences across its surface, with respect to the control run. The absolute difference in ablation between this experiment and the control runs ranges from 0–7 w.e. cm, with the South Glacier 2009 test at 0 w.e. cm, the North Glacier 2009 and the South Glacier 2008 tests at 1 w.e. cm difference, and the North Glacier 2008 test at 7 w.e. cm difference (Table 6.37). The absolute difference in mass balance ranges between 0–20 w.e. cm, with the 2009 simulations very close too no difference and the 2008 simulation having a large mass balance differences. The difference in energy balance components is large for each of the components but tend to cancel out resulting in the small difference in Q_M, except for the North Glacier 2008 test (Table 6.38).

Table 6.36: Difference between the spatially distributed ablation for the parameter and meteorological variable transfer experiment, but with locally-measured ice albedo and initial snow-depth, and the control runs expressed as MPE and RMSE.

Simulation	MPE (%)	$RMSE_p$ (%)	$RMSE_a$ (m)
(α_i,*swe*)S08-**PN08**-**MN08**	2	22	0.17
(α_i,*swe*)S09-**PN09**-**MN09**	0	19	0.15
(α_i,*swe*)N08-**PS08**-**MS08**	−16	38	0.17
(α_i,*swe*)N09-**PS09**-**MS09**	−1	11	0.09

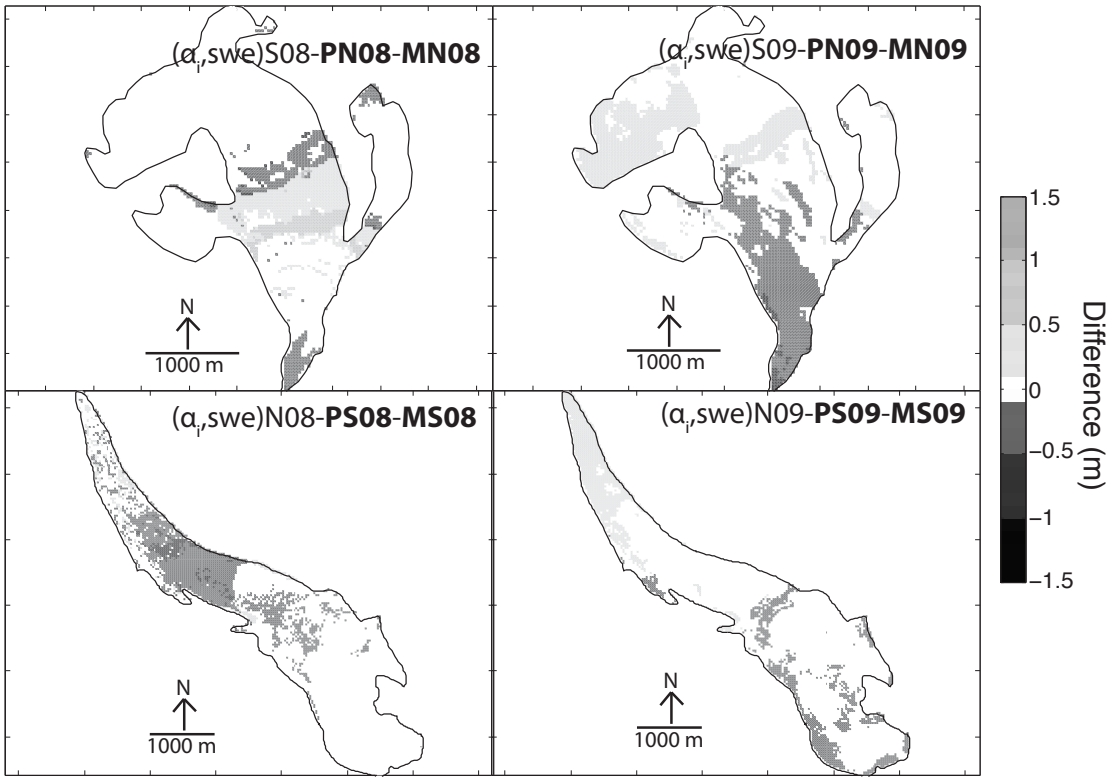

Figure 6.26: Difference in spatially distributed ablation as calculated by the parameter and meteorological variable transfer experiment, but with locally-measured ice albedo and initial snow-depth retained and the spatially distributed ablation in the control runs. Note that white delineates near-zero difference.

Table 6.37: Spatially averaged mass balance components as estimated for the parameter and meteorological variable transfer experiment, but with locally-measured ice albedo and initial snow-depth, and the difference in summer ablation and mass balance with respect to the control experiments. C_{w} is winter surface accumulation, C_{s} is summer surface accumulation, A_{s} is summer surface ablation, B_{n} is surface net balance, $\triangle A_s$ is the difference in summer ablation, and $\triangle B_n$ is the difference in net mass balance with respect to the control run. Units are in w.e. m.

Simulation	C_w	C_s	A_s	B_n	$\triangle A_s$	$\triangle B_n$
(α_{i},*swe*)S08-**PN08**-**MN08**	0.33	0.18	−0.81	−0.31	−0.01	−0.13
(α_{i},*swe*)S09-**PN09**-**MN09**	0.53	0.06	−0.81	−0.22	0	0.01
(α_{i},*swe*)N08-**PS08**-**MS08**	0.23	0.30	−0.39	0.13	0.07	0.20
(α_{i},*swe*)N09-**PS09**-**MS09**	0.38	0.05	−0.69	−0.25	0.01	0

Table 6.38: Difference in spatially averaged energy balance components between parameter and meteorological variable transfer experiment, but with locally-measured ice albedo and initial snow-depth and control runs. $\triangle S_{\mathrm{net}}$ is the difference in net shortwave radiation, $\triangle L_{\mathrm{net}}$ is the difference in net longwave radiation, $\triangle Q_{\mathrm{H}}$ is the difference in sensible heat flux, $\triangle Q_{\mathrm{L}}$ is the difference in latent heat flux, $\triangle Q_{\mathrm{g}}$ is the difference in subsurface heat flux, and $\triangle Q_{\mathrm{M}}$ is the difference in the energy available for melt. Units are in W m^{-2}

Simulation	$\triangle S_{\mathrm{net}}$	$\triangle L_{\mathrm{net}}$	$\triangle Q_{\mathrm{H}}$	$\triangle Q_{\mathrm{L}}$	$\triangle Q_{\mathrm{g}}$	$\triangle Q_{\mathrm{M}}$
(α_{i},*swe*)S08-**PN08**-**MN08**	−5.3	3.3	1.6	0.1	0.7	0.4
(α_{i},*swe*)S09-**PN09**-**MN09**	−4.7	4.2	2.0	−2.1	0.6	0
(α_{i},*swe*)N08-**PS08**-**MS08**	3.1	−3.4	−1.3	0.1	−0.8	−2.3
(α_{i},*swe*)N09-**PS09**-**MS09**	4.0	−4.4	−1.7	2.3	−0.6	−0.5

Overall the MP$-\alpha_i$,swe experiment performs better than the MP experiment. The experiment comes close to reproducing the area integrated ablation in three of the tests and close to reproducing mass balances in the 2009 tests, but fails to produce acceptable mass balances for the 2008 simulations. By examining Table 6.37 it appears as though the summer accumulation (C_s) is what is creating the large differences in mass balance. The summer accumulation is similar to the control values in the 2009 tests but far from the control in the 2008 tests, explaining the duality in model performance. The model performance where the summer accumulation is close to its control value justifies a further experiment wherein summer accumulation is retained along with ice albedo and initial snow-depth.

6.6.2 Assessing the role of Ice albedo, initial snow depth, and summer snowfall

In a final experiment all of the parameters and meteorological variables are transferred from one site to the other except ice albedo, initial snow-depth, and summer snowfall (MP$-\alpha_i$,swe,P_s). The comparison between MP$-\alpha_i$,swe,P_s experiment and the validation data is shown in Figures 6.23, 6.27 and Table 6.39. The comparison between the simulated and measured ablation at the stake locations (Figure 6.27) shows that in general the errors are larger than those in the control runs but smaller or the same as in the full MP and MP$-\alpha_i$,swe experiments. The relative (absolute) RMSE errors range from 0–6 % (0-0.08 m) greater than the control runs (Table 6.39). All of the test show the general trend of the 1 : 1 line. The comparison between this experiment and the USDG record (Figure 6.23) shows for the South Glacier 2008 MP$-\alpha_i$,swe,P_s test overestimates ablation compared to both the USDG record and the control run, but not as severely as the MP$-\alpha_i$,swe experiment. The South Glacier 2009 MP$-\alpha_i$,swe,P_s test closely tracks the full MP, MP$-\alpha_i$,swe experiments, and the USDG record. The North Glacier 2008 MP$-\alpha_i$,swe,P_s test closely follows the MP$-\alpha_i$,swe experiment and the North Glacier 2008 MP$-\alpha_i$,swe,P_s test underestimates ablation compared to the USDG record and control run, but not as badly as the full MP experiment.

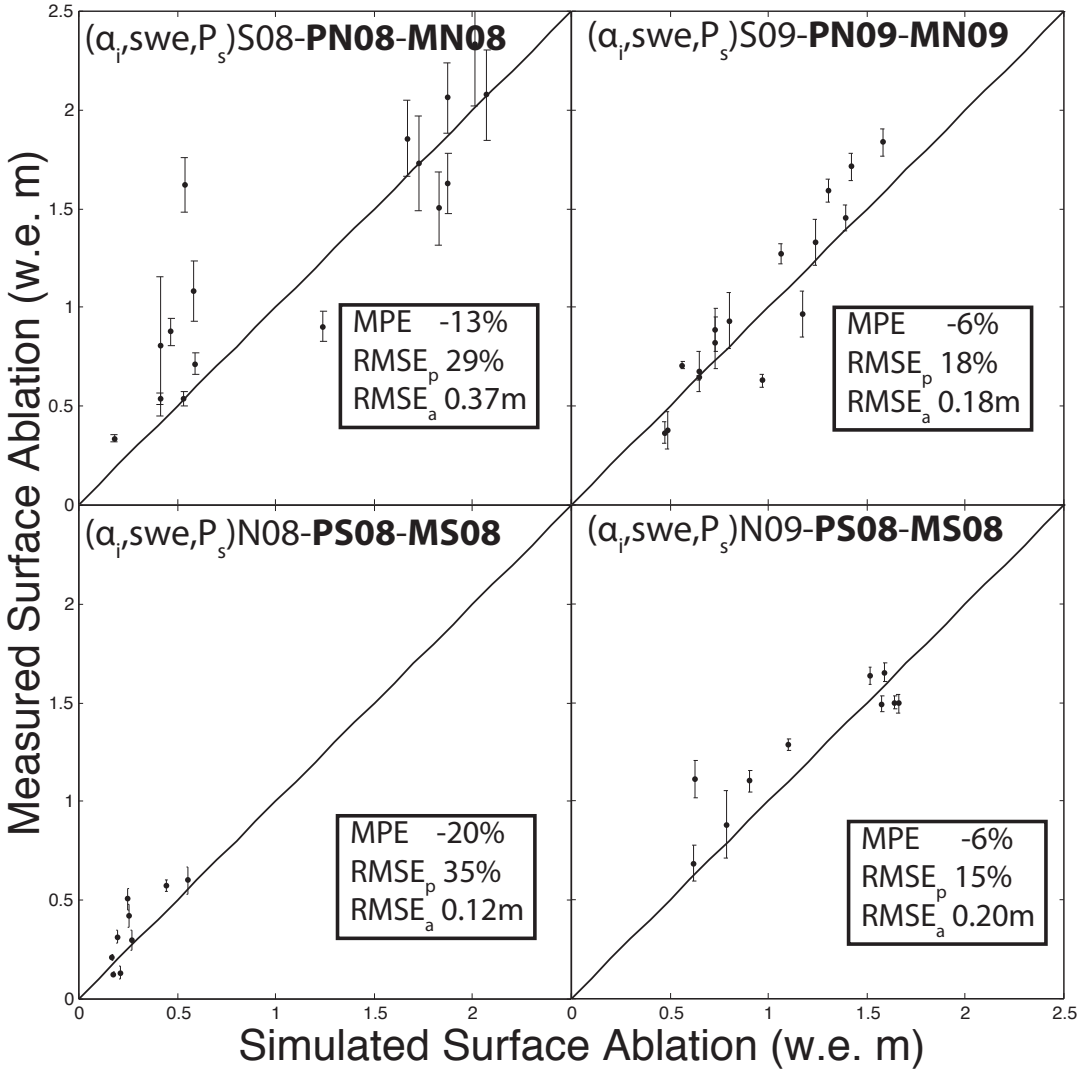

Figure 6.27: Comparison of results of the meteorological variable transfer experiment, but with locally-measured ice albedo and all snow variables, to ablation stake measurements.

Table 6.39: Difference between simulated and measured ablation at stake locations for the meteorological variable transfer experiment, but with locally-measured ice albedo and all snow variables.

Simulation	MPE (%)	$RMSE_p$ (%)	$RMSE_a$ (m)
(α_i,*swe*,P_s)S08-**PN08**-**MN08**	−13	29	0.37
(α_i,*swe*,P_s)S09-**PN08**-**MN09**	−6	18	0.18
(α_i,*swe*,P_s)N08-**PS08**-**MS08**	−20	35	0.12
(α_i,*swe*,P_s)N09-**PS09**-**MS09**	−6	15	0.20

The comparison between the MP$-\alpha_i$,swe,P_s experiment and the control runs are shown in Figures 6.23, 6.28 and Tables 6.40 – 6.42. The differences in spatially distributed ablation between this experiment and the control runs (Figure 6.28) show the same general patterns as seen in the MP$-\alpha_i$,swe experiment, except smaller in magnitude. The South Glacier 2008 MP$-\alpha_i$,swe,P_s test shows a band of overestimation of ablation and a band of underestimation with respect to the control run. The South Glacier 2009 MP$-\alpha_i$,swe,P_s test shows a band of overestimation near the ice–firn transition and week wavy pattern in the ablation zone, with respect to the control run. The North Glacier 2008 MP$-\alpha_i$,swe,P_s test has a patchy pattern over much of the glacier and the North Glacier 2009 MP$-\alpha_i$,swe,P_s test shows uniform small differences, with respect to the control run. The absolute differences in spatially integrated ablation between this experiment and the control runs (Table 6.41) ranges from 0–9 w.e. cm, with zero difference for the South Glacier 2009 test, 7 w.e. cm difference for the North Glacier 2008 test and the North Glacier 2009 test, and 9 w.e. cm difference for the South Glacier 2009 test. The differences in mass balance are identical. The difference in energy balance components show large deviations with respect to the control run in most of the components that largely cancel out (Table 6.42). From the mass balance components one can see that retaining local summer accumulation makes some of the simulations compare more poorly to the control runs, but on the whole makes the simulations of mass balance more consistent. It appears that high mass balance skill for the 2009 tests in the MP$-\alpha_i$,swe experiment was due to excess ablation being canceled by excess summer snowfall.

Overall the joint parameter and meteorological variable transferability experiments demonstrate that in this study region that it is possible to extend the DEBM across the range to within order 10 w.e. cm ablation accuracy if one can determine the local ice albedo and the local snowfall in each basin. Methods to estimate ice albedo for individual glaciers using remote sensing data are well established (Klok et al., 2003) and therefore this parameter can justifiably be derived locally for a regional DEBM without undo expense. Deriving local basin snowfall is a more challenging problem that is exploted in further discussion (see Chapter *Discussion*).

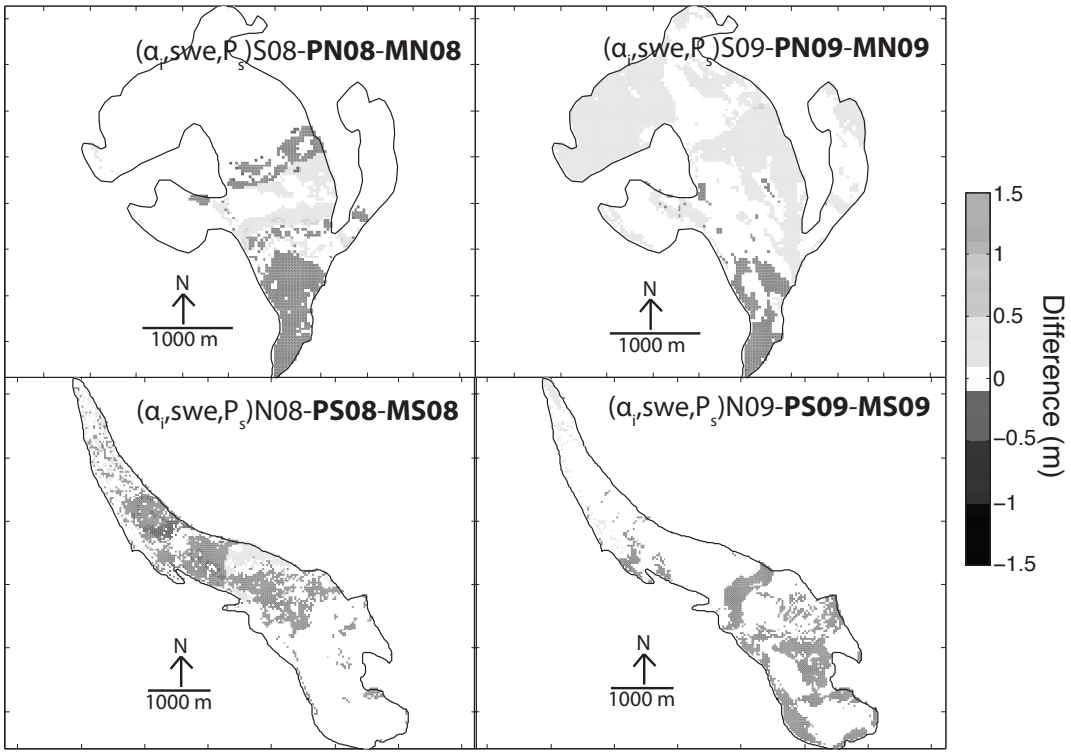

Figure 6.28: Difference in spatially distributed ablation as calculated by the parameter and meteorological variable transfer experiment, but with locally-measured ice albedo and all snow variables, and the spatially distributed ablation in the control runs. Note that white delineates near-zero difference.

Table 6.40: Difference between the spatially distributed ablation for the parameter and meteorological variable transfer experiment, but with locally-measured ice albedo and all snow variables, and the control runs expressed as MPE and RMSE.

Simulation	MPE (%)	$RMSE_p$ (%)	$RMSE_a$ (m)
(α_i,*swe*,P_s)S08-**PN08**-**MN08**	0	17	0.13
(α_i,*swe*,P_s)S09-**PN09**-**MN09**	11	20	0.16
(α_i,*swe*,P_s)N08-**PS08**-**MS08**	−16	36	0.17
(α_i,*swe*,P_s)N09-**PS09**-**MS09**	−8	11	0.09

Table 6.41: Spatially averaged mass balance components as estimated for the parameter and meteorological variable transfer experiment, but with locally-measured ice albedo and all snow variables, and the difference in summer ablation and mass balance with respect to the control runs. C_w is winter surface accumulation, C_s is summer surface accumulation, A_s is summer surface ablation, B_n is surface net balance, $\triangle A_s$ is the difference in summer ablation, and $\triangle B_n$ is the difference in net mass balance with respect to the control run. Units are in w.e. m.

Simulation	C_w	C_s	A_s	B_n	$\triangle A_s$	$\triangle B_n$
(α_i,*swe*,P_s)S08-**PN08**-**MN08**	0.33	0.28	−0.79	−0.18	0	0
(α_i,*swe*,P_s)S09-**PN09**-**MN09**	0.53	0.05	−0.90	−0.32	−0.09	−0.09
(α_i,*swe*,P_s)N08-**PS08**-**MS08**	0.23	0.17	−0.39	0	0.07	0.07
(α_i,*swe*,P_s)N09-**PS09**-**MS09**	0.38	0.07	−0.63	−0.18	0.07	0.07

Table 6.42: Difference in spatially averaged energy balance components between meteorological variable transfer experiment, but with locally-measured ice albedo and all snow variables, and control runs. $\triangle S_{\text{net}}$ is the difference in net shortwave radiation, $\triangle L_{\text{net}}$ is the difference in net longwave radiation, $\triangle Q_{\text{H}}$ is the difference in sensible heat flux, $\triangle Q_{\text{L}}$ is the difference in latent heat flux, $\triangle Q_{\text{g}}$ is the difference in subsurface heat flux, and $\triangle Q_{\text{M}}$ is the difference in the energy available for melt. Units are in W m^{-2}

Simulation	$\triangle S_{\text{net}}$	$\triangle L_{\text{net}}$	$\triangle Q_{\text{H}}$	$\triangle Q_{\text{L}}$	$\triangle Q_{\text{g}}$	$\triangle Q_{\text{M}}$
(α_{i},*swe*,P_{s})S08-**PN08**-**MN08**	−2.5	1.0	1.2	−0.4	0.7	0
(α_{i},*swe*,P_{s})S09-**PN09**-**MN09**	1.9	3.3	1.7	−2.4	0.6	5.1
(α_{i},*swe*,P_{s})N08-**PS08**-**MS08**	−1.7	0.5	−0.9	0.6	−0.7	−2.3
(α_{i},*swe*,P_{s})N09-**PS09**-**MS09**	−3.2	−0.9	−1.7	2.6	−0.6	−3.8

6.7 Discussion

6.7.1 Experiment inter-comparison

The mass balance components for each of the experiments and their constituent tests are shown in Figure 6.29. This figure visually demonstrates the primary results from this Chapter: that the TP experiment closely reproduces the control values; that the M experiment gives the opposite sign for the mass balance of North Glacier; and that retaining ice albedo, initial snow-depth and summer snowfall at locally measured values in the MP−α_{i},swe,P_{s} experiment can produce results close to the control run.

Tables 6.43 – 6.46 summarize the critical statistics for all of the simulations conducted for each glacier-year combination. The critical statistics are those that are to my understanding the most informative about the skill of the model with respect to the validation data (relative RMSE with respect to the ablation stake measurements), and each test's ability to reproduce the results of the control runs (the absolute value of the difference in summer ablation and mass balance).

The inter-comparisons show that in general the TP experiment can reproduce mass balance to within 4 w.e. cm of the control value. The SP and STP experiments can reproduce mass balance to within 10 w.e. cm. Retaining ice albedo in these experiments will in most,

but not all, cases improve model performance. The M experiment produces large errors in mass balance that can be partly compensated by retaining local initial snow-depth. The MP experiment also produce large errors, but these can be reduced by retaining ice albedo, initial snow-depth and summer snowfall. If these quantities are retained mass balance can be reproduced to within 9 w.e. cm relative to the control runs.

An interesting outcome of comparing these experiments is that when retaining key quantities transferring both the parameters and meteorological variables produces less error than transferring only the meteorological variables. This indicates that the parameter values are not independent of the meteorological variables but are in some way taking into account the local meteorological condition of the place and time from whence they are derived.

There are several test where the RMSE with respect to the ablation stake measurements is smaller for the test than in the control run. This is likely a result of both not tuning the model to mass balance data and the large uncertainties in the estimation of snow accumulation. By not tuning the model to the mass balance data the control runs do not represent the best fit between the data and all possible model outputs. That the control runs are not the best fit indicates that there is room for improvement in the sub-model components. Given the degree of bias in the control runs it is not surprising that using transferred initial snow-depth can in some cases improve model performance. For example, reducing the initial snow-depth produces earlier snow–ice transitions and therefore increases ablation, which can compensate for the underestimation of ablation inherent to three of the control runs.

6.7.2 Patterns in distributed surface ablation differences

There are noticeable and consistent patterns in the differences in distributed surface ablation between the control runs and the tests. The South Glacier 2008 and North Glacier 2009 tests produce relatively uniform or elevation-banded differences in the ablation zone. The South Glacier 2009 tests in many cases produce a wavy pattern, and the North Glacier 2008 tests produce a patchy pattern in the ablation zone. In addition, all of the simulations have a tendency to produce differences near the ice–firn transition. The patterns of difference in the ablation zones mirror the pattern of snow line retreat on each glacier. For example, the North Glacier 2008 simulations have a patchy pattern of snow-line retreat and the dif-

Table 6.43: Summary of critical statistics for tests simulating mass balance of South Glacier 2008. The statistics are: the relative RMSE of each test when comparing simulated and measured ablation at the stake locations; the absolute values of the difference in summer ablation between the simulation and the control run; and the absolute value of the difference in mass balance between the test and the control run.

Simulation	$RMSE_p$ (%)	$\lvert\triangle A_s\rvert$ (w.e. m)	$\lvert\triangle B_n\rvert$ (w.e. m)
S08 control	23	-	-
S08-**PS09**-MS08	23	0.02	0.01
S08-**PN08**-MS08	41	0.12	0.07
S08-**PN09**-MS08	36	0.05	0
(α_i)S08-**PN08**-MS08	31	0.02	0.03
(α_i)S08-**PN09**-MS08	26	0.05	0.10
S08-PS08-**MN08**	22	0.08	0.25
(*swe*)S08-PS08-**MN08**	28	0.01	0.09
S08-**PN08**-**MN08**	40	0.09	0.12
(α_i,*swe*)S08-**PN08**-**MN08**	32	0.01	0.13
(α_i,*swe*,P_s)S08-**PN08**-**MN08**	29	0	0

Table 6.44: Summary of critical statistics for tests simulating mass balance of South Glacier 2009.statistics are: the relative RMSE of each test when comparing simulated and measured ablation at the stake locations; the absolute values of the difference in summer ablation between the simulation and the control run; and the absolute value of the difference in mass balance between the test and the control run.

Simulation	$RMSE_p$ (%)	$\lvert\triangle A_s\rvert$ (w.e. m)	$\lvert\triangle B_n\rvert$ (w.e. m)
S09 control	14	-	-
S09-**PS08**-MS09	13	0.02	0.02
S09-**PN09**-MS09	22	0.01	0.02
S09-**PN08**-MS09	25	0.05	0.04
(α_i)S09-**PN09**-MS09	15	0.09	0.10
(α_i)S09-**PN08**-MS09	18	0.02	0.03
S09-PS09-**MN09**	16	0.11	0.22
(*swe*)S09-PS09-**MN09**	26	0.06	0.09
S09-**PN09**-**MN09**	17	0.08	0.21
(α_i,*swe*)S09-**PN09**-**MN09**	24	0	0.01
(α_i,*swe*,P_s)S09-**PN09**-**MN09**	18	0.09	0.09

Table 6.45: Summary of critical statistics for tests simulating mass balance of North Glacier 2008.statistics are: the relative RMSE of each test when comparing simulated and measured ablation at the stake locations; the absolute values of the difference in summer ablation between the simulation and the control run; and the absolute value of the difference in mass balance between the test and the control run.

Simulation	$RMSE_p$ (%)	$\lvert\triangle A_s\rvert$ (w.e. m)	$\lvert\triangle B_n\rvert$ (w.e. m)
N08 control	30	-	-
N08-**PN09**-MN08	40	0.04	0.04
N08-**PS08**-MN08	126	0.13	0.10
N08-**PS09**-MN08	39	0.16	0.13
(α_i)N08-**PS08**-MN08	35	0.02	0.01
(α_i)N08-**PS09**-MN08	33	0.05	0.02
N08-PN08-**MS08**	54	0.12	0.30
(*swe*)N08-PN08-**MS08**	38	0.07	0.14
N08-PS08-MS08	53	0.05	0.29
(α_i,*swe*)N08-**PS08**-**MS08**	43	0.07	0.20
(α_i,*swe*,P_s)N08-**PS08**-**MS08**	35	0.07	0.07

Table 6.46: Summary of critical statistics for tests simulating mass balance of North Glacier 2009. statistics are: the relative RMSE of each test when comparing simulated and measured ablation at the stake locations; the absolute values of the difference in summer ablation between the simulation and the control run; and the absolute value of the difference in mass balance between the test and the control run.

Simulation	$RMSE_p$ (%)	$\lvert\triangle A_s\rvert$ (w.e. m)	$\lvert\triangle B_n\rvert$ (w.e. m)
N09 control	15	-	-
N09-**PN08**-MN09	20	0.04	0.04
N09-**PS09**-MN09	29	0.09	0.08
N09-**PS08**-MN09	29	0.09	0.08
(α_i)N09-**PS09**-**MN09**	16	0.02	0.04
(α_i)N09-**PS08**-**MN09**	16	0.02	0.03
N09-PN09-**MS09**	35	0.14	0.50
(*swe*)N09-PN09-**MS09**	11	0.08	0.10
N09-**PS09**-**MS09**	32	0.18	0.55
(α_i,*swe*)N09-**PS09**-**MS09**	15	0.01	0
(α_i,*swe*,P_s)N09-**PS09**-**MS09**	15	0.07	0.07

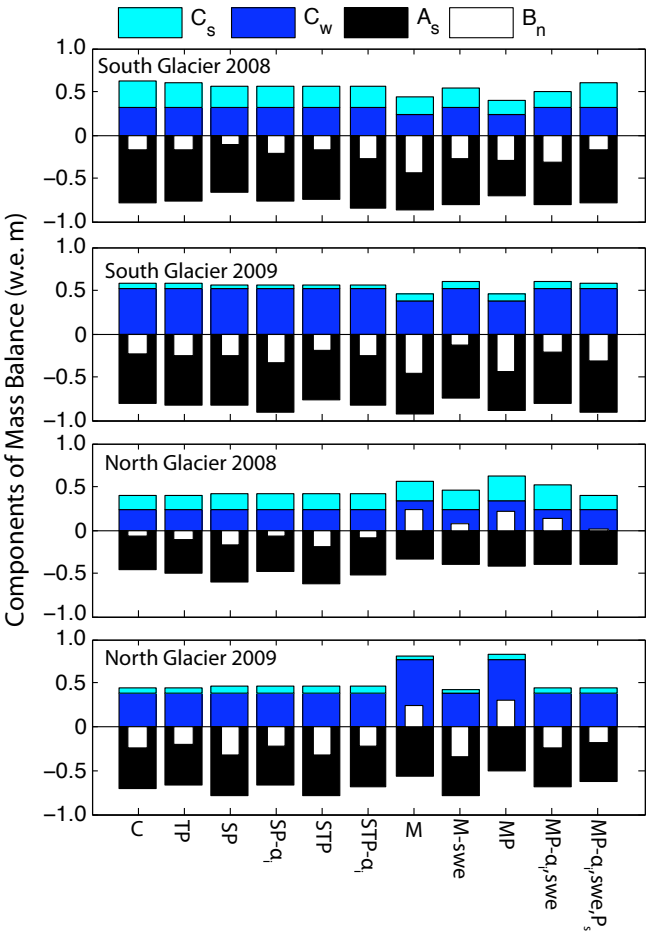

Figure 6.29: Estimated mass balance components for the control run and each of the transfer tests: C_w is winter surface accumulation, C_s is summer surface accumulation, A_s is summer surface ablation and B_n is surface net balance. Summer accumulation is stacked on winter accumulation while net mass balance is superimposed on other components. C is control, TP parameter transfer in time, SP parameter transfer in space, SP$-\alpha_i$ SP but with locally measured ice albedo retained, STP parameter transfer in space and time, STP$-\alpha_i$ SP but with locally measured ice albedo retained, M meteorological variable transfer, M$-$swe M but with locally measured initial snow-depth retained, MP meteorological variable and parameter transfer, MP$-\alpha_i$,swe MP with locally retaining local values of ice albedo and initial snow-depth, and MP$-\alpha_i$,swe,P_s MP retaining local values of ice albedo, initial snow-depth and summer snowfall.

ferences in ablation with respect to the control run appear to result from slightly altered rates of snow-line retreat in the transfer experiments. The rate of snow-line retreat controls the timing of the snow–ice transition, a major factor in total summer ablation due to the difference in albedo between the two surface types. The difference in ablation near the ice–firn transition has a simple explanation, the different data-sets have different firn-line elevations. Transferring the firn line in the parameter transfer experiments and joint transfer experiments creates a large firn/ice albedo dichotomy that creates large differences in ablation. For region scale simulations it is advisable to attempt to retrieve firn-lines from remote sensing data. For long-timescale modelling it may be more appropriate to use the multiyear averages of the equilibrium-line to infer the firn-line, instead of using a fixed elevation firn-line.

6.7.3 Implications for model transferability

From the standpoint of attempting to extend a DEBM in either space or time the two most important experiments are: the parameter transferability in time and the joint parameter and meteorological transferability in space. Parameter transferability in time is important if one desires to project glacier mass balance for a multiyear time period using either reanalysis data or general (regional) circulation model output. That the parameters in this experiment appear to be highly transferable in time, indicates that it may be possible to project mass balance many years into the future (assuming that changes in glacier shape and volume are properly taken into account). With only two glaciers and two years to test the transferability in time these conclusions must be taken with caution. The dichotomy between the cold snowy summer of 2008 and warm dry summer of 2009 indicates that implicit meteorological factors in the parameter values are relatively weak. That is, the parameters do largely reflect local perennial glaciological features.

The spatial parameter transfer and meteorological variable transfer experiments, although interesting for evaluating transferability, are of limited practical value for large scale model implementation. Simply put, if one goes through all of the trouble and expense to measure meteorological variables at a glacier site it is of almost trivial effort to also derive at least some of the needed parameter values. In the reverse it is impossible to derive many of the parameter values without meteorological data.

The joint transferability of parameters and meteorological variables is important if one were to treat an entire region as an extension of one well studied glacier. Given the results of these experiments one can see that taking such a approach will produce large errors in simulated ablation. The ice albedo, initial snow-depth and summer snowfall of each glacier must be known individually to achieve less than a ± 10 w.e. cm error in net mass balance. If these obstacles can be overcome DEBMs could more reliably be extended over large areas which could greatly improve projections of available water resources and sea level contribution from mountain glaciers and ice-caps.

6.8 Summary

A distributed energy balance melt model has been created for two mountain glaciers in the Donjek Range of the St. Elias Mountains, Yukon, Canada. The model was calibrated separately for the two glaciers for the summers of 2008 and 2009 using albedo and aerodynamic roughness length data sets, leaving ablation stake and ultra sonic depth gauge data as independent validation data. The four data sets were used for a series of transferability experiments wherein the spatial and temporal transferability of model parameters and meteorological driving variables was assessed. The results of these experiments demonstrate that model parameters are transferable in time to within 4 w.e. cm of ablation. Together the model parameter and meteorological variable forcings are transferable in space to within 9 w.e. cm of ablation, if local glacier ice albedo, initial snow-depth and summer snowfall are known for each glacier basin.

Two current weaknesses of distributed energy balance models are the use of empirical albedo evolution parameterizations and the lack of distributed wind fields. Both of these weaknesses have recently been overcome in local or offline studies (Dadić et al., 2010, Gardner and Sharp, 2010). The incorporation of these physical processes in distributed energy balance modeling should form the next major step in distributed model evolution. If these processes can be successfully incorporated into DEBMs without exceeding the limits of the available data sets, it would be important to reassess model transferability.

Chapter 7

Discussion

7.1 Energy balance inter-comparison

The areally averaged energy balance components calculated by the DEBM for the control runs can be compared between the two glacier sites (Table 7.1). South Glacier receives more net radiation than North Glacier and turbulent fluxes are larger on North Glacier than South Glacier. The difference in the mean value of net radiation between the two glaciers is a result of South Glacier receiving more shortwave radiation due to the glaciers' southerly aspect. The larger mean turbulent fluxes on North Glacier appear to be a result of that glacier reaching lower elevations than South Glacier. Turbulent fluxes are a function of temperature and air density, which increase at low elevations.

Compared to other glaciers where DEBMs have been implemented, the Donjek Range study glaciers derive a relatively high proportion of melt energy from net radiation (Table 7.1): net radiation comprises 83 % of the melt energy for South Glacier in 2008 and 81 % in 2009, 60 % of the melt energy for North Glacier in 2008 and 76 % in 2009. These values are comparable to Haut Glacier d'Arolla in summer 1990 (82 % net radiation) (Arnold et al., 1996), and South Cascade Glacier in summer 2004 (62 % net radiation) and summer 2005 (68 % net radiation). The relative contribution of net radiation to melt energy is higher for the Donjek Range study glaciers than that found for Storglaciären in the summers of 1993 (35 % net radiation) and 1994 (57 % net radiation) (Hock and Holmgren, 2005), and than that found for Brewster Glacier between 2004–2008 (45 % net radiation) (Anderson et al., 2010). I make these comparisons in areally averaged fluxes from different studies, bearing

in mind that each study covers a different length of time and employs a different model design. All else being equal glaciers in continental climates will tend to be dominated by net radiation, while glaciers in costal climates will have large contributions from turbulent heat fluxes (Hock, 2005). There are however many complicating factors that influence the proportion and magnitude of the energy balance components. The geometry of the glacierized valley controls the proportion of the glacier that is shaded, the fraction of the sky that is visible, and how the surrounding mountains act as longwave radiators. The slope and aspect of a glacier have a strong effect on the contribution from incoming shortwave radiation, especially at high latitudes where the sun is perpetually at low elevations angles. At low latitudes shading is reduced and incident solar radiation is larger. The turbulent fluxes are strongly affected by elevation of the glacier which determines the density of the air and the ability of the air to hold moisture. Glaciers at high elevations receive relative little of their melt energy from turbulent fluxes (Sicart et al., 2008, Wagnon et al., 2003). The magnitude of turbulent fluxes is directly proportional to wind speed, which is intern determined by many complicated atmospheric and topographical variables (e.g. Dadić et al., 2010). All of these factors must be taken into account when comparing the energy balance of glaciers from different locations. Given the small number of glaciers where DEBMs have been implemented and the large number of factors that must be considered in energy balance partitioning, it is best to view the above comparison as context for only one of many glacier characteristics to be taken into account when classifying glaciers in complex terrains.

7.2 The limits of model transferability

The high transferability of parameters in time suggests that the DEBM could be run for many years at North Glacier and South Glacier without re-calibration, opening the possibility of using regional climate model output to project future ablation. High transferability of both model parameters and meteorological variables in space is desirable for regional melt modeling, where it is convenient to treat all glaciers in a range as extensions of the study glacier. The transferability experiments have shown that extending the DEBM from one to many glaciers in the Donjek Range will probably lead to large errors in calculated ablation, unless ice albedo, initial snow-depth and summer snowfall can be better parameterized or further constrained. Ice albedo can be derived from satellite remote sensing

Table 7.1: Summary of energy balance partitioning between net radiation (Q_N) and turbulent heat fluxes (Q_T) for this study and for previous studies implementing DEBMs. Net radiation is the sum of net shortwave and net longwave radiation. The turbulent fluxes are the sum of the sensible and latent heat fluxes.

Study	Glacier	Period	Q_n (%)	Q_T (%)
MacDougall (2010)	South Glacier	2008	83	14
MacDougall (2010)	South Glacier	2009	81	19
MacDougall (2010)	North Glacier	2008	60	37
MacDougall (2010)	North Glacier	2009	76	24
Arnold et al. (1996)	Haut Glacier d'Arolla	1990	82	18
Hock and Holmgren (2005)	Storglaciären	1993	35	48
Hock and Holmgren (2005)	Storglaciären	1994	57	42
Anslow et al. (2008)	South Cascade Glacier	2004	62	38
Anslow et al. (2008)	South Cascade Glacier	2005	68	32
Anderson et al. (2010)	Brewster Glacier	2004–2008	45	52

(Klok et al., 2003), but remotely deriving initial snow-depth and summer snowfall presents a greater challenge. Snow depth can be derived from satellite remote sensing, even in complex terrain (Shi and Dozier, 2000). However spatial resolution, data availability at the right time of year and uncertainties in the derived snow depth itself remain challenges in implementing remotely sensed snow depth in high resolution models. Recent advances in orographic snow redistribution models (Dadić et al., 2010) suggest that it might be possible to use reanalysis precipitation data, coupled to a model of wind redistribution of snow, to produce realistic snow distributions for each basin of interest. The computational intensity of such calculations remains a significant obstacle. Existing physical and statistical orographic precipitation models have been developed and used in complex terrain (e.g. Kunz and Kottmeier, 2006, Schuler et al., 2008), however these models do not account for the transport of snow from valley walls to glaciers.

7.3 Differences between the study sites

One of the ultimate aims of the glaciological research program in the Donjek Range is to create reliable regional scale glacier melt-models. To better understand how to reliably extend the DEBM to the rest of the range I examine the differences between the two study sites. The primary differences between the glaciers are their locations on opposing sides of a topographic divide, and the dynamic regimes of the glaciers – South Glacier exhibits surge-type behavior and North Glacier does not. The glaciers have similar elevation-area distributions, with North Glacier having a somewhat larger proportion of its area at low elevation. Comparing the mean values of the measured meteorological variables shows that there is less difference between the sites in terms of barometric pressure, temperature, and incoming radiation than the measurement uncertainty for each of those quantities (Table 7.2). The only major meteorological differences between the sites is that North Glacier has a smaller initial snow-depth than South Glacier. Summer snowfall, wind speed and relative humidity were lower on North Glacier in 2008, but not in 2009 when snowfall totals were small (Table 7.2 and 7.3). Parameter values, particularly those related to albedo, vary much more substantially between the two sites than the meteorological variables do. The difference in ice albedo between the two sites is curious, as ice albedo is expected to be similar for glaciers with commensurate debris inputs and dust deposition. This difference in

ice albedo may be a product of South Glacier's surge-type dynamic nature; field personnel have occasionally witnessed debris rich water emerging at the surface from moulins and fractures on South Glacier. Much of this debris presumably remains on the ice, and lowers the albedo. The most important difference between the two sites appears to be related to precipitation and orography. I hypothesize that the study glaciers are typical of their respective sides of the range, except in ice albedo. This hypothesis could be explored by deploying additional AWSs on the respective sides of the range and by extracting ice albedo values from satellite data for the other glaciers in the range.

Table 7.2: Mean value of each meteorological variable measured by AWSs. Percent differences are relative to South Glacier values.

Variable	Mean Value S08	Mean Value N08	Difference (%)
p_c	776 mbar	764 mbar	±0.3 %
ϕ	75 %	71 %	±5.3 %
T_a	0.1 °C	0.4 °C	±0.1 %
u_z	2.0 ms^{-1}	1.5 ms^{-1}	±22 %
I	171 Wm^{-2}	169 Wm^{-2}	±1.2 %
D	91 Wm^{-2}	92 Wm^{-2}	±1.1 %
L_{in}	207 Wm^{-2}	208 Wm^{-2}	±0.5 %
Variable	Mean Value S09	Mean Value N09	Difference (%)
p_c	770 mbar	768 mbar	±0.3 %
ϕ	66 %	65 %	±1.5 %
T_a	2.1 °C	2.1 °C	0 %
u_z	2.4 ms^{-1}	2.5 ms^{-1}	±3.8 %
I	222 Wm^{-2}	226 Wm^{-2}	±1.8 %
D	91 Wm^{-2}	90 Wm^{-2}	±1.1 %
L_{in}	219 Wm^{-2}	225 Wm^{-2}	±2.8 %

Table 7.3: Cumulative summer accumulation P_s and winter balance C_w. Summer accumulation is measured by the USDGs. Winter balance is areally averaged initial snow-depth. Percent differences are relative to South Glacier values.

(a)Variable	S08 (m w.e.)	S09 (m w.e.)	Difference (%)
P_s	0.20	0.13	$\pm$35 %
C_w	0.33	0.23	$\pm$30 %
(b)Variable	S08 (m w.e.)	S09(m w.e.)	Difference (%)
P_s	0.03	0.05	$\pm$67 %
C_w	0.53	0.38	$\pm$28 %

7.4 The appropriateness of physical melt modelling

Temperature-index models and simplified energy-balance models implicitly take into account all of the components of the energy balance with a small number of parameters (Hock, 2005). Intuitively this implies that DEBMs, which explicitly describe the components of the energy balance, should exhibit higher transferability in space and time, and/or higher model skill. The two studies that have examined the transferability of enhanced temperature-index models (Wheler, 2009, Carenzo et al., 2009) have found the models to be highly transferable in space and time. On the surface the success of these simple models and the limitations on DEBM transferability found in this study appear to undermine the case for using physically based models for regional melt-modelling. It is important to recall, however, that neither Wheler (2009) nor Carenzo et al. (2009) attempted to transfer initial snow-depth, from one site to the another. This is a serious caveat, considering how important knowledge of this quantity appears to be for DEBM model transferability. Also important to recall is that the results of simplified melt-models have been shown to drift away from those of physically based models when ablation is projected decades into the future (Hock et al., 2007). Simplified models may therefore be a better approach to regional melt modelling over short periods of time or in locations where insufficient data exist to calibrate a DEBM.

7.5 DEBM conceits and future directions

DEBMs are not entirely physically based but depend on a number of parameterizations to simplify complex physical processes such as snow albedo evolution. Moreover these parameterizations tend to include positive temperatures as a driving variable: both the snow albedo evolution and roughness length evolution parameterizations from this DEBM use cumulative positive temperatures as a proxy for melt energy. It has been suggested in literature (e.g. Brock et al., 2006) that replacing these cumulative temperature components with cumulative melt energy would introduce positive feedbacks into the DEBM which would render the such a model unstable. Ignoring such (well founded) advice I carried out an experiment in which the temperature variable in the Hock and Holmgren (2005) albedo evolution parameterization was replaced with available melt energy. The DEBM was initialized using the original parameterization and an iterative loop applied until the model converged. The model does not converge until snow albedo rapidly reaches it's lower limit in all model grid cells, immensely overestimating ablation. This experiment supports the Brock et al. (2006) hypothesis that using available melt energy instead of positive temperatures in parameterizations leads to model instabilities and unreliable output.

Replacing the temperature based parameterizations in DEBMs with physically based sub-models should be a priority for future energy balance melt-modelling. Advances have recently been made in the physical modelling of snow albedo (Gardner and Sharp, 2010), efforts should be made to integrate physical albedo models into DEBMs.

DEBMs must frequently make oversimplified assumptions about meteorological quantities, in particular the assumption of uniform wind fields has been raised as a concern (Hock and Holmgren, 2005). Computing distributed wind fields in complex topography is physically intricate but possible (Dadić et al., 2010), however, the quantity of input data necessary for this process may exceed the limit of all but the most well studied glacier sites. If this process can be simplified or when required technology becomes inexpensive distributed wind fields should be added to DEBMs.

Chapter 8

Summary, Conclusions and Future Work

8.1 Summary

Modelling melt from glaciers and ice-caps is a critical step in assessing the impact of anthropogenic climate warming on eustatic sea level-rise and regional fresh water availability (Lemke et al., 2007). To model glacier melt at large spatial scales models are typically calibrated to well studied glaciers and applied unaltered to many other glaciers in the surrounding region. This method assumes that the melt models have high transferability in space and time despite evidence that such transferability is not universally possible (Hock, 2003, Hock et al., 2007). Empirical melt models in particular have been shown to drift away from physically based energy balance melt models when run many decades into the future (Hock et al., 2007). In this study the first steps were taken to applying physically based energy balance models regionally by exploring the transferability of such a model between two glacier in the Donjek Range of the St. Elias Mountains.

The two glaciers were studied in detail in the summers of 2008 and 2009. Mass balance was measured at an array of ablation stakes at least twice in each summer, and continuous meteorological measurements were made by Automatic Weather Stations (AWSs). These measurements included net all-wave radiation, and incoming and reflected shortwave radiation. The microtopographic technique was used to measure aerodynamic roughness length,

a parameter has often used to tune energy balance models.

Energy balance melt models parameterize or utilize measurements of all of the components of the surface energy balance of ice or snow to solve for the energy available to melt ice as a residual. Distributed energy balance melt models extrapolate the surface energy balance across a grid on the glacier surface such that melt can be resolved across the entire glacier. The energy balance is written as:

$$Q_M = (S_{\text{in}}(1-\alpha) + L_{\text{in}} - L_{\text{out}}) + Q_H + Q_L - Q_g + Q_R, \tag{8.1}$$

Incoming shortwave radiation (S_{in}) is measured at the AWS and extrapolated to the rest of the glacier by breaking the flux into its direct and diffuse components, applying the diffuse component to all grid points and the direct component to grid points not shaded by surrounding topography; albedo (α) is computed using the snow albedo evolution parameterization of Hock and Holmgren (2005) and by taking ice albedo as the mean measured value from the AWS location; the turbulent fluxes (Q_H and Q_L) are computed using the bulk aerodynamic approach; subsurface flux (Q_g) and outgoing longwave radiation (L_{out}) are computed using a simplified two layer subsurface model; incoming longwave radiation (L_{in}) is computed as the residual of measured net radiation and the other radiative components of the energy balance; the sensible heat flux from rain (Q_R) is disregarded. The DEBM is calibrated by: finding the best-fit parameters for the albedo parameterization with respect to the albedo record from the AWS for each glacier and each year; and using the aerodynamic roughness length data to find the best-fit snow roughness length evolution parameters. Mass balance data are not used to calibrate the model.

The model skill was examined by running the model with locally derived parameters and locally measured meteorological values. Modelled ablation from these control runs was compared to ablation at the stake locations and continuous ablation from an ultra sonic depth gauge record. In three of the four control runs ablation is underestimated by 10–11 %, and in the case of North Glacier 2008, overestimated by 18 %. Root mean square error ranges from 14–30 %, with the North Glacier 2008 simulation having the largest RMSE in a relative sense and the South Glacier 2008 simulation having the largest RMSE in an absolute sense. The simulated melt at the AWS location tracks the continuous USDG record of ablation to within 20 w.e cm. The model skill is similar to that achieved using empirical melt models in the same region (Wheler, 2009). The control runs were used

as references from which to gauge the results of the sensitivity tests and transferability experiments.

Sensitivity tests were conducted on the DEBM by perturbing each of the model parameters through a range of plausible values while holding all other parameters at their control values. These tests demonstrated that the model is most sensitive to perturbations in the albedo parameters and least sensitive to, lapse rates, and parameters describing the roughness length, the subsurface, and the albedo and emissivity of the terrain. Tests were also conducted to explore the sensitivity of the model to the uncertainty ranges of the meteorological variables. The model is most sensitive to uncertainties in wind speed, initial snow-depth and incoming longwave radiation. The sensitivities to wind speed and initial snow-depth are of the most concern as these quantities vary considerably in regions of complex topography, while estimated incoming longwave radiation is near identical at the two study sites.

Model transferability is the ability of a model calibrated for one time and location to produce realistic results at another time and/or location. Transferability was described here both in terms of model parameter values and meteorological driving variables. The former is the ability of parameters calibrated for one time or location to describe another, while the latter is the ability of meteorological variables measured at one site to drive a model at another site. Ideally, a model will have both high parameter transferability and high driving transferability, such that a model calibrated at one well-studied site can be used successfully at surrounding sites. The model parameters are transferable in time to within a bound of 4 cm w.e. (9 %) in the calculated ablation; model parameters are transferable in space to within a bound of 13 cm w.e. (28 %). Transferring meteorological variables, including accumulation, produces large differences in the calculated ablation, as does transferring model parameters and meteorological variables jointly. The joint parameter and meteorological variable transferability can be greatly improved (to within a bound of 9 cm w.e., 15 %) if locally measured ice albedo, initial snow-depth and summer snowfall are retained. Ice albedo can be derived for individual glacier basins from satellite remote sensing data (Klok et al., 2003), while initial snow-depth, and summer snowfall represent significantly more challenging quantities to obtain remotely.

8.2 Conclusions

From the experiments described in this thesis I concluded that:

1. A distributed energy balance melt model applied to the Donjek Range study glaciers, calibrated without using mass balance data, has a similar model skill as empirical melt models of the same glaciers.

2. The model is most sensitive to: the parameters that control albedo, wind speed, and initial snow-depth.

3. The model parameters are highly transferable in time.

4. The model has low parameter transferability in space, and in space and time. Spatial transferability can be improved if ice albedo is retained at its locally derived value.

5. The meteorological variables used to drive the model are poorly transferable in space.

6. The model has poor joint parameter and meteorological variable transferability. Joint transferability can be greatly improved if ice albedo, initial snow-depth and summer snowfall are retained at locally measured values.

7. If the model was imposed unaltered on the remaining glaciers of the Donjek Range $\sim$30 % errors in calculated ablation should be expected.

8. Techniques must be developed to remotely obtain ice albedo and snow depth before regional glacier melt models can achieve high reliability in complex topography.

8.3 Future Work

The Earth's glaciers and ice-caps comprise only a tiny faction of the cryosphere (Lemke et al., 2007), but are disproportionately important to human societies due to their rapid response to a change in climate (Oerlemans and Knap, 1998), their ability to act as natural water reservoirs (e.g. Huss et al., 2008), and their potential to create flash flooding hazards as they degrade. Accurate high temporal and spatial resolution modelling is crucial if realistic assessments are to be made of the effect of glacier degradation on fresh water supplies

and the agricultural production that depends on these glacier water sources. Monitoring all major glaciers with ground based field programs is unrealistic. Therefore efforts must be made to create glacier melt models that can be initialized entirely with remotely sensed data and integrated into coupled General Circulation Models (GCMs), as such models evolve into full Earth System Models (ESMs).

Given the current state of the science of glacier melt modelling several advance are necessary before integration into ESMs. One necessary advance is to overcome the limits of DEBM transferability in space as outlined in this study. One avenue to pursue this goal is to attempt to use remotely sensed data to acquire parameter values, initialization data, and validation data. If model transferability can be sufficiently improved using such data the next step it to replace ground based meteorological data with reanalysis data. Such a model would be entirely independent of ground based observations and could be extended to model melt in isolated glacierized regions.

Another parallel avenue to pursue is to create an entirely synthetic melt model which can be run offline utilizing GCM output. Such a model would downscale precipitation and calculate local wind speeds using an orographic sub-model and drive glacier melt using GCM calculated incoming radiative energy components. General circulation models and their descendants are the most sophisticated energy balance models ever created (Randall et al., 2007). They have advanced schemes for calculating incoming radiation which take cloud physics into account in a vastly superior fashion than the simple parameterization used in the current generation of DEBMs (Randall et al., 2007). Once such a model is created they could either be integrated into ESMs, if GCM grid cells have been reduced to sub-kilometric scales, or used as references to develop accurate stochastic sub grid-scale parameterizations of glacier melt.

Bibliography

Anderson, B., A. MacKintosh, D. Stumm, L. George, T. Kerr, A. Winter-Billington, and S. Fitzsimons, 2010: Climate sensitivity of a high-precipitation glacier in New Zealand. *J. Glaciol.*, **56**, 114–128.

Anslow, F. S., S. Hostetler, W. R. Bidlake, and P. U. Clark, 2008: Distributed energy balance modelling of South Cascade Glacier, Washington and assessment of model uncertainty. *J. Geophys. Res.*, **113**, doi:10.1029/2007JF000850.

Arendt, A. A., S. B. Luthcke, C. F. Larsen, W. Abdalati, W. B. Krabill, and M. J. Beedle, 2008: Validation of high-resolution GRACE mascon estimates of glacier mass changes in the St. Elias Mountains, Alaska, USA, using aircraft laser altimetry. *J. Glaciol.*, **256**, 165–172.

Arnold, N. S., I. C. Willis, M. J. Sharp, K. S. Richards, and W. J. Lawson, 1996: A distributed surface energy-balance model for a small valley glacier. 1. Development and testing for Haut Glacier d'Arolla, Valais, Switzerland. *J. Glaciol.*, **42**, 77–89.

Bahr, D., M. Dyurgerov, and M. F. Meier, 2009: Sea-level rise from glaciers and ice caps: a lower bound. *Geophys. Res. Lett.*, **36**, doi:10.1029/2008GL036309.

Barrand, N. E. and M. J. Sharp, 2010: Sustained rapid shrinkage of Yukon glaciers since the 1957–1958 Ineternational Geophysical Year. *Geophys. Res. Lett.*, **37**, doi: 10.1029/2009GL042030.

Beljaars, A. C. M. and A. A. M. Holtslag, 1991: Flux parameterization over land surfaces for atmospheric models. *J. Appl. Meteor.*, **30**, 317–359.

Berthier, E., E. Schiefer, G. K. C. Clarke, B. Menounos, and F. Rémy, 2010: Contribution of alaskan glaciers to sea-level rise derived from satellite imagery. *Nature Geoscience*, doi:DOI: 10.1038/NGEO737.

Brock, B. W., I. C. Willis, and M. J. Sharp, 2000a: Measurement and parameterization of albedo variations at Haut Glacier d'Arolla, Switzerland. *J. Glaciol.*, **46**, 657–688, doi:10.3189/172756500781832675.

Brock, B. W., I. C. Willis, and M. J. Sharp, 2006: Measurement and parameterization of aerodynamic roughness length at Haut Glacier d'Arolla, Switzerland. *J. Glaciol.*, **52**, 281–297.

Brock, B. W., I. C. Willis, M. J. Sharp, and N. Arnold, 2000b: Modelling seasonal and spatial variations in the surface energy balance of Haut Glacier d'Arolla, Switzerland. *Annals of Glaciology*, **31**, 53–62.

Carenzo, M., F. Pellicciotti, S. Rimkus, and P. Burlando, 2009: Assessing the transferability and robustness of an enhanced temperature-index glacier-melt model. *J. Glaciol.*, **55**, 258–274.

Clarke, G. K. C. and G. Holdsworth, 2002: Glaciers of the St. Elias Mountains. US Geological Survey professional paper ISSN 1044-9612.

Collares-Pereira, M. and A. Rabl, 1979: The average distribution of solar radiation: correlations between daily and hourly insolation values. *Solar Energy*, **22**, 155–164.

Corripio, J. G., 2004: Snow surface albedo estimated using terrestrial photography. *Int. J. Remote Sensing*, **25**, 5705–5729.

Dadić, R., R. Mott, M. Lehning, and P. Burlando, 2010: Wind influence on snow depth distribution and accumulation over glaciers. *J. Geophys. Res.*, **115**, doi: 1029/2009JF001261.

De Paoli, L. and G. E. Flowers, 2009: Dynamics of a small surge-type glacier using one-dimensional geophysical inversion. *J. Glaciol.*, **55**, 1101–1112.

de Woul, M. and R. Hock, 2005: Static mass-balance sensitivity of Arctic glaciers and ice caps using a degree day approach. *Ann. Glaciol.*, **42**, 217–224.

Denby, B. and W. Greuell, 2000: The use of bulk and profile methods for determining surface heat fluxes in the presence of glacier winds. *J. Glaciol.*, **46**, 445–452.

Forrer, J. and M. Rotach, 1997: On turbulence structure in the stable boundary layer over the Greenland ice sheet. *Boundary-Layer Meteorol.*, **85**, 111–136.

Gardner, A. S. and M. J. Sharp, 2010: A review of snow and ice albedo and the development of a new physically based broadband albedo parameterization. *J. Geophys. Res.*, **115**, doi:doi:10.1029/2009JF001444.

Greuell, W. and W. H. Knap, 1997: Elevation changes in meteorological variables along a mid–latitude glacier during summer. *J. Geophys. Res.*, **102**, 941–954.

Hock, R., 1999: A distributed temperature-index ice- and snowmelt model including potential direct solar radiation. *J. Glaciol.*, **45(149)**, 101–111.

Hock, R., 2003: Temperature index melt modelling in mountain areas. *J. Hydrology*, **282**, 104–115.

Hock, R., 2005: Glacier melt: a review of processes and their modelling. *Prog. Phys. Geog.*, **29(3)**, 362–391.

Hock, R. and B. Holmgren, 2005: A distributed energy-balance model for complex topography and its application to Storglaciären, Sweden. *J. Glaciol.*, **51**, 25–36, doi: 10.3189/172756505781829566.

Hock, R., V. Radić, and M. de Woul, 2007: Climate sensitivity of Storglaciären, Sweden: an intercomparison of mass-balance models using ERA-40 re-analysis and regional climate model data. *Ann. Glaciol.*, **46**, 342–348.

Huss, M., D. Farinotti, A. Bauder, and M. Funk, 2008: Modelling runoff from highly glacierized alpine drainage basins in a changing climate. *Hydrol. Process.*, **22**, 3888–3902.

Jonsell, U., R. Hock, and B. Holmgren, 2003: Spatial and temporal variations in albedo on Storglaciären, Sweden. *J. Glaciol.*, **49**, 59–68.

Kaser, G., J. G. Cogley, M. B. Dyurgerov, M. F. Meier, and A. Ohmura, 2006: Mass balance of glaciers and ice caps: Consensus estimates for 1961–2004. *Geophys. Res. Lett.*, **33**, doi:10.1029/2006GL027511.

Klok, E. J., W. Greuell, and J. Oerlemans, 2003: Temporal and spatial variation of the surface albedo of Morteratschgletscher, Switzerland, as derived from 12 Landsat images. *J. Glaciol.*, **49(167)**.

Klok, E. J. and J. Oerlemans, 2002: Model study of the spatial distribution of the energy balance of Morteratschgletscher, Switzerland. *J. Glaciol.*, **48**, 505–518, doi: 10.3189/172756502781831133.

Kunz, M. and C. Kottmeier, 2006: Orographic enhancement of precipitation over low mountain ranges. part I: Model formulation and idealized simulations. *J. Appl. Meteor. Climatol.*, **45**, 1025–1040.

Lemke, P., et al., 2007: Observations: Changes in snow, ice and frozen ground. *Climate Change 2007: The Physical Science Basis. Contribution of Working Group I to the Fourth Assessment Report of the Intergovernmental Panel on Climate Change*, S. Solomon, D. Qin, M. Manning, Z. Chen, M. Marquis, K. Averyt, M. Tignor, and H. Miller, Eds., Cambridge University Press.

Lettau, H., 1969: Note on aerodynamic roughness-parameter estimation on the basis of roughness-element description. *J. Appl. Meteor.*, **8**.

L'Heureux, M. L., M. E. Mann, B. I. Cook, B. E. Gleason, and R. S. Voss, 2004: Atmospheric circulation influences on seasonal precipitation patterns in Alaska during the latter 20th century. *J. Geophys. Res.*, **109**, doi:10.1029/2003JD003845.

MacDougall, A. H., 2010: Distributed energy-balance glacier melt-modelling in the Donjek Range of the St. Elias Mountains, Yukon Territory, Canada: model transferability in space and time. M.S. thesis, Dept. of Earth Sciences, Simon Fraser University, [Manuscript in preparation.].

Munro, D. S., 1989: Comparison of melt energy computations and albatometer measurements on melting ice and snow. *Arctic and Alpine Research*, **22**, 153–162.

Oerlemans, J. and B. Grisogono, 2002: Glacier winds and parameterization of the related surface heat fluxes. *Tellus*, **54A**, 440–452.

Oerlemans, J. and W. H. Knap, 1998: A one year record of global radiation and albedo in the ablation zone of Morteratschgletscher, Switzerland,. *J. Glaciol.*, **44**, 231–238.

Oerlemans, J., et al., 1998: Modelling the response of glaciers to climate warming. *Climate Dyn.*, **14**, 267–274.

Oerlemans, J., et al., 2005: Estimating the contribution of Arctic glaciers to sea-level change in the next 100 years. *Ann. Glaciol.*, **42**, 230–236.

Oke, T., 1987: *Boundary layer climates*. 2d ed., London, Methuen; New York, Routledge Press.

Paterson, W. S. B., 1994: *The Physics of Glaciers*. 3d ed., Reed Educational and Professional Publishing Ltd.

Paulson, C. A., 1970: The mathematical representation of wind speed and temperature profiles in the unstable atmospheric surface layer. *J. Meteorol.*, **9**, 857–861.

Pellicciotti, F., B. Brock, U. Strasser, P. Burlando, M. Funk, and J. Corripio, 2005: An enhanced temperature-index glacier melt model including the shortwave radiation balance: development and testing for Haut Glacier d'Arolla, Switzerland. *J. Glaciol.*, **51**, 573–587.

Pettersson, R., P. Jansson, and H. Blatter, 2004: Spatial variability in water content at the cold–temperate transition surface of the polythermal Storglaciären, Sweden. *J. Geophys. Res.*, **109**, doi:10.1029/2003JF000110.

Randall, D. A., et al., 2007: Climate models and their evaluation. *Climate Change 2007: The Physical Science Basis. Contribution of Working Group I to the Fourth Assessment Report of the Intergovernmental Panel on Climate Change*, S. Solomon, D. Qin,

M. Manning, Z. Chen, M. Marquis, K. Averyt, M. Tignor, and H. Miller, Eds., Cambridge University Press.

Raper, S. C. B. and R. J. Braithwaite, 2006: Low sea level rise projections from mountain glaciers and icecaps under global warming. *Nature*, **439**, 311–313.

Rasband, W. S., 1997–2009: Imagej, u. s. national institutes of health. [Available online at http://rsb.info.nih.gov/ij/, [Available online at http://rsb.info.nih.gov/ij/.

Rees, W. G., 1998: Correspondence: A rapid method for measuring snow surface profiles. *J. Glaciol.*, **44**, 674–675.

Rees, W. G. and N. S. Arnold, 2006: Scale-dependent roughness of a glacier surface: implications for radar backscatter and aerodynamic roughness modeling. *J. Glaciol.*, **52**, 214–222.

Reijmer, C. H. and R. Hock, 2008: Internal accumulation on Storglaciären, Sweden, in a multi-year snow model coupled to a distributed energy- and mass-balance model. *J. Glaciol.*, **54**.

Schneeberger, C., H. Blatter, A. Abe-Ouchi, and M. Wild, 2003: Modelling changes in the mass balance of glaciers of the northern hemisphere for a transient 2 $\times CO_2$ scenario. *J. Hydrology*, **282**, 145–263.

Schuler, T. V., P. Crochet, R. Hock, M. Jackson, I. Barstad, and T. Jóhannesson, 2008: Distribution of snow accumulation on the Svartisen ice cap, Norway, assessed by a model of orographic precipitation. *Hydrol. Proc.*, **22**, 3998–4008, doi:10.1002/hyp.7073.

Shi, J. and J. Dozier, 2000: Estimation of snow water equivalence using SIR-C/X-SAR, part II: inferring snow depth and particle size. *IEEE Trans. Geosci. Remote Sensing*, **38**, 2475–2488.

Sicart, J. E., R. Hock, and D. six, 2008: Glacier melt, air temperature, and energy balance in different climates: the Bolivian Tropics, the Frensh Alps, and northern Sweden. *J. Geophys. Res.*, **113**, doi:10.1029/2008JD010406.

Wagnon, P., J. E. Sicart, E. Berthier, and J. P. Chazarin, 2003: Wintertime high-altitude surface energy balance of a Bolivian glacier, Illimani, 6340 m above sea level. *J. Geophys. Res.*, **108**, doi:10.1029/2002JD002088.

Wheler, B. A., 2009: Glacier melt modelling in the Donjek Range, St. Elias Mountains, Yukon Territory. M.S. thesis, Dept. of Earth Sciences, Simon Fraser University.